Design, Synthesis, and Characterization of New Generation Lithium Batteries

Nuria Vicente Agut

March 2019

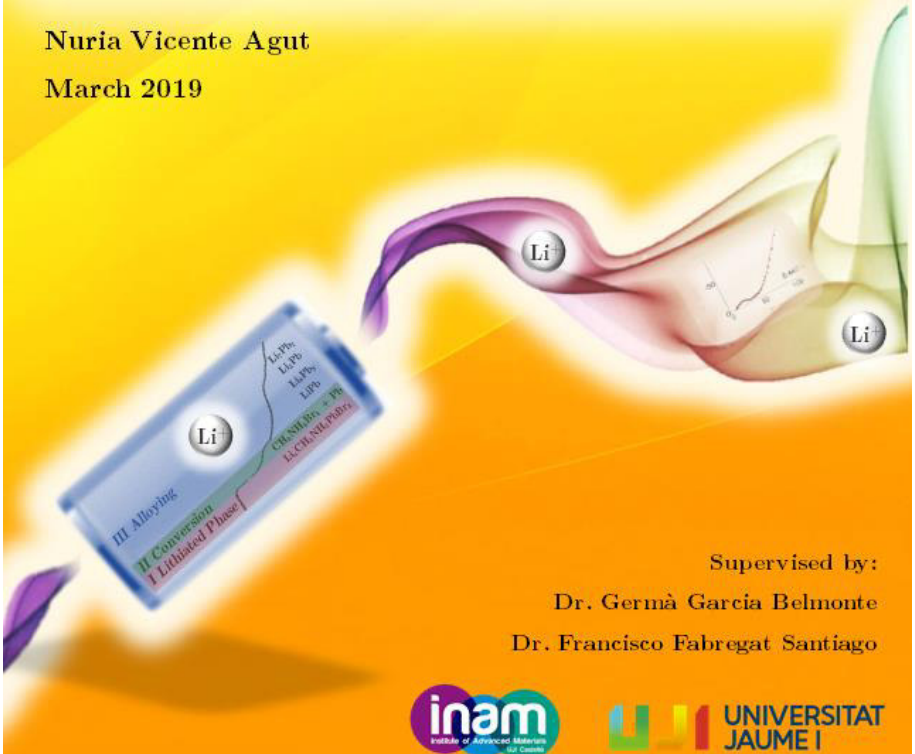

Supervised by:
Dr. Germà Garcia Belmonte
Dr. Francisco Fabregat Santiago

inam Institute of Advanced Materials

UNIVERSITAT JAUME I

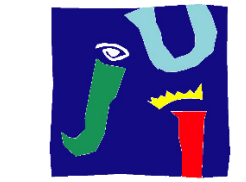

Programa de Doctorat en Ciències

Escola de Doctorat de la Universitat Jaume I

Design, Synthesis, and Characterization of New Generation Lithium Batteries

Memòria presentada per Nuria Vicente i Agut **per a optar al grau de doctora per la Universitat Jaume I**

Doctoranda:

Nuria Vicente Agut

Directors:

Dr. G. Garcia-Belmonte

Dr. F. Fabregat-Santiago

Castelló de la Plana, Juny de 2019

Fons de finançament

Aquesta tesi doctoral ha segut realitzada gràcies al finançament rebut per:

- Ajuda predoctoral per a la formació de personal investigador (PREDOC/2015/54), en el Pla de promoció de la investigació 2015 de la Universitat Jaume I.
- Beca per a realitzar una estada de tres mesos en el Helmholtz Institute Ulm (HIU) en Alemanya, en el Pla de promoció de la investigació 2017 de la Universitat Jaume I.
- Ajuda per a realitzar una estada de tres mesos en la Universitat Nacional de Seul en Corea del Sud, emmarcada en el projecte europeu, IRSES Internew.

El conjunt de projectes en els quals ha estat inclosa l'activitat investigadora durant la present tesi són els següents:

- UJI-B2016-35, del Pla d'investigació de la Universitat Jaume I de 2016.
- Projecte de la Generalitat Valencia: Prometeo, PROMETEO/2014/020) i de l'Institut de Nanotecnologies per a les Energies Netes (ISIC/2012/008).
- Els projectes MAT2016-76892-C3-1-R i MAT2011-22753, del Ministeri d'Economia i Competitivitat.
- Projectes Col · laboratius Europeus: ***Bioelectrochemical Systems for Metal Recovery,*** *BioelectroMET* (2012) i ***Novel Composite***

Oxides by Combinatorial Material Synthesis for Next Generation All-Oxide-Photovoltaics, $ALLOXIDEPV$ (2012).

"First principle: never to let one's self be beaten down by persons or by events."

Marie Skłodowska Curie

Agraïments. Acknowledgements.

No puc acabar aquesta etapa sense recordar tots aquells que ho han fet possible.

En primer lloc, m'agradaria agrair al meu director de tesis el Prof. Dr. Germà Garcia-Belmonte per la confiança depositada en mi per desenvolupar aquest projecte i el seu suport al llarg d'aquests anys. Al Dr. Francisco Fabregat-Santiago, codirector, per les llargues discussions de l'electroquímica i les seues idees. A la Dra. Marta Haro, junt a ella vaig posar els ciments d'aquesta investigació. Així com, a tots, i cadascun, dels membres dels grups d'investigació, GAME i GAS, amb qui he tingut el plaer de compartir el dia a dia.

In furtherance of obtaining my Ph. D, I have had the opportunity of being hosted in two international research centers. My first research stage was in Seoul National University, I had the opportunity of joining Prof. Yung-Eun Sung in School of Chemical and Biological Engineering. After that I could join to Prof. Passerini's group in Helmolth Institute Ulm in Germany, where I was allowed to carry out my experiments there under Dr. Bresser supervision. Both stays were wonderful and I want to extend my gratitude to all the people I had the chance to work with.

I de vosaltres, els *compis de centralita&CIA*, no me puc oblidar: Marta, Drialys, Roser, Ramón i Bruno, tampoc dels que vam passar per ahí: Isaac, Luca i Lucia. Gràcies per compartir molt més que hores de laboratori o discussions científiques, amb vosaltres mai han faltat rialles, xafarderies, cafès, el *Rossegó* i pizzes! Gràcies, a les nostres

mamis, que m'han cuidat i aconsellat sempre i per a tot, Eva i Loles. Tots vosaltres us heu convertit en família durant aquests anys.

También gracias a Pilar y Sandra, lejos o cerca, pero siempre a una llamada de teléfono para escucharme y aconsejarme en esta locura de la investigación que decidí emprender. Y por recordarme, muchas veces, lo verdaderamente importante. Viele danke, Amélie, denn während meines Aufenthaltes in Ulm hast du dein Zuhause eröffnet und du wurdest ein Freund. Gràcies als de casa: als amics de sempre (PX) i als que us heu sumat en els últims mesos, que sense saber massa bé el què faig sempre esteu ahí per a recolzar-me!

I, si miro enrere, aquest camí va començar amb llargues tardes d'estiu fent sumes i restes, inculcant-me la fascinació per les "cuentes" i refusant sempre les calculadores, per allò de si s'equivocaven... Gràcies iaios.

Per últim, i els més importants, els que han sigut, són i seran un pilar fonamental, els meus pares. Sense ells, ni el seu esforç, mai haguera sigut possible fer realitat aquest repte. Per inculcar-me des de ben menuda valors com el sentit de la responsabilitat, de l'esforç, de la perseverança i de la lluita per allò que vull i crec, GRÀCIES.

Scientific contribution

Publications included in this Thesis

1. Nuria Vicente, Marta Haro, Daniel Cíntora-Juárez, Carlos Pérez-Vicente, José Luis Tirado, Shahzada Ahmad, Germà Garcia-Belmonte. $LiFePO_4$ particle conductive composite strategies for improving cathode rate capability, *Electrochimica Acta*, **2015**, 163, 323-329. (DOI: 10.1016/j.electacta.2015.02.148)

   Impact factor 2015: 4.803 (Q1).

2. Marta Haro, Nuria Vicente, Germà Garcia-Belmonte. Oxygen Reduction Reaction Promotes Li^+ Desorption from Cathode Surface in Li-O_2 Batteries, *Advanced Materials Interfaces*, **2015**, 2 (16), 1500369. (DOI: 10.1002/admi.201500369)

   Impact factor 2015: 3.365 (Q1)

3. Nuria Vicente, Germà Garcia-Belmonte. Methylammonium lead bromide perovskite battery anodes reversibly host high Li-ion concentration, *The Journal of Physical Chemistry Letters*, **2017**, 8 (7), 1371-1374. (DOI: 10.1021/acs.jpclett.7b00189)

   Impact factor 2017: 8.480 (Q1)

4. Nuria Vicente, Germà Garcia-Belmonte. Organohalide Perovskites are Fast Ionic Conductors, *Advanced Energy Materials*, **2017**, 7 (19), 1700710. (DOI: 10.1002/aenm.201700710)

   Impact factor: 19.687 (Q1)

5. Nuria Vicente, Dominic Bresser, Stefano Passerini, Germà Garcia-Belmonte. Probing the 4-step Lithium storage Mechanism in CH3NH3PbBr3 Perovskite Electrode by Operando-XRD Analysis, *ChemElectroChem*, **2019**, 6, 456 – 460. (DOI: 10.1002/celc.201801291)
   Impact factor 2017: 4.312 (Q1).

This thesis has been accepted by the co-authors of the publications listed above that have waved the right to present them as a part of another PhD thesis.

Publications not included in this Thesis

1. Kang-Joon Park, Byung-Beom Lim, Moon-Ho Choi, Hun-Gi Jung, Yang-Kook Sun, Marta Haro, Nuria Vicente, Juan Bisquert, Germà Garcia-Belmonte. A high-capacity $Li[Ni_{0.8}Co_{0.06}Mn_{0.14}]O_2$ positive electrode with a dual concentration gradient for next-generation lithium-ion batteries, *Journal of Materials Chemistry A*, **2015**, 3 (44), 22183-22190.
2. Nuria Vicente, Marta Haro, Germà Garcia-Belmonte. New approaches to the lithiation kinetics in reaction-limited battery electrodes through electrochemical impedance spectroscopy, *Chemical Communications*, **2018**, 54 (9), 1025-1040.

Participation in conferences

1. *Probing lithiation kinetics of conversion-reaction battery materials*, Nuria Vicente, Gonzalo Molina, Marta Haro, Antonio Guerrero, 65th Annual meeting of the International Society of Electrochemistry, August 2014, Lausanne, Switzerland. (Poster).
2. *Mechanism scan in Li-O_2 batteries by impedance spectroscopy*, Marta Haro, Nuria Vicente, Germà Garcia-Belmonte, ECS

Conference on Electrochemical Energy conversion & Storage with SOFC-XIV, July 2015, Glasgow, United Kingdom. (Poster).

3. *Mechanism Identification in Lithium-Oxygen Batteries by Impedance Spectroscopy*, Nuria Vicente, Marta Haro, Germà Garcia-Belmonte. IBA2016-International Battery Association, March 2016, Nantes, France. (Poster).

4. *Next-Generation Li[Ni0.8Co0.06Mn0.14]O2 Positive Electrode Material with a Dual Concentration Gradient for High-Energy Li-Ion Batteries*, A.J. Park, H. G. Jung, Y. K. Sun, Marta Haro, Nuria Vicente, Juan Bisquert, Germà Garcia-Belmonte. ECS - 18th International Meeting on Lithium Batteries, June 2016, Chicago, EEUU. (Poster).

5. *Recent Advances in Photoelectrochemical Response of Perovskite/liquid Junction*, Nuria Vicente, Eva Maria Barea Berzosa, Germà Garcia-Belmonte, Research Workshop for Young Researchers Thin Film Emerging Photovoltaic and Optoelectronic Technologies, November 2016, Valencia, Spain. (Poster).

6. *Lead Bromide Perovskite Fast Ionic Conductor for High-Power Charge Storage Battery Anodes*, Nuria Vicente, Germà Garcia-Belmonte, The International Conference on Perovskite Thin Film Photovoltaics (ABXPV17), March 2017, Valencia, Spain. (Poster).

7. *High Li-Ion concentration and diffusion in methylammonium lead bromide perovskite battery anodes*, Nuria Vicente, Germà Garcia-Belmonte, MRS Fall Meeting, September 2017, Warsaw, Poland. (Poster).

Abstract

In the last years, Li-ion batteries received great attention because of the increasing energetics requirements of modern society across a broad range of applications. We need to switch to renewable source energy and be able to storage it. Hence, modern electrochemistry faces a great challenge in developing rechargeable batteries whose materials meet the requirement for excellent features, as very prolonged stability and cycle life, safe, low cost, abundant as possible and ecofriendly.

Herein, different materials are characterized electrochemically: $LiFePO_4$ anode, Li-O_2 batteries and the innovative $CH_3NH_3PbBr_3$ anode. Impedance spectroscopy allows us to identify the kinetics limitation for each type of electrode. Furthermore, by coupling the electrochemical process with *operando*-XRD, the structure evolution during lithiation is investigated in the perovskite anode to propose for the first time a possible mechanism based on three steps: insertion, where coexist pristine material and lithiated phase; irreversible lead conversion and Li-Pb alloying.

This work demonstrates that EIS is a testing tool that makes accessible the connection between electrochemical mechanism and electrode morphology and constituents.

Abbreviations, notations and chemical formulas

Li	Lithium
$LiFePO_4$	LFP – Lithium iron phosphate
Li-O_2 batteries	Lithium-oxygen batteries
$CH_3NH_3PbBr_3$	$MAPbBr_3$ – Methylammonium lead bromide perovskite
Li-Pb alloying	Lithium-lead alloying
Operando-XRD	*Operando* – X Ray Diffraction
EIS	Electrochemical Impedance Spectroscopy
IEA	International Energy Agency
CO_2	Carbon dioxide
UNFCC	United Nations Framework Convention on Climate Change
V_{ox}	Oxidative chemical reaction potential
V_{red}	Reduction chemical reaction potential
V	Cell voltage
V^0_{cell}	Open-circuit voltage
Emf	Electromotive force

W_{max}	Maximum electric energy delivered
ΔG	Change of free energy per mol
n	Number of electrons transferred during the reaction
F	Faraday constant
μ_A	Electrochemical potential of the anode
μ_C	Electrochemical potential of the cathode
Ni-MH batteries	Nickel–metal hydride batteries
Ni-Cd batteries	Nickel-cadmium batteries
Li-S batteries	Lithium-sulfur batteries
LIB	Lithium Ion Batteries
Li^+	Ion lithium
LMBs	Lithium metal batteries
TiS_2	Titanium disulfide
VO_x	Vanadium oxide (at different oxidation states)
Li_xMO_2	Transition metal oxides lithium
Co	Cobalt
Ni	Nickel
Mn	Manganessium
MoS_2	Molybdenum disulfide
$LiCoO_2$	Lithium cobalt oxide
$LiPF_6$	Lithium hexafluorophosphate
NMP	N-methyl-pyrrolidone
EES	Electrical energy storages

PVDF	Polyvinylidene fluoride
$Li_4Ti_5O_{12}$	LTO - lithium titanate
SEI	Solid Electrolyte Interface
TiO_2	Titanium dioxide
Na^+	Ion sodium
$LiNiO_2$	LNO - Lithium nickel oxide
$LiNi_{0.8}Co_{0.15}Al_{0.05}O_2$	NCA - Lithium nickel cobalt aluminium oxide
$LiMn_2O_4$	LMO - Lithium manganese oxide
$LiNi_{0.33}Co_{0.33}Mn_{0.33}O_2$	NMC - Lithium nickel manganese cobalt oxide
Fe	Iron
Cu	Cupper
Li_2O_2	Lithium peroxide
$LiMPO_4$	Lithium transition-metal phosphates
OER	Oxygen evolution reaction
ORR	Oxygen reduction reaction
$Li_{1-x}CoO_2$	LCO – Lithium cobalt oxide
EC	Ethylene carbonate
DMC	Dimethyl carbonate
DEC	Diethyl carbonate
EMC	Ethyl methyl carbonate
LiF	Lithium fluoride
$(CH_2OCO_2Li)_2$	Lithium ethylene dicarbonate
$Li_2(OCO_2(CH_2)_2OCO_2)_2$	Dilithium butylene dicarbonate

Contents

1

Introduction

Nowadays, it is impossible to imagine our society without the use of energy, it is important to all of us, for a variety of useful reasons. Over the past years, energy has been largely supplied by the consumption of fossil fuels, at the cost of a dangerous anthropogenic impact on the environment. According to the latest report of the International Energy Agency (IEA) with a share of more than 80%, and an increase of 2.1 % in 2017 (as show in **Figure 1.1**), in global CO_2 emissions related to energy, after three years with hardly any changes.[1]

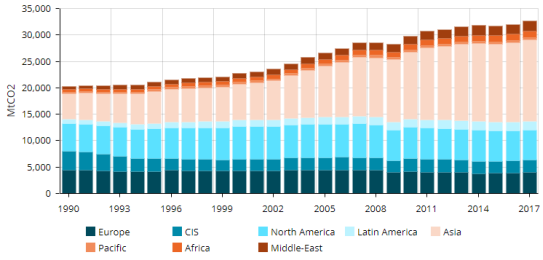

Figure 1. 1. World energy consumption between 1990 and 2017 by Global Energy Statistical Yearbook 2018. [1-2] (Reproduced with permission)

For this reason, the United Nations Framework Convention on Climate Change (UNFCC) calls to climate action to reduce greenhouse gas emissions rapidly and to strengthen the ability of

countries to build resilience and adapt to the impacts of climate change, ensuring adequate support for developing countries. The main goal is achieving to keep the average global temperature increment as close as possible to 1.5ºC and below 2ºC, through the enforcement of the Paris Agreement, the 2030 Agenda for Sustainable Development and the Sendai Framework for Disaster Risk Reduction.[3] Spain will not be able to comply with the commitments adopted in the Paris Climate Agreement, if not dispense with fossils fuels before decarbonizing the economy in 2050. This implies moving from fossil fuels towards renewable energy sources,[4] which represent only the 2.77 % of the world primary energy source at this moment. If a new energy economy is to emerge, it must be based on a cheap and environmentally friendly energy supply.

To such extent, it is of great importance to know how to transform the energy from sustainable sources such as solar power, wind or moving water, and what methods to store and transport energy from place to place at times we want to utilize it. Not only are they more-ecofriendly also unlimited. However, they present a big disadvantage: the intermittency of supply, which is subjected to time, season or weather conditions. Here electrochemical energy production can potentially provide a solution, by the use of devices, such as batteries, supercapacitors and fuel cells. In addition, these devices may operate with much higher efficiencies than combustion engines and related devices, due to the electrical conversion from chemical energy is not subject to undergoes lower thermodynamic energy losses.[2]

1.1. Batteries for electrochemical energy storage

Battery energy storage is the most widely used technology available for power system application, and many types of batteries are

commercialized. T. Reddy has defined a rechargeable battery as an electrochemical system that converts the chemical energy contained in its active materials into electrical energy by means of an electrochemical oxidation reduction (redox) reversible reaction.[5]

All batteries consist of two electrodes connected by an ionically conductive electrolyte, a separator and the current collectors. The more negative electrode of the cell, in the electrochemical scale, is designed as the anode, which is associated with oxidative chemical reactions, at the potential V_{ox}, that release electrons to external circuit, which is comprised of materials that can reversible store lithium ions (e. g. carbon, transition metal oxides and alloying metals). On the other part, the cathode is the more positive one, where reductive chemical reactions, at the potential V_{red}, take place when it gains electrons from external circuit. The separator is necessary to avoid the electrons at the separate electrodes come internally into contact when the battery is processed. If this happens both electrodes would be at the same potential and the cell will be in short circuit and become useless.

The amount of electric energy that the cell can deliver is a function of the cell potential (V) and charge capacity (Ah kg^{-1}), which in turn depend on the chemistry of the battery. The equilibrium cell potential is given by the difference of potentials of cathode and anode:

$$V_{cell}^{0} = V_{red} - V_{ox} \qquad (1.1)$$

When the battery is in equilibrium, the potential difference between its terminals, or open-circuit voltage (OCV), V_{cell}^{0}, is understood as the electromotive force, *emf*. This chemical driving force across the cell is given by the change of free energy of the reaction, determined by the free energies of formation of products and reactants.

$$W_{max} = \Delta G = -nFV_{cell}^{0} \quad (1.2.)$$

Where W_{max} represents the maximum electric energy delivered by the chemicals, ΔG is the change of free energy per mol when the reactions progress, n is the number of electrons transferred during the reaction and F is the Faraday constant. V_{cell}^{0}, the electrode cell potential difference also can defined by chemical electrode potentials: μ_A and μ_C, for anode and cathode, respectively, which depend on the chemistry that occurs at each electrode.

Following, in the **Figure 1. 2**, it is shown the principle of operation of electrochemical battery. Here, the free energy available is due to the oxidation reaction at the anode, which increases the state of charge of a metal M, at the standard potential of the oxidation reaction occurs, V_{ox}.

$$M \rightarrow M^{+} + e^{-} \qquad V = V_{ox} \quad (1.3.)$$

And at the cathode reduction reaction decreases the state of charge of a metal oxide B, it takes place at reduction potential, V_{red}

$$B + M + e^{-} \rightarrow BM \qquad V = V_{red} \quad (1.4.)$$

During the discharge process the semi-reactions that take place in both electrodes lead to a reduction in the voltage differential between both. On the contrary, the charge process increases this voltage difference.

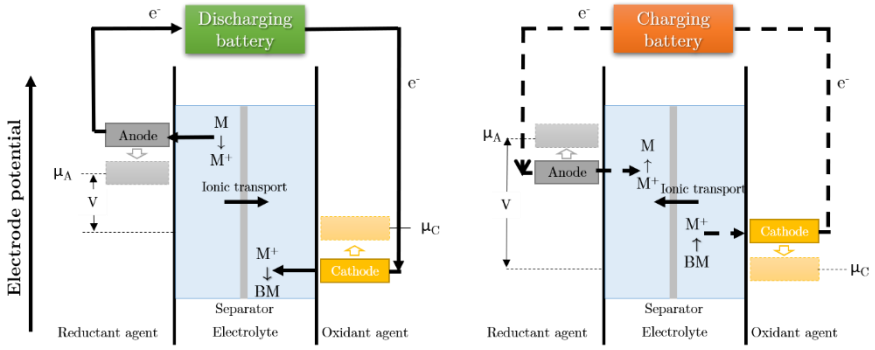

Figure 1. 2. Principle of operation of electrochemical battery during (a) discharging and (b) charging process. Circuit energy diagram of Li-ion battery. μ_A and μ_C are the electrochemical potential of the anode and cathode, respectively. And the electrochemical potential to the end the process has been shown by dotted lines.

Li-ion batteries is a mainstream technology to power an increasingly diverse range of applications, from cars to microchips. Despite the simplicity of this device, the lack of suitable electrode materials and electrolytes, together with difficulties in understanding what happen in the interfaces, has been the cause that their slow development, for example in the electric vehicles.

1.1.1. Batteries chemistry

The amount of electrical energy per mass or volume that a battery can deliver is a function of the chemistry of the system. The most remarkable rechargeable batteries are lead-acid, Ni-Cd or their successor: Ni-MH and lithium-metal that evolved to implement the lithium-ion battery technology. Also, the new configurations such as Li-Sulfur or Li-oxygen batteries must be mentioned. In **Figure 1. 3** different existing storage technologies are compared as a function of the gravimetric energy versus volumetric energy they are able to provide.[6 - 7] The goal in this research field is to develop a battery

whose properties include light technology with high specific power, it means high loading capability, also stability and with long cycle life.

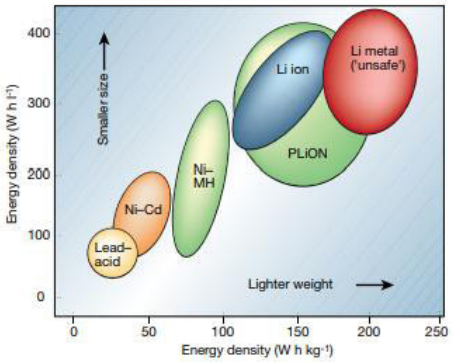

Figure 1. 3. Comparison of the different battery technologies in terms of gravimetric energy versus volumetric energy. [6](Reproduced with permission from Armand, M.; Tarascon, J., Issues and challenges facing rechargeable batteries. Nature 2001, 414, 359-367).

In 1859, lead-acid batteries were developed, characterized by their fast response times, small daily self-discharge rates, relatively high cycle efficiencies (63-90%). They are relatively cheap and easy to manufacture. But this technology had significant drawbacks, such as its heavy weight, which limits its energy density and short lifetime, risk of hydrogen evolution and their heavy metal use. Their most common application is starting engine, electric and hybrid vehicles and standby emergency power.

The only rechargeable battery until 1899 was lead acid. Then, Ni-Cd batteries broke into the market, but the negative effects of cadmium on human health and memory effect, which limits the charging voltage and capacity if the battery was not fully discharged previously, were the cause because they failed. Nickel metal hydride batteries (Ni-MH) mostly replaced them in the 1900s. Ni-MH anode is constituted by a metal hydride with adsorbed hydrogen, which came up with higher energy density than previous one, resulting in a

higher capacity or longer service life, and are more environmentally friendly. So, they are used in consumer electronic devices such as phones or computers. As well as, they are considered candidates for use in electric vehicles.

The scientific community continued seeking for lighter options, capable of giving higher energy densities. From mid-1970s, sodium-sulfur battery technology has been commercialized, which attracted attention for grid applications, accounting for 315 MW of worldwide discharge power capacity. Although they have a high energy density, acceptable charge/discharge efficiency, long cycle life, temperature stability and use cheap and easy to recycle components, their performance is reduced because part of the stored energy is used to maintain the operating temperature in the range of 300 – 350 ºC. On the other hand, redox flow batteries have to be pointed out because of their great advantage: the power is independent of their storage capacity as, in this case, it is determined by the size of the electrodes, the number of cells, the concentration and the amount of electrolyte. Among the disadvantages there is the fact that they show low performance resulting from non-uniform pressure drops and the reactant mass transfer limitation, high manufacturing cost and systems requirements.

Thereafter, lithium metal was found to be a good candidate because of it is lightest of all metals with the greatest electrochemical potential and offers the largest energy density per kilogram. However, it was studied the changes that the lithium electrode suffers on itself during the cycling resulted in potential fire danger. Then a safer technology which operates at room temperature and with non-metallic lithium battery emerge as an alternative to replace them: lithium-ion batteries. Due to offering superior energy efficiency, high power density, fast charge and discharge capability, low weight and long cycle life these batteries have attracted the attention to use them in portable devices. Nevertheless, they have some disadvantages such as high cost due to overcharging protection and risk of capacity loss

or thermal runaway. It should be pointed out that there are two specials cases: Li-S and Li-O_2 batteries. In the next section will be complemented and expanded to take account of Li-ion batteries specific characteristic.[6]

1.2. Lithium ion Batteries (LIB)

Li-ion batteries were a natural evolution from lithium metal battery technology and the deep knowledge of intercalations chemistry developed by solid-state chemist in the 1970s. Firstly, lithium was regarded as an excellent anode with the extra-high capacity (3860 mAh g^{-1}) and the lowest negative electrochemical potential (−3.04 V *vs* the standard hydrogen electrode). In 1980s, Moli Energy commercialized the first-generation Lithium Metal Batteries (LMBs) with a high energy density of 100-200 Wh kg^{-1} and 200-300 Wh l^{-1}. In this first stage, the intercalated cathodes that were used (electrochemical incorporation of Li^+ within the structure of host materials, more details are given in the following sections), such as TiS_2, VO_x, Li_xMO_2 (where M is Co, Ni, or Mn), and MoS_2, operated properly. Nevertheless, LMBs were not viable because Li metal forms dendrites which can cause short circuits, start a thermal run-away reaction on the cathode, and a risk of explosion hazards of the batteries. Also, they have poor cycle life.[8-9] So, it was replaced by the secondary anode materials.

One of the major characteristics of Li-ion batteries is that the same ion, Li^+, participates at both electrodes, it means that insertion/extraction is reversible from the electrode material coupled with addition/removal electrons. The first commercialized Li-ion battery was realised in 1991 by Sony. The electrode materials in this cell were $LiCoO_2$ as the positive electrode, which was identified by Goodenough's group as a higher potential cathode for the electrochemical insertion/extraction of lithium[10], and carbon as the

negative electrode, with $LiPF_6$ dissolved in a mixture of propylene carbonate and diethyl carbonate as the electrolyte. The energy it stored around 180 Wh kg^{-1} at an average voltage of 3.8 V, being five times more that stored by the older lead–acid batteries.

Nowadays, their capacity has more than doubled, becoming the most popular power sources; and in the recent years, they have begun to employ in electrical energy storages (EES), like as in energy plants. In 2013, the global battery market accounted for $54 billion. And it is estimated to be achieved a global market $213.5 billion by 2020.[6] However, in order for the LIB's become the batteries of the future, they must overcome problems such as safety issues relative to combustible materials, electrolyte decomposition, and they would need to reduce their carbon footprint.[11]

1.2.1. Anode and cathode materials

Each electrode is made from particles (~80% by mass) with which Li^+ ions react and into which the lithium inserts. The electrolyte is a chemical solution that provides a medium of ion transport between the electrodes, but electronically nonconductive. Anode and cathode are electrochemically isolated to prevent short circuit for a separator, which is a microporous polyethylene or polypropylene separator film, permeable to the electrolyte to provide ionic conductivity. The current collectors are metals in contact with the electrodes that receive a flow of electrons from an external circuit to take place the oxidation/reduction reaction on the electrodes. Aluminium and copper sheets for the cathodes and the anodes, respectively. When the electrodes are prepared, a binder is used to hold the active material particles together and in contact with the current collectors, typically ~10% by weight of polyvinylidene fluoride (PVDF). And, electronic conductive material is used to enhance the electrical conduction into the electrodes (~5-10% by wt. of hard carbon).

In order to be considered suitable candidates for LIBs, active materials should comply with reversible capacity, good ionic and electrical conductivity, long cycle life, high rate of lithium diffusion into active material and, as well as low cost, safety and eco-friendly. In next section, the most relevant anode and cathode materials are presented with their advantages and disadvantages. In the majority the configurations, active materials undergo a topotactic reaction where lithium ions are reversibly removed or inserted into the host without a significant structural change to the host during the charged and discharged. However, there may exist also alloying reactions between lithium and another metal and conversion processes, where active materials experiment a solid-state redox reaction during lithiation/delithiation, corresponding to changes in their crystalline structure. Reactions involves a huge volume expansion, it entails a high mechanical instability. The different mechanisms can be seen in **Figure 1. 4.**

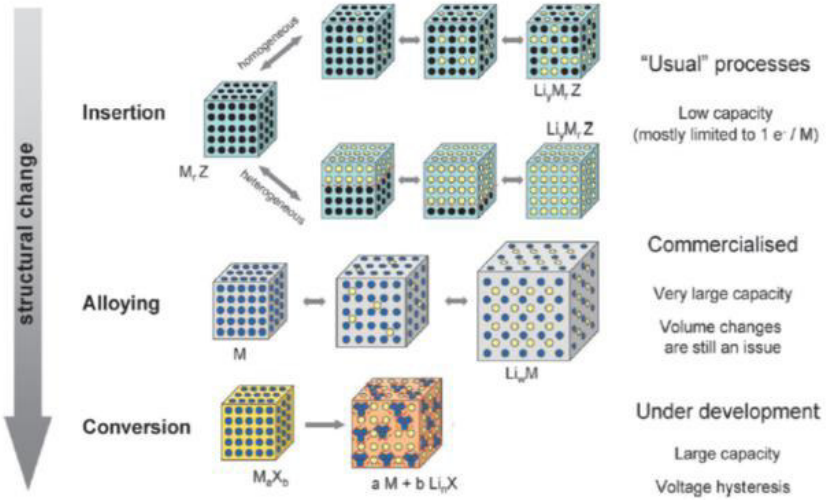

Figure 1. 4. A schematic representation of the different reaction mechanisms observed in electrode materials for lithium batteries. Black circles: voids in the crystalstructure, blue circles: metal and yellow circles: lithium.[12] (Reproduced with permission from Palacin, M. R., Recent advances in rechargeable battery materials: a chemist's perspective. Chem. Soc. Rev. 2009, 38 (9), 2565-2575).

The great effort made in all areas has allowed the exponential improvement experimented by lithium-ion batteries in recent years, which allows them to be considered as the main storage energy solution in many applications. However, the most important breakthroughs come from new materials. Below is a summary on the innovative materials classified in three groups, depending on their Li-ion battery reaction mechanism: intercalation/de-intercalation, alloy/de-alloy and conversion materials.

Insertion electrodes

The most important suitable compounds among anode materials due to a high electrical conductivity and Li^+ transport, apart from properties of low cost, abundance, easy processability, chemical stability, low delithiation potential vs. Li/Li^+ and relative low volume change during lithiation/delithiation and relatively ecofriendly are the carbonaceous materials such as carbon, graphite, soft-carbons and hard carbons.[7] Electrochemical activity in carbon comes from the intercalation of Li between the graphene planes, up to 1 Li atom per 6 C can be stored in this way, corresponding to 372 mAh g^{-1}, theoretically.[13] As alternative is the spinel $Li_4Ti_5O_{12}$ (LTO).[14] Despite its low specific capacity (150 mAh g^{-1} at 1.50 V vs. Li/Li^+) compared to graphite, its good performance at very high rates, it shows a long cycle life derived from the zero-strain intercalation mechanism, coupled to the safety enhancement derived from a higher potential with no SEI formation, make it attractive for implementation in batteries for transport applications. Other titanium oxides (polymorphs of TiO_2) are possible candidates, too.[15]

Most efforts made in insertion electrodes have being devoted to positive electrode materials. The intercalation cathode materials are divided in layered oxides, spinel structures and phospho-olivines (see **Figure 1. 5**). All they have crystalline structures that enable

reversible lithium insertion/extraction at practical voltage values vs. Li^+/Li.

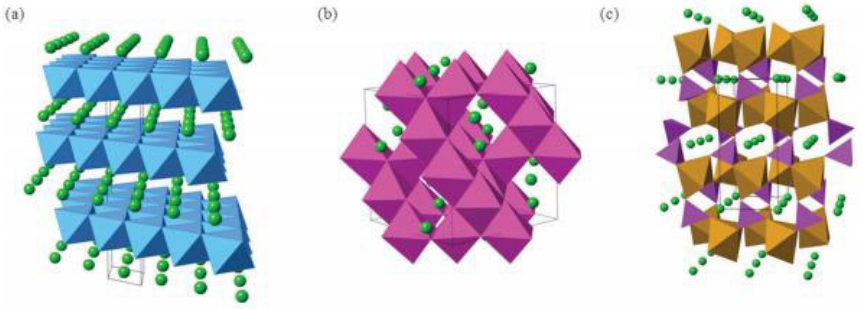

Figure 1. 5. Representative crystal structures of cathode materials for lithium-ion batteries: (a) layered a-$LiCoO_2$; (b) cubic $LiMn_2O_4$ spinel; (c) olivine structured $LiFePO_4$. Black lines demarcate one unit cell in each structure. Structural representation of three types of insertion materials (green spheres are lithium ions).[16] (Reproduced with permission from Islam, M. S.; Fisher, C. A. J., Lithium and sodium battery cathode materials: computational insights into voltage, diffusion and nanostructural properties. Chem. Soc. Rev. 2014, 43 (1), 185-204. Published by The Royal Society of Chemistry).

The most commercially successful was $LiCoO_2$ (LCO), where the Co and Li are in octahedral sites occupy alternating layers and form a hexagonal symmetry, the two-dimensional paths exist along the ab direction, which allows for diffusion of lithium ions (see Figure 1. 5). LCO is a very attractive because of it shows relatively high theoretical specific capacity of 274 mAh g^{-1}, low self-discharge, high discharge voltage, and good cycling performance. Nevertheless, they have high cost and fast capacity fade at high currents rates. Furthermore, it has low thermal stability, so Co^{4+} from delithiated $Li_{1-x}CoO_2$ can oxidize the organic solvents of the battery electrolyte, especially upon heating and can lead to the ignition of the battery.[17]

$LiNiO_2$ (LNO) presents similar structural, theoretical specific capacity of 275 mAh g^{-1} and thermal instabilities than $LiCoO_2$, but

lower cost because of lack of Co. However, the two-dimensional paths in $LiNiO_2$ usually are partially blocked by excess nickel atoms that limit the Li-ion diffusion rate. A partial substitution of Ni with Co in order to avoid blocking the Li sites during synthesis and with Al in order to improve both thermal stability and electrochemical performance. The resulting $LiNi_{0.8}Co_{0.15}Al_{0.05}O_2$ (NCA) cathode material has high discharge capacity (200 mAh g^{-1}) which is now used in the battery for some models of Tesla electric cars.[18]

$LiMnO_2$ (LMO) is also a promising alternative to $LiCoO_2$ cathode material in terms of toxicity, performance and cost. When lithium insertion/extraction they tend to transform into $LiMn_2O_4$ with spinel structure, that has lower capacity and voltage. Stabilization of oxides containing manganese has been achieved by partial substitution of Mn by Co and Ni. The optimal composition with the best compromise between thermal stability and performance has been found for $LiNi_{0.33}Co_{0.33}Mn_{0.33}O_2$ (NMC) which is widely used in the battery market because Mn is much cheaper and less toxic compared to Co or Ni and shows reversible specific capacity as high as 234 mAh g^{-1} and good cycle stability.[19]

More recently, a high-capacity $LiNi_{0.8}Co_{0.06}Mn_{0.14}O_2$ with a dual concentration gradient was reported.[20] Each particle consists of Ni-rich concentration in the particle core and the Mn concentration on the particle surface. This positive electrode shows improved overall electrochemical properties such as reversible capacity, cycle life, and rate capability and thermal stability. We have performed in collaboration with Prof. Yang-Kook Sun, although it is not included in the present thesis.[20]

So also, the spinel $LiMn_2O_4$ (LMO) is interesting in terms of low cost, and environmental friendliness of Mn, with a moderate capacity of 120 mAh g^{-1} and an average voltage of 3.8 V vs. Li^+/Li. However, it shows insufficient long-term cyclability has been attributed mainly to Mn dissolution and destabilization of the spinel structure.

Finally, Lithium transition-metal phosphates $LiMPO_4$ (M: Fe, Mn, Co, Ni) with olivine-type structure constitute a group of polyanionic compounds safer alternatives and were proposed by Goodenough's group.[21] The polyanionic $LiFePO_4$ is the most representative for the olivine structure and call the attention of the battery scientific community by its thermal stability, high power capability, competitive cost and presumable low toxicity. It provides 170 mAh g^{-1} at 3.50 V vs. Li/Li^+. Although it presents disadvantages like its relatively low average potential, a low electron conductivity and slow diffusion of Li^+, they can be improved by coating it with conducting agents such as carbon or polymer. The relevant properties of $LiFePO_4$ and the mechanisms of charge transport and phase transformation of this material are described in Chapter 2.

Alloying

Materials that store charge via alloying reactions tend to display high capacities (i.e. Si = 3579 mAh g^{-1}, Sn = 993 mAh g^{-1}), but have poor cycle life at high active loadings, due to the dramatic volume changes during the alloying process, at least 400 %, which damages electrode integrity. The latest researches have developed complex or nanocomposite battery electrode materials, which display a combination of different charge storage mechanisms, both insertion and conversion/alloying mechanisms. These materials provide a balance between moderate structural changes and reasonable high capacities, with longer cycle life stability.[22-23]

Conversion mechanism

Transition-metal oxide (M_xO_y, M=Fe, Co, Ni, Mn, Cu, etc.) are noted to be capable of incorporating more than one Li^+ per metal atom, leading to an increase in electrochemical capacities than carbonaceous

anode. In spite of the great capacities and low cost, the main drawback is the poor energy efficiency, high hysteresis between charge and discharge profiles, and the large volumetric change. It is due to this mechanism involves a completed change in the chemical identity of the reactants (MO + 2 Li^+ ↔M+LiO_2). It is believed that this reaction is not practical because it occurs at low potentials, below threshold of reduction reaction of most the solution species used in Li-ion batteries, and it is not possible to guarantee really stable passivation for these reactions.[23-24]

New electrode materials for lithium-based batteries

Li-O_2 batteries

It is important to look beyond the horizon of LIBs and explore alternative rechargeable batteries that might exceed what lithium-ion batteries could deliver. Approaches based on new chemistry are necessary to increase the energy density in batteries, such as Li-O_2 batteries, which is obtained by combing lithium metal anode with a O_2 permeable cathode. This concept was proposed by Abraham and Jang in 1996.[25] The lithium air battery is expected to provide theoretical energy density (~3500 Wh kg^{-1}), but their development is hindered by the complexity of the chemistry at play. Currently Li–O_2 batteries are classified into four architectures based on the electrolyte used: aprotic, aqueous, hybrid, and solid-state systems.[26]

The energy is stored by the direct reaction, in nonaqueous or aqueous system, between Li^+ ions and O_2 in a porous electrode that acts as an electric conductive substrate and is based on the oxygen reduction reaction (ORR) during discharge forming the discharge product Li_2O_2 on the cathode surface, which is electrochemically decomposed to release oxygen during oxygen evolution reaction (OER) in the charging. Since lithium oxides products are insoluble in the electrolyte, they are stored in the carbon electrode pores, and the cell

discharge ends when these pores are filled completely with the oxides. The capacity of the oxygen electrode is dependent on the specific area of the carbon electrode. Li_2O_2 formation involves some challenges such as is a solid electronically insulator, which can cause a high overpotential in OER, the use of a catalyst in the carbon cathode can improve the recharge efficiency, being the most popular strategy the addition of heterogeneous catalysts that dispersed in the carbon electrode have improved the performance of the battery. Among them noble metals and metal oxides have been widely investigated.[27-28]

The main issues that require improvement to achieve higher capacities are: (i) a nonaqueous electrolyte that is stable to assist the peroxide radical attachment with high oxygen solubility, (ii) an excellent catalyst for the reduction of Li_2O_2, (iii) the suppression of lithium dendrite formation and (iv) protection from CO_2 and H_2O in the ambient air.[29]

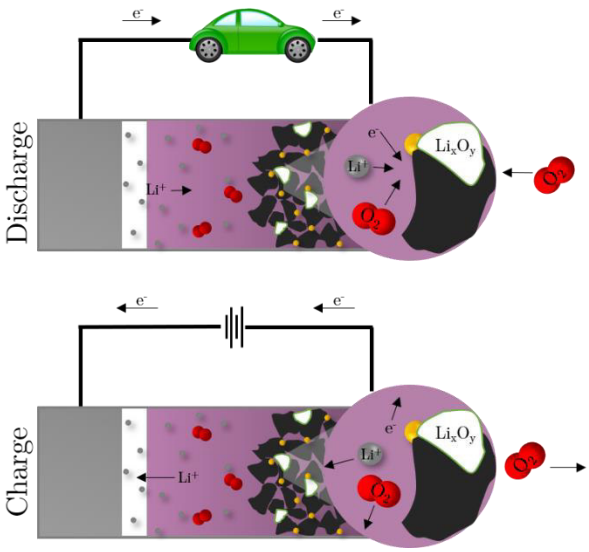

Figure 1. 6. Schematic of Li-O2 batterr. Grey represents a Li metal negative electrode, white separator, purple the organic electrolyte, black porous carbon positive electrode, yellow a catalyst, red is oxygen molecule and white forms the discharge product.

$CH_3NH_3PbBr_3$ anodes

Studies on the already well-known Li-batteries are focusing on battery materials and architectures, enhancing the stability and safety, and lowering the cost through innovative materials. Towards this end, recent publications have proposed a promising anode material to improve batteries performance: hybrid lead halide perovskites.[30-32] Perovskite may be able to offer both improved capacity and lower cost. Since 2009, organic-inorganic hybrid perovskites have attracted tremendous scientific attention, when the first hybrid perovskite application in solar cells was reported.[33] Due to its great properties (high absorption coefficient, low charge-carrier recombination rates and easy and low cost of cell fabrication by chemical methods and much abundance of raw materials), which have allowed achievement of the highest power conversion efficiencies of 22.7% certified by NREL.[34] Now, and also because of the ability to host extrinsic elements, such as Li^+ or Na^+, these materials have potential for battery applications. The first report that supports this statement a storage capacity of ~330 mAh g^{-1} for $MAPbBr_3$ was reported by Xia et al.[30]

These first publications, aimed at determining the viability of hybrid halide perovskites as storage energy material, were based on *ex-situ* experiments or theoretical studies.[30, 35-36] In this thesis (see Chapter 6) a possible mechanism for the 3D perovskites anodes is proposed, which is even supported by *in-situ* experimental techniques, specifically *in-situ* X-Ray Diffraction. The loss of the $MAPbBr_3$ structure during the cycle is confirmed, turning insertion mechanism into conversion and alloying mechanism.

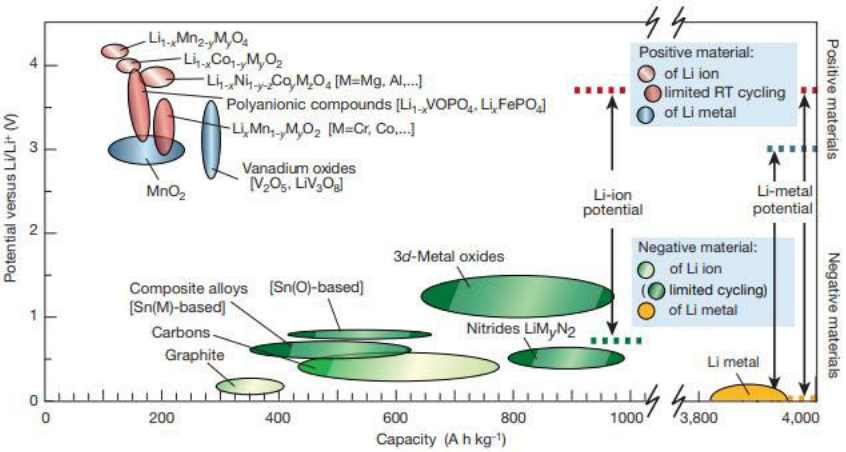

Figure 1. 7. Voltage *vs.* Capacity for anodes and cathodes materials considerate for the next generation of rechargeable Li-ion batteries.[6] (Reproduced with permission from Armand, M.; Tarascon, J., Issues and challenges facing rechargeable batteries. Nature 2001, 414, 359-367).

1.2.2. Electrolyte

The electrolyte is a pure ionic conductor that physically separates the anode from the cathode, whose main role is to enable a fluent and fast transport of Li ions thought the separator that is soaked with it. The electrolytes, which are used in Li-ion batteries, are based on non-aqueous solvent.

In this thesis the electrolyte that has been used is a conventional electrolyte. It consists of $LiPF_6$ dissolved in a mixture of aprotic, polar carbonate solvents because of they offer a high ionic conductivity $4 \cdot 10^{-3}$ S cm^{-1}, a high dielectric constant, which enables them to solvate lithium salts and are stable in voltage working window where it does not discompose or polymerization, usually they are limited to 4.60 V vs. Li/Li^+.

Usually, the most useful solvents are ethylene carbonate (EC), which has a high dielectric constant. Since its melting point is relatively

high (36.4°C), low viscosity co-solvents are typically used. These are most typically linear alkyl carbonates, such as dimethyl carbonate (DMC), diethyl carbonate (DEC) or ethyl methyl carbonate (EMC). The presence of EC is critical for the reversibility of the reaction at the negative electrode because it decomposes reductively on the graphite surface upon first charging at around 0.80 V vs. Li/Li^+, forming an SEI layer of decomposition products, it is examined in depth in the next section.

1.2.3. Solid Electrolyte Interface (SEI)

In 1979, it was proposed by E. Peled[37], the SEI model that is valid for all alkali metals and alkaline earths in non-aqueous batteries systems. The solid electrolyte interface model proved that the instantaneously formation of SEI film upon contact of the metal with the solution, due to the reduction of the electrolyte and production of insoluble Li species at the surface of anodes of lithium-ion batteries, is profitable for operating Li-ion batteries. The reactions on the electrode/electrolyte interface causes irreversible capacity loss, which directly reduce the available energy of the LIBs.

The layer acts as an interphase between the anode and the electrolyte solution and has the properties of a solid electrolyte with relatively high electrical resistance and high cation selectivity and permeability. Its thickness is usually from 1 to 10 nm, has high strength and tolerance to expansion and contraction stresses during the charging/discharging, respectively. And also, it is insoluble in the electrolyte and stable in the operating temperatures and potentials range.[38] The SEI layer is determining factor in the safety, power capability, morphology of lithium deposits, and cycle life of the batteries. SEI film helps to prevent the transfer of electrons from the electrode to the solution in lithium battery, after its formation, but it should be able to let lithium ions go through and passivate the

electrode surface from further reactions and the charged electrode from corrosion.

The morphology of SEI is very complex and varies with electrolyte composition, described as a thin heterogeneous film of organic and inorganic components. Its multicomponent composition is not fully ascertained, but inorganic compounds have been identified as the products of the reduction of salts anions such as LiF and $LiPF_x$, while the decomposition of the electrolyte carbonate solvents can lead to formation of insoluble Li_2CO_3, which is considered to be one of the SEI main components formed during the lithiation−delithiation process.[39] And partially soluble carbonates $Li_2(OCO_2(CH_2)_2OCO_2)_2$, $(CH_2OCO_2Li)_2$ have been identified as its main components.[40-43]

Intensive research is currently carrying out to improve SEI properties and to develop an artificial SEI to avoid any growth over repeated charge/discharge cycles and long term storage, as well as dissolution at elevated temperatures.[44]

1.3. Outline and scope

1.3.1. Objectives

The main objective of this Thesis is to understand and contribute to the development of a new generation of Lithium Batteries with better performance. In this context, the author worked on different materials, such as $LiFePO_4$ cathodes, Li-O_2 batteries and methylammonium lead bromide perovskite battery anodes. Being the last one where significant effort have been made because it is the most innovative anode in the bibliography at this moment.

In this research project, electrochemical impedance spectroscopy technique has been employed to probe kinetic limitations in charging of battery electrodes. It allows us to identify the principal kinetic limitation that prevents the full charge of the electrode, which can be

relative to ion diffusion or the kinetics of the reduction reaction itself. Solid-state kinetic models of transport and reaction have been proposed for each of the studied electrodes to explain the reaction- or diffusion-limited mechanism, whether intercalation, conversion or alloying electrodes.

To reach this goal several objectives have been target:

- Synthesis, optimization, and structural and morphological characterization of active materials for electrodes lithium batteries.
- Electrochemical characterization of electrodes as anodes or cathodes in lithium ion half-cells.
- Development of different Impedance Models to explain the electrode behavior during the cycling.
- In case of novel $CH_3NH_3PbBr_3$ anodes, few studies relative to the mechanism that is taking place are reported in the bibliography. It is for this reason, that its mechanism was elucidated by means of *operando* techniques: performing an impedance study and XRD analysis.

1.3.2. Structure of the Thesis

This Thesis consists of seven chapters and it has been organized according to the requirements on a compendium of articles, which have been published in relevant international publications.

First chapter is a general introduction to the lithium ion batteries fundamentals, materials and battery performance, and a brief explanation of the techniques used for the characterization of the batteries. Throughout the next five chapters are presented the different electrodes that have been studied during the investigation. Finally, Chapter 7 summarizes the main conclusions of this Thesis and possible future researches are suggested.

Here, an overview of each publication is presented:

1. **Chapter 3: $LiFePO_4$ particle conductive strategies for improving cathode rate capability.**

   In this manuscript, in order to power performance of lithium iron phosphate (LFP) cathodes, the matrix was modified with the addition to the LFP particles of an electric conductive carbon or polymer. A deep study of impedance allowed us to elucidate the role of the additives. Not only do they improve the transfer of charge, but also favor the lithiation/delithiation in the phosphate matrix.

2. **Chapter 4: Oxygen Reduction Reaction Promotes Li^+ Desorption from Cathodes Surface in Li-O_2 Batteries.**

   For Li–O_2 cathodes, the energy is stored by the direct reaction between Li^+ ions and O_2 in a porous electrode that acts as an electric conductive substrate. A novel equivalent circuit model is proposed, which allows interpretation of the measurements of impedance spectroscopy for Li-O_2 batteries. During discharge mechanism different electrochemical process are identified: (i) interfacial phenomena, (ii) electrochemical double layer capacitance related to the Li^+ adsorption, and (iii) oxygen reduction reaction chemical capacitance related phenomena only at voltages and frequencies below 2.7 V and 10 mHz.

3. **Chapter 5: Methylammonium Lead Bromide Perovskite Battery Anodes Reversible Host High Li-ion Concentrations.**

   Here, promising preliminary results and the early understanding of the electrochemical charging of

nanostructured hybrid perovskite $CH_3NH_3PbBr_3$ has been reported. Intercalation anode exhibits a stable specific capacity and partially reversible ~200 mA h g^{-1}, and molar contents as high as x = 3 (moles lithium per mol of methylammonium). Main advantages are its high insertion concentration x>>1.

4. **Chapter 6: Organohalide Perovskite are Fast Ionic Conductors.**

   Methylammonium lead bromide perovskite is used in solar cells, but due to the multicomponent environment in all-solid-state configurations, the ion diffusivity analysis is ambiguous. So that battery configuration, in which the electrolyte is in contact with the anode, a reservoir of Li^+ is forced to intercalate and migrate within the perovskite electrode, and then impedance study allows us calculate ion diffusion kinetics. Confirming the superionic intrinsic property of organohalide perovskites.

5. **Chapter 7: Probing the 3-step Lithium Storage Mechanism in $CH_3NH_3PbBr_3$ Perovskite Electrode by Operando-XRD Analysis**

   In this manuscript the mechanism that take place between lithium and organic-inorganic halide perovskite has just recently proposed, using an *operando*-XRD. According to our results the lithiation of $CH_3NH_3PbBr_3$ entails three reaction steps: (1) the initial Li^+ insertion into the perovskite phase in which pure perovskite and lithiated phases, $Li_xCH_3NH_3PbBr_3$ coexist ($0 < x < 1$), (2) the perovskite conversion reaction leading to the formation of metallic lead ($1 < x < 2$), which is an irreversible process, and finally, (3)

the alloying of lithium with the metallic lead previously formed. It is in accordance to previous electrochemical results.

This proposal for lithium storage gives a complete perspective of the complex structural environment involving the use of perovskite materials as electrodes for Li-ion batteries.

1.4. References

1. https://www.elboletin.com/noticia/160911/economia/los-combustibles-fosiles-acaparan-el-80-de-la-demanda-mundial-pese-al-tiron-renovable.html.
2. Winter, M.; Brodd, R. J., What are batteries, fuel cells, and supercapacitors? ACS Publications: 2004.
3. https://unfccc.int/achieving-the-sustainable-development-goals-through-climate-action.
4. http://www.europapress.es/sociedad/medio-ambiente-00647/noticia-espana-debe-prescindir-combustibles-fosiles-cuanto-antes-descarbonizar-economia-2050-expertos-20171214114955.html.
5. Reddy, T. B., *Linden's Handbook of Batteries*. Fourth ed.; McGraw-Hill Education: 2011.
6. Armand, M.; Tarascon, J., Issues and challenges facing rechargeable batteries. *Nature* **2001,** *414*, 359-367.
7. Yoo, H. D.; Markevich, E.; Salitra, G.; Sharon, D.; Aurbach, D., On the challenge of developing advanced technologies for electrochemical energy storage and conversion. *Mater. Today* **2014,** *17* (3), 110-121.
8. Nitta, N.; Wu, F.; Lee, J. T.; Yushin, G., Li-ion battery materials: present and future. *Mater. Today* **2015,** *18* (5), 252-264.
9. Cheng, X.-B.; Zhang, R.; Zhao, C.-Z.; Zhang, Q., Toward Safe Lithium Metal Anode in Rechargeable Batteries: A Review. *Chem. Rev.* **2017,** *117* (15), 10403-10473.
10. Mizushima, K.; Jones, P.; Wiseman, P.; Goodenough, J. B., LixCoO2 (0< x<-1): A new cathode material for batteries of high energy density. *Mater. Res. Bull.* **1980,** *15* (6), 783-789.
11. Armand, M.; Tarascon, J.-M., Building better batteries. *Nature* **2008,** *451* (7179), 652.

12. Palacin, M. R., Recent advances in rechargeable battery materials: a chemist's perspective. *Chem. Soc. Rev.* **2009,** *38* (9), 2565-2575.
13. Huggins, R., *Advanced batteries: materials science aspects*. Springer Science & Business Media: 2008.
14. Yi, T.-F.; Yang, S.-Y.; Xie, Y., Recent advances of Li 4 Ti 5 O 12 as a promising next generation anode material for high power lithium-ion batteries. *J. Mater. Chem. A* **2015,** *3* (11), 5750-5777.
15. Madian, M.; Eychmüller, A.; Giebeler, L., Current Advances in TiO2-Based Nanostructure Electrodes for High Performance Lithium Ion Batteries. *Batteries* **2018,** *4* (1), 7.
16. Islam, M. S.; Fisher, C. A. J., Lithium and sodium battery cathode materials: computational insights into voltage, diffusion and nanostructural properties. *Chem. Soc. Rev.* **2014,** *43* (1), 185-204.
17. Dahn, J. R.; Fuller, E. W.; Obrovac, M.; von Sacken, U., Thermal stability of LixCoO2, LixNiO2 and λ-MnO2 and consequences for the safety of Li-ion cells. *Solid State Ionics* **1994,** *69* (3), 265-270.
18. Chen, C.; Liu, J.; Stoll, M.; Henriksen, G.; Vissers, D.; Amine, K., Aluminum-doped lithium nickel cobalt oxide electrodes for high-power lithium-ion batteries. *J. Power Sources* **2004,** *128* (2), 278-285.
19. Shaju, K. M.; Bruce, P. G., Macroporous Li (Ni1/3Co1/3Mn1/3) O2: A High-Power and High-Energy Cathode for Rechargeable Lithium Batteries. *Adv. Mater.* **2006,** *18* (17), 2330-2334.
20. Park, K.-J.; Lim, B.-B.; Choi, M.-H.; Jung, H.-G.; Sun, Y.-K.; Haro, M.; Vicente, N.; Bisquert, J.; Garcia-Belmonte, G., A high-capacity Li [Ni 0.8 Co 0.06 Mn 0.14] O 2 positive electrode with a dual concentration gradient for next-generation lithium-ion batteries. *J. Mater. Chem. A* **2015,** *3* (44), 22183-22190.

21. Padhi, A. K.; Nanjundaswamy, K. S.; Goodenough, J. B., Phospho-olivines as positive-electrode materials for rechargeable lithium batteries. *J. Electrochem. Soc.* **1997,** *144* (4), 1188-1194.
22. Liu, D.; Liu, Z. j.; Li, X.; Xie, W.; Wang, Q.; Liu, Q.; Fu, Y.; He, D., Group IVA Element (Si, Ge, Sn)-Based Alloying/Dealloying Anodes as Negative Electrodes for Full-Cell Lithium-Ion Batteries. *Small* **2017,** *13* (45), 1702000.
23. Bresser, D.; Passerini, S.; Scrosati, B., Leveraging valuable synergies by combining alloying and conversion for lithium-ion anodes. *Energ. Environ. Sci.* **2016,** *9* (11), 3348-3367.
24. Cabana, J.; Monconduit, L.; Larcher, D.; Palacin, M. R., Beyond intercalation-based Li-ion batteries: the state of the art and challenges of electrode materials reacting through conversion reactions. *Adv. Mater.* **2010,** *22* (35), E170-E192.
25. Abraham, K.; Jiang, Z., A polymer electrolyte-based rechargeable lithium/oxygen battery. *J. Electrochem. Soc.* **1996,** *143* (1), 1-5.
26. Lu, J.; Li, L.; Park, J.-B.; Sun, Y.-K.; Wu, F.; Amine, K., Aprotic and Aqueous Li–O2 Batteries. *Chem. Rev.* **2014,** *114* (11), 5611-5640.
27. Scrosati, B.; Abraham, K.; van Schalkwijk, W. A.; Hassoun, J., *Lithium batteries: advanced technologies and applications*. John Wiley & Sons: 2013; Vol. 58.
28. Imanishi, N.; Luntz, A. C.; Bruce, P., *The lithium air battery: fundamentals*. Springer: 2014.
29. Bruce, P. G.; Freunberger, S. A.; Hardwick, L. J.; Tarascon, J.-M., Li–O 2 and Li–S batteries with high energy storage. *Nat. Mater.* **2012,** *11* (1), 19.
30. Xia, H.-R.; Sun, W.-T.; Peng, L.-M., Hydrothermal synthesis of organometal halide perovskites for Li-ion batteries. *Chem. Commun.* **2015,** *51* (72), 13787-13790.
31. Zhang, W.; Eperon, G. E.; Snaith, H. J., Metal halide perovskites for energy applications. *Nat. Energy* **2016,** *1*, 16048.

32. Ahmad, S.; George, C.; Beesley, D. J.; Baumberg, J. J.; De Volder, M., Photo-Rechargeable Organo-Halide Perovskite Batteries. *Nano Lett.* **2018,** *18* (3), 1856-1862.
33. Kojima, A.; Teshima, K.; Shirai, Y.; Miyasaka, T., Organometal halide perovskites as visible-light sensitizers for photovoltaic cells. *J. Am. Chem. Soc.* **2009,** *131* (17), 6050-6051.
34. Yang, W. S.; Park, B.-W.; Jung, E. H.; Jeon, N. J.; Kim, Y. C.; Lee, D. U.; Shin, S. S.; Seo, J.; Kim, E. K.; Noh, J. H., Iodide management in formamidinium-lead-halide–based perovskite layers for efficient solar cells. *Science* **2017,** *356* (6345), 1376-1379.
35. Tathavadekar, M.; Krishnamurthy, S.; Banerjee, A.; Nagane, S.; Gawli, Y.; Suryawanshi, A.; Bhat, S.; Puthusseri, D.; Mohite, A. D.; Ogale, S., Low-dimensional hybrid perovskites as high performance anodes for alkali-ion batteries. *J. Mater. Chem. A* **2017,** *5* (35), 18634-18642.
36. Ramirez, D.; Suto, Y.; Rosero-Navarro, N. C.; Miura, A.; Tadanaga, K.; Jaramillo, F., Structural and Electrochemical Evaluation of Three-and Two-Dimensional Organohalide Perovskites and Their Influence on the Reversibility of Lithium Intercalation. *lnorg. Chem.* **2018,** *57* (7), 4181-4188.
37. Peled, E., The electrochemical behavior of alkali and alkaline earth metals in nonaqueous battery systems—the solid electrolyte interphase model. *J. Electrochem. Soc.* **1979,** *126* (12), 2047-2051.
38. Peled, E.; Menkin, S., SEI: past, present and future. *J. Electrochem. Soc.* **2017,** *164* (7), A1703-A1719.
39. Rezvani, S. J.; Gunnella, R.; Witkowska, A.; Mueller, F.; Pasqualini, M.; Nobili, F.; Passerini, S.; Cicco, A. D., Is the Solid Electrolyte Interphase an Extra-Charge Reservoir in Li-Ion Batteries? *ACS Appl. Mater. Interfaces* **2017,** *9* (5), 4570-4576.
40. Aurbach, D., The role of surface films on electrodes in Li-ion batteries. In *Advances in Lithium-Ion Batteries*, Springer: 2002; pp 7-77.

41. Aurbach, D.; Zaban, A.; Ein-Eli, Y.; Weissman, I.; Chusid, O.; Markovsky, B.; Levi, M.; Levi, E.; Schechter, A.; Granot, E., Recent studies on the correlation between surface chemistry, morphology, three-dimensional structures and performance of Li and Li-C intercalation anodes in several important electrolyte systems. *J. Power Sources* **1997,** *68* (1), 91-98.

42. Aurbach, D.; Markovsky, B.; Weissman, I.; Levi, E.; Ein-Eli, Y., On the correlation between surface chemistry and performance of graphite negative electrodes for Li ion batteries. *Electrochim. Acta* **1999,** *45* (1-2), 67-86.

43. Malmgren, S.; Ciosek, K.; Hahlin, M.; Gustafsson, T.; Gorgoi, M.; Rensmo, H.; Edström, K., Comparing anode and cathode electrode/electrolyte interface composition and morphology using soft and hard X-ray photoelectron spectroscopy. *Electrochim. Acta* **2013,** *97*, 23-32.

44. Ding, M. S.; Koch, S. L.; Passerini, S., The Effect of 1-Pentylamine as Solid Electrolyte Interphase Precursor on Lithium Metal Anodes. *Electrochim. Acta* **2017,** *240*, 408-414.

2

Characterization methods and modelling

Firstly, it should be pointed out that in this thesis all the experiments have been carry out with half-cell, i.e., all the electrodes, both anode and cathode materials, have been characterizes against lithium metal.

2.1. Cell assembly

For electrochemical testing, composite electrodes were prepared by hand-mixing active material, carbon black and binder in Agatha mortar, about 80:10:10 by weigh, respectively, and made into slurry by adding 1-Methyl-2-pyrrolidone (NMP). The slurry was spread on contact aluminum or cupper foil (cathode or anode, respectively) by Dr. Blade technique and vacuum dried. Later, electrodes were cut and placed in two-electrodes Swagelok cells with lithium metals as the counter and reference electrode, and separator soaked by electrolyte under inert glovebox, with controlled oxygen and moisture contents. In order to let electrolyte permeate through the separator, cells were allowed to rest few hours.

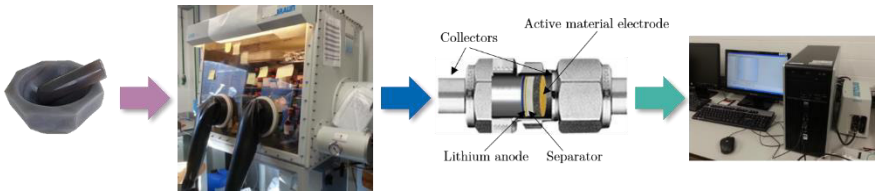

Figure 2. 1. Scheme of assembled lithium half-cell.

2.2. Cyclic Voltammetry, CV

Cyclic voltammetry is a quantitative electrochemical tool to investigate the potentials in which the electron transfer reactions take place for charge/discharge batteries and their reversibility relative to the number of peaks on both the forward and reverse scan.

This reversal technique is based on the sweeping the potential window and recording the current as function of potential. The voltage of the working electrode (electrode that is characterized vs. lithium) is swept between two values: V_1 and V_2 at a fixed rate. When the voltage reaches V_2 the scan is reversed and the voltage is swept back to V_1.[1-2] A typical cyclic voltammogram recorded is shown in **Figure 2. 2.**

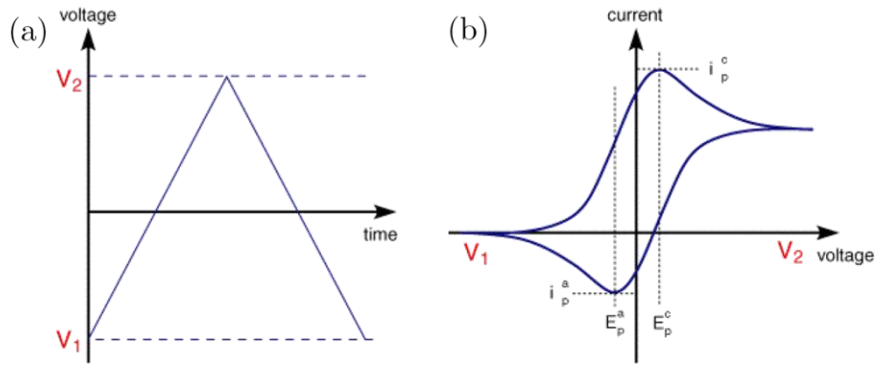

Figure 2. 2. (a) The voltage is swept between two values at a fixed rate. (b) Typical cyclic voltammogram recorded for a reversible single electrode transfer reaction. E_p^a is the potential which oxidation takes place and E_p^c defines the reduction reaction potential.

2.3. Galvanostatic charge/discharge

One of the most straightforward tests to characterize an electrode material is to apply a constant current until a V cut-off value is reached to measure the potential of the electrode as a function of time, to obtain quantitative values and reproducing the behavior of the battery, depending on the insertion or removing Li^+ into the material is said to be charged or discharged the cell.

The information about electrochemical processes that take place during charging and discharging is showed in the way in which the potential changes over time. These results allow to calculate the capacity of the system:[1]

$$\boldsymbol{Q = \int_{t_1}^{t_2} I(t)dt = I \cdot \Delta t} \qquad (2.1.)$$

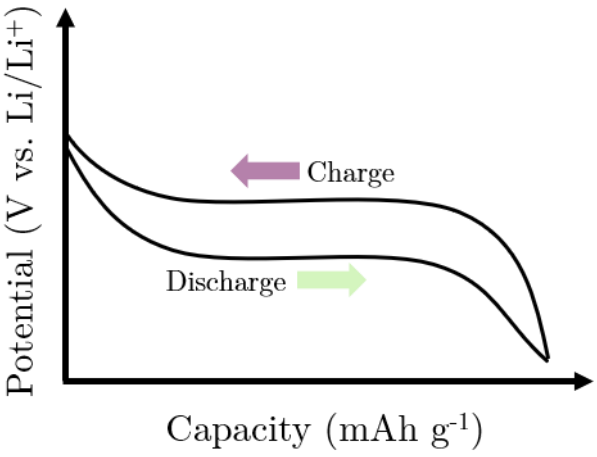

Figure 2. 3. Schematic of potential in the charge/discharge profile of an ideal insertion electrode material. This electrochemical potential is caused by the energy difference of phase transitions between the charge and discharge profiles.

2.4. Electrochemical Impedance Spectroscopy, EIS

Electrochemical impedance spectroscopy is a powerful non-destructive technique whose measurements can be correlated with chemical, physical, mechanical and electrical variables. It allows the study of adsorption, charge and mass transport, and the kinetics mechanism in battery electrodes, that is thanks to the different characteristic times at which each process takes place. This tool measures the flow of an alternating current as a function of frequency, $\hat{I}(\omega)$, at a steady state voltage, V. It used a sinusoidal excitation voltage signal, $\hat{V}(\omega)$, whose amplitude is usually 10-20 mV and applies frequency sweeps (regularly in the range of 1MHz down to 1 mHz). This small perturbation ensures a linear dependence between $\hat{V}(\omega)$ and $\hat{I}(\omega)$ (see Fig. 11).

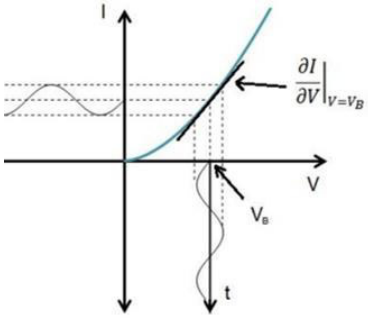

Figure 2. 4. Small amplitude voltage signal perturbation with a liner response.

The impedance is defined as:

$$Z(\omega) = \frac{\hat{V}(\omega)}{\hat{I}(\omega)} \qquad (2.2.)$$

The symbol $\hat{x}$ over a quantity x indicates that is the complex small amplitude of a sinusoidal AC perturbation of x.

In view of the battery electrodes, it induces changes in transport and charging mechanism involving ionic species of different time scales, mainly Li^+ in batteries, as shown in **Figure 2. 5**:

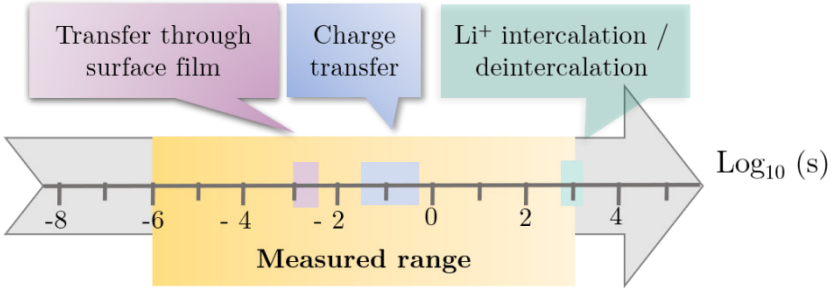

Figure 2. 5. Measurement timescale used in the Li-ion batteries modelling by impedance spectroscopy.

In case of batteries electrodes are submerged in electrolytes containing a lithium reservoir, when impedance test is conducted the processes at the electrode/electrolyte interface and the electrode bulk material are affected by the small perturbation. Thus, it allows to obtain both electrode capacitance data and load transfer kinetics, so it could be determined the reaction mechanisms of a specific electrochemical system and distinguish between different physical and chemical processes that take place at the electrode-electrolyte interface and electrode bulk material simultaneously and/or consecutively, using equivalent circuits including elements that act like resistors, inductors and capacitors. So, a correct interpretation becomes essential to take the best out of this technique.

When battery EIS spectra are analyzed is observed different regions of interest to model a battery system:

- Firstly, the important effect is occurring at the electrode/electrolyte interface. A capacitive and resistive processes take place simultaneously in high frequencies. The

capacitive behavior is in accordance with the classical known double-layer capacitance, C_{dl}, which is defined as the ability of the interface to accumulate ionic species near the surface upon application of voltage, being a function of the dielectric properties of the interface. Thus, the double-layer capacitance is expressed as:

$$C_{dl} = \frac{\varepsilon\varepsilon_0 A}{d} \qquad (2.3.)$$

Where ε is the effective dielectric constant, ε_0 is the vacuum permittivity, A corresponds to active surface and d is the effective charge separation.[1]

At the same time, an interchange of charge carriers, ionic or electronic, between this interface takes place, surpassing an interfacial potential barrier, thereby governed by energetic properties of the interface at a given charging state. As that is a resistive behavior it is accompanied by energy loss. This is known as the permeability to the passage of charge, charge transfer resistance, R_{ct}. This combination of C_{dl} and R_{ct} yields an RC Randles circuit at high frequencies, with the characteristic frequency:

$$\omega_{dl} = \frac{1}{R_{ct}C_{dl}}; \qquad (2.4.)$$

- On the other hand, the electrochemical response of the electrode bulk to the variation in the applied potential is fundamentally represented by a capacitive mechanism labelled as chemical capacitance, C_μ. It is linked to low-frequency limit of the EIS response. It is defined as the ratio

between the variation in electrode charge state produced by a change in the electrode potential V.

$$V = \frac{-(\mu - \mu_{ref})}{e} \qquad (2.5.)$$

Where μ is the chemical potential of Li^+ in the electrode, μ_{ref} correspond to Li metal (in our case because of half batteries with lithium metal as reference is studied) and e the positive elementary charge. In addition, the concentration of Li-ions in the electrode bulk depends on the total concentration N and the molar fraction in a given lithiated state x as $n=Nx$. In a electrode, the ion chemical potential varies as a function of the amount of inserted charge $\mu(x)$, the chemical capacitance (per unit volume) can be then readily expressed as:

$$C_\mu = eN\frac{dx}{dV} \quad (\mathrm{F\ cm^{-3}}) \qquad (2.6.)$$

In F g^{-1}using the density of the active material.
Obviously, chemical capacitance is relative to the integral of the CV when very low current rates are employed.[1] Example is shown below in the **Figure 2. 6**.

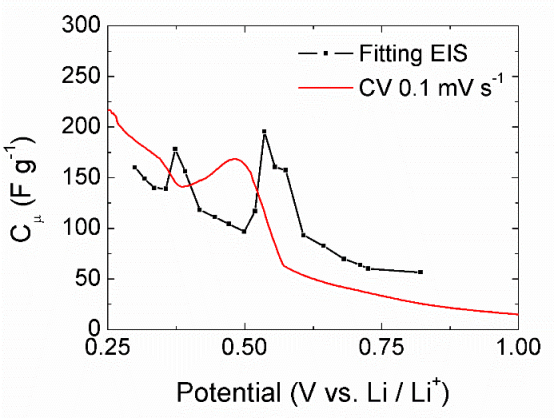

Figure 2. 6. Example how to fit chemical capacitance by EIS measurements and cyclic voltammetry. Values correspond to $CH_3NH_3PbBr_3$ anode. (Reproduced with permission from Vicente, N.; Garcia-Belmonte, G, Organohalide Perovskites are Fast Ionic Conductors, Adv. Energy Mater. 2017, 7 (19), 1700710).

In addition, it must be considered that the different electrochemical systems will have several rate-limiting mechanisms hindering or delaying the charging. Thus, any energy loss is electrically viewed as a resistance. In electrode materials, the basic charging process involves the chemical reaction between Li^+ and the electrode constituents, but it must be distinguished between an intercalation electrode, where the incorporation of ionic species does not excessively distort the lattice and conversion or alloying electrodes Li^+ intake produces a rearrangement of the lattice structure.

- Intercalation electrode reaction implies that the reduction reaction itself is energetically favorable involving reduced energy losses. The transport of Li^+ inside the bulk of the electrode is the resistive mechanism which is called diffusion resistance R_d.
- Conversion or alloying electrode reaction governs the charging process and it is represented by a reaction resistance, R_r, corresponding to the overall energy losses involved in the solid-state reaction.

In both cases, either diffusion-limited or reaction-limited, the elements which represent this stage operate within the low-frequency range.

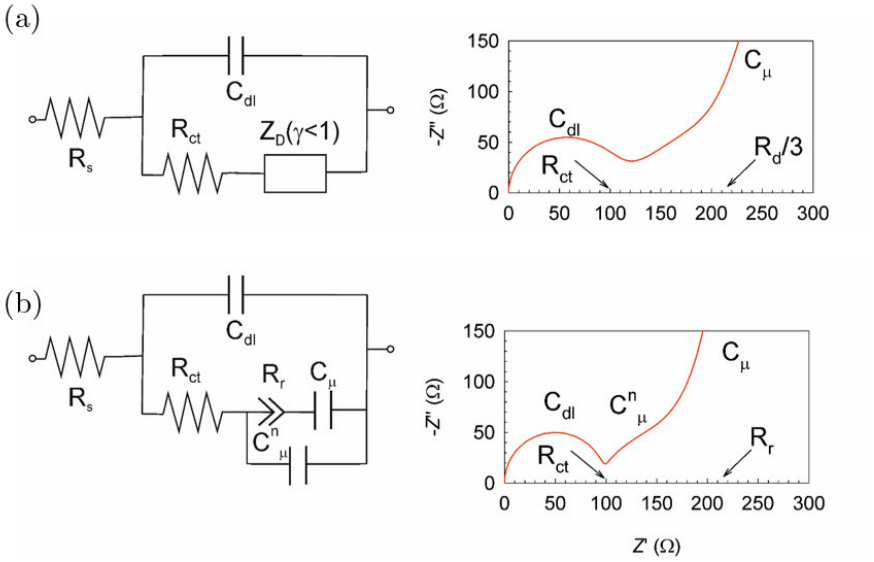

Figure 2. 7. Equivalent circuits and their corresponding impedance plot ($Z''-Z'$ complex plane) for different battery electrode mechanisms. R_s accounts for the solution resistance. (a) Randle's circuit proposed for intercalation electrode with anomalous spatially limited diffusion model Z_D with disorder parameter $\gamma < 1$. (b) A reaction-limited model including the generalization of reaction resistance. In all the plots: $C_{dl} = 1$ μF, $C_\mu = 1$ mF and $R_{ct} = 100\ \Omega$. (b) $n = 0.85$ for both capacitances. (a) $R_d = 300\ \Omega$ and $\gamma = 0.85$. (b) Including $C^n_\mu = 100$ μF.

In addition to the foregoing, the equivalent circuits can be correctly elaborated and capture all the electrochemical mechanism involved in the electrode response with previous theoretical knowledge about capacitive and resistive process occurring in the electrode. Herein, solid kinetic models have been proposed for each of the studied electrodes to explain the electrode behavior, whether intercalation, conversion or alloying electrodes.

2.5. *Operando*-X-Ray Diffraction, *Opernado*-XRD

In contrast to *ex-situ* characterization techniques, an *operando* XRD experiments makes possible to study how the crystalline structure changes in new electrode materials during their lithiation and delithiation to better understand the reaction pathway followed during the cycles. An opportunity to clarify what is the mechanism taking place during charge/discharge process in batteries with $CH_3NH_3PbBr_3$ anode.

This technique has the advantage of avoiding exposure to the atmosphere outside it, namely the diffraction measurement is done in real time as the battery charges and discharges. The design of the electrochemical cell for operando diffraction that was used to carry out the experiments was a Helmholtz Institute Ulm design, it can see in **Figure 2. 8.**

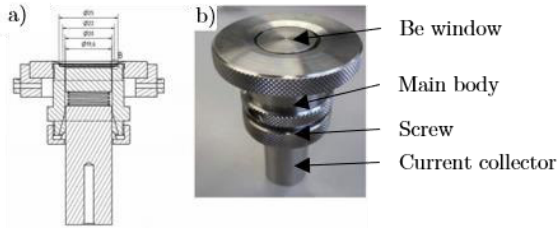

Figure 2. 8. Electrochemical cell for *operando*-XRD experiments: a) detailed view of the cell and b) a cell photo.[2] (Reproduced with permission from Bresser, D.; Paillard, E.; Kloepsch, R.; Krueger, S.; Fiedler, M.; Schmitz, R.; Baither, D.; Winter, M.; Passerini, S., Carbon Coated ZnFe2O4 Nanoparticles for Advanced Lithium-Ion Anodes. Adv. Energy Mater. 2013, 3 (4), 513-523).

In Chapter 7 can read the battery configuration and the procedure used to characterize the anodes. In this case beryllium window is necessary to the X-ray cut into the electrode. So, the configuration is Be window/electrode to study/separator-soaked electrolyte and

lithium metal, which is assembled inside the inert glovebox with oxygen and

moisture under control. During charge/discharge process the phase transitions are recorded in diffraction patterns, with very slow current rates applied. The data obtains clearly are in good agreement with the results obtained from electrochemical data. A detailed analysis is discussed in the corresponding publication presented in this thesis.

2.6. References

1. Bard, A. J.; Faulkner, L. R.; Leddy, J.; Zoski, C. G., *Electrochemical methods: fundamentals and applications*. wiley New York: 1980; Vol. 2.
2. Bisquert, J., *Nanostructured energy devices: equilibrium concepts and kinetics*. CRC Press: 2014.
3. Bresser, D.; Paillard, E.; Kloepsch, R.; Krueger, S.; Fiedler, M.; Schmitz, R.; Baither, D.; Winter, M.; Passerini, S., Carbon Coated ZnFe2O4 Nanoparticles for Advanced Lithium-Ion Anodes. *Adv. Energy Mater.* **2013,** *3* (4), 513-523.

3

Publication 1

3.1. Candidate's contribution

In this case of Publication 1, the nature and extent of my contribution to the work was the following:

Nature of contribution	Extent of contribution
• Review of existint literature and assessment on the present understanding of $LiFePO_4$ electrodes • Design experiments • Analysis and discussion the experimental data • Performance the impedance study, and development and discussions of the impedance model. • Help in the preparation of manuscrit drafts.	35 %

3.2. Published manuscript

N. Vicente, M. Haro, D. Cíntora-Juárez, C. Pérez-Vicente, J. L.Tirado, S. Ahmad, G. Garcia-Belmonte. $LiFePO_4$ particle conductive composite strategies for improving cathode rate capability, *Electrochimica Acta*, **2015**, 163, 323-329.

$LiFePO_4$ particle coating strategies for improving cathode rate capability

Nuria Vicente[a], Marta Haro[a], Daniel Cíntora-Juárez[b], Carlos Pérez-Vicente[b], José Luis Tirado[b], Shahzada Ahmad [c,*], and Germà Garcia-Belmonte [a,*]

[a] *Photovoltaics and Optoelectronic Devices Group, Departament de Física, Universitat Jaume I, 12071 Castelló, Spain*

[b] *Laboratorio de Química Inorgánica, Campus de Rabanales, Universidad de Córdoba, 14071, Spain*

[c] *Abengoa Research, C/ Energía Solar nº 1, Campus Palmas Altas, 41014 Seville, Spain*

Email: garciag@uji.es

Abstract

Lithium iron phosphate (LFP) cathodes are one of the most promising candidates to find application in hybrid electric vehicle energy storage system. For this reason, advances in the performance of its theoretical capacity at high charge/discharge rates is under continuous development. Most used strategies to improve power performance are carbon coating and the addition of a conductive polymer, such as poly (3,4-ethylenedioxythiophene) [PEDOT]. The data obtained from impedance analysis show that these strategies not only improve the charge transfer but also favor the lithiation/delithiation processes in the phosphate matrix. Furthermore, PEDOT is capable to reduce the resistances of charge transfer and lithiation reaction inside the phosphate matrix by one order of magnitude in comparison with those achieved with the carbon coating

strategy. In this study, the most effective strategy has been the addition of PEDOT by a blending method, resulting in a specific capacity of 130 mA h g_{LFP}^{-1} at 2C.

1. Introduction

In the last decades, lithium iron phosphate ($LiFePO_4$) has been extensively studied, and currently it is regarded as one of the most likely candidate for the large-sized Li-ion batteries for hybrid electric vehicles (HEV) [1]. Other applications include, cathode in portable electronic devices, bulk electricity storage at power stations, and to provide back-up energy for solar and wind power [2,3]. This electrode has attracted extensive attention due to a high theoretical specific capacity (170 mAh g^{-1}), high stability, low cost, high compatibility with environment, and small amount of oxygen generation at the fully charged state. Its main drawback is to attain the full capacity due to its low electronic conductivity which leads to initial capacity loss and poor rate capability, because of slow reaction of Li^+ ion in $LiFePO_4/FePO_4$.

To gain the full capacity of these materials, the mechanism of charging-discharging of this cathode has been deeply studied [4,5]. In the $LiFePO_4$ olivine structure, the oxygen atoms adopt a hexagonal closed-packing configuration with Li^+ and Fe^{2+} cations located in half of the octahedral sites and P^{5+} cations in 1/8 of tetrahedral sites. Then, there exist 1D channels for Li^+ ions exchange. Once the mechanism is understood, several strategies have been investigated to improve both electronic and ionic conductivity to overcome the current bottleneck in these materials. Two of these strategies are coating with carbon and/or conducting polymers. Carbon improves the electronic conductivity and can contribute to increase the electrode capacity [6-10]. However, perfect surface coatings and desired mixtures are often very difficult to achieve and the power- performance enhancement of these

electrode materials is still limited. More recently, the use of conductive polymers such as poly(3,4-ethylenedioxythiophene) (PEDOT) is especially attractive in terms of the improvement of the mechanical flexibility, the option to be coated under mild processing conditions compared to carbon coating, improvement of Li-ion transport, and for its dual role as conductive and binder additive [11-13]. In these cathodes, the synthesis procedure is key for the final stoichiometry and microsctructure that largely influence the physico-chemical properties of the material.

LFP can be directly prepared by ceramic procedures. Normally, solid precursor compounds such as Fe(II)-acetate, ammonium phosphate, and lithium carbonate are mixed together in a ball mill, and a first mild temperature treatment is used to achieve their decomposition [14]. The final thermal treatment up to 900ºC is carried out in an inert or slightly reducing atmosphere to avoid Fe^{2+} to Fe^{3+} oxidation. The addition of carbon sources such as citric acid is also used for this purpose. With sufficient carbon excess, e.g. by covering the pellets with carbon black, the resulting LFP particles are carbon- coated and display improved conductive properties [15]. Due care must be taken to avoid an extended formation of iron phosphide that may penalize the capacity, although being also a conductive side product [16]. To lower the reaction temperature, LFP can also be synthesized by solvothermal methods. The hydrothermal procedure starting from $FeSO_4 \cdot 7H_2O$ and o-H_3PO_4 premixed with water by addition of a LiOH solution [17] can be carried out in both subcritic and supercritic conditions, the later favoring a higher dispersion of the resulting powders. Ionothermal [18], polyol [19], non-aqueous sol-gel syntheses [20] and coprecipitation in aqueous medium [21], have also been successfully employed.

Recently, we have proposed a model to study the lithiation/delithiation kinetics through equivalent circuit analysis of the experimentally obtained electrochemical impedance spectroscopy (EIS) spectra [22,23]. This approach facilitates the

extraction of resistances involved in the overall lithium ion storage that allows establishing mechanisms for rate capability reduction, as well as the insertion-extraction process occurring during the battery cycling. Herein, $LiFePO_4$ (LFP) electrodes were coated with PEDOT to give molecular wiring effect (LFP/PEDOT), carbon (C-LFP), and both materials (C-LFP/PEDOT). The role of each element has been analyzed by impedance spectroscopy that can distinguish the different steps involved in the charge-discharge process associated to the specific electrochemical mechanisms and, by means of a proposed equivalent circuit model, the different processes can be related to resistances and capacitances. The obtained data show that PEDOT reduces the resistances of charge transfer and lithiation reaction one order of magnitude respect to those extracted employing carbon coatings, which gives a new resistance and capacity ascribed to the carbon film. Albeit the lithiation/delithiation mechanism has been extensively studied in olivine cathodes, novel insight into the electrical contributions of each element is obtained through the resistive analysis of the recorded impedance spectra.

2. Experimental

LFP was obtained as described elsewhere [24]. For C-coating, samples were pressed into pellets that were then covered with excess carbon black ca. 1 g/400 mg of sample and then heated in alumina boats at 750, 850, and 900°C for 8 and 16 h. Then, the remaining carbon black excess was mechanically removed. Electrodes were also prepared by mixing the LFP or LFP/C active materials with CB and PVDF (85:8:7 wt.) in *N*-methyl pyrrolidone. The mixture was sonicated and deposited over aluminum disks (0.64 cm^2). Finally, the deposits where dried at 80° C under vacuum for 12 h. The average amount of LFP in the electrodes is estimated at 5 mg cm^{-2}. Samples with PEDOT:PSS

where obtained by two methods. The first method (blend) consisted in mixing PEDOT:PSS (0.3 mg) with LFP, PVDF and CB. For the second method (dropcast), PEDOT:PSS (0.3 mg) was casted over a preformed LFP or C-LFP electrode. For both methods, the electrodes were dried under vacuum at 100º C for 12 h.

Scanning electron microscopy (SEM) images were obtained using a JEOL JSM63000 microscope. The electrochemical characterization was carried out using a two-electrode Swagelok cell with metallic lithium as both the counter and the reference electrode, and a glass fiber (Grade GF/C260µm-thick) from Whatman as a separator. The electrolyte used was 1.0 M $LiPF_6$ in a 50:50 (w/w) mixture of ethylene carbonate (EC) and diethyl carbonate (DEC). Cell assembly was carried out in an N_2-filled glovebox. Electrochemical characterization was performed using a PGSTAT-30 potentiostat from Autolab equipped with an impedance module. 1C was defined as 170 mA g^{-1} for the charge-discharge tests. The cyclic voltammetry (CV) and the galvanostatic charge/discharge tests were carried out in the voltage window of 2-4.5 V. The EIS were performed at several voltages within this voltage range with amplitude of 10 mV and in the frequency range of 1 MHz to 1mHz.

The experimental data are normalized to the mass of LFP, although the masses of PEDOT and C are the same in the electrodes, and the relationship of the values maintain the same if it was referred to the mass of the electrode.

3. Results and discussion

3.1. Characterization of LFP based electrodes

Figure 1a shows particles of pristine LFP, while Figure 1b

shows the LFP coated with PEDOT:PSS. It can be observed that the virgin LFP is of irregular shape while the modified LFP cathode with PEDOT:PSS has uniformly covered the surface resembling a blanked coating atop of LFP. The granular structures of LFP are in close contact with PEDOT resulting in a material with enhanced mechanical and electrical comunication between the active particles.

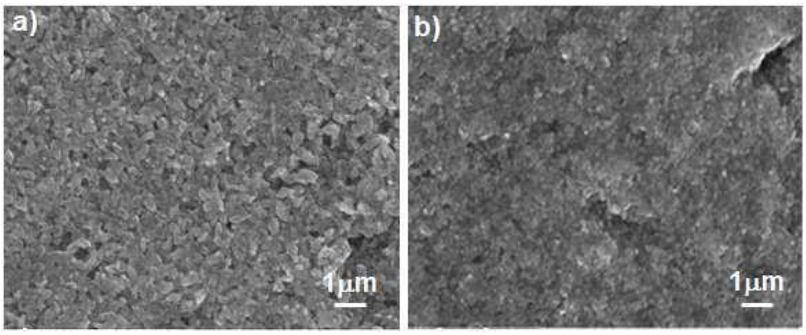

Fig. 1. Scanning electron microscopy images of a) pristine LFP and b) LFP/PEDOT- materials.

3.2. Electrochemical response

Figure 2 shows the 3rd cycle of the cyclic voltammetry signal of the LFP-based cathodes, where the Fe^{3+}/Fe^{2+} redox reaction peaks upon lithium intercalation are observed within the range of 2-4.5 V. The faradaic processes related to the Li^+ ion insertion and extraction from the LFP lattice are clearly favored in the cathode LFP/PEDOT(blend), which shows the closest and narrowest peaks, followed by LFP/PEDOT(cast) electrode that shows similar behavior to C-LFP/PEDOT(cast) cathode. The C-LFP electrodes (without PEDOT) show the Li^+ ion insertion and extraction processes with a separation of almost 2 V. The width of the peaks and the separation between them are related to the kinetic limitations (resistances) present in the electrode. Besides

residual hysteresis unveiled in multiparticulate LFP electrodes at extremely low currents was ascribed to thermodynamic phenomena in a recent study [25]. According to the CV experiments, PEDOT reduces the resistances in the system, in particular for the blend preparation, while the effect of C-coating is considerably less significant.

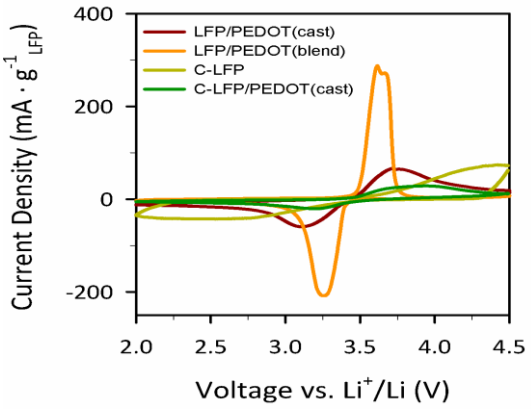

Fig. 2. Cyclic voltammograms of the $LiFePO_4$ and C-$LiFePO_4$ modified electrodes at 0.1 $mV \cdot s^{-1}$.

The third cycle of the charge-discharge curves obtained at different rates for the LFP/PEDOT, C-LFP/PEDOT, and C-LFP electrodes are shown in Figure 3a-d. In all cases, as the current density increases, the charge-discharge plot shows that the specific capacity decreases, which indicates low active material utilization and transport limitations in the solid $LiFePO_4$ particles [25]. This effect is clearly observed in Figure 3e that shows the effect of the cycle number and the charging-discharging rate on the capacity of the cathode. At very low current, C/10, the discharge specific capacity is similar for all the studied electrodes, with slightly larger values for C-LFP-PEDOT(cast) and lower for LFP-PEDOT(cast). As the discharge current increases the battery with higher specific capacity is LFP-PEDOT(blend) that provides 130

mAh g^{-1} at 2C. Meanwhile, when the polymer is drop cast over LFP and C-LFP, the specific capacity collapses at C and 2C rates, respectively. After such tests, these electrodes show no response even at low charge current (C/10). This phenomenon suggests that the lost of capacity is related to stability issues rather than kinetic barriers. This elucidation was also supported by the CV experiments, in which both electrodes show better defined redox peaks than the C-LFP sample, which suggests lower resistance values. The kinetic limitations are clearly observed for C-LFP that shows similar specific capacity than LFP-PEDOT-blend at low discharge current (C/10, C/5), however it decreases notably above C/2, reaching a value of 50 mAh g^{-1} at 2C (less than half the value obtained for LFP-PEDOT(blend)).

The other feature observed in Figure 3a-d is reflected in Figure 3f. As the current density increases the mid plateau potential decreases (increases), and the voltage gap resulting from the hysteresis increases. This effect has been assigned to a combination of transport and ohmic losses with negligible contribution from the kinetics of the charge-transfer reaction [25]. The lowest hysteresis is for the sample LFP/PEDOT(blend) that scarcely increases with the charge-discharge rate. The small value of the gap at moderate 1C rate, suggests that blended PEDOT favors the transport of both Li^+ ions and e^- within the LFP bulk. It is evident that the electrode preparation method is critical for the battery operation. Thus, when the PEDOT is cast in the cathode, the transport and ohmic losses increases dramatically. On the other hand, the C coverage reduces these losses to some extent.

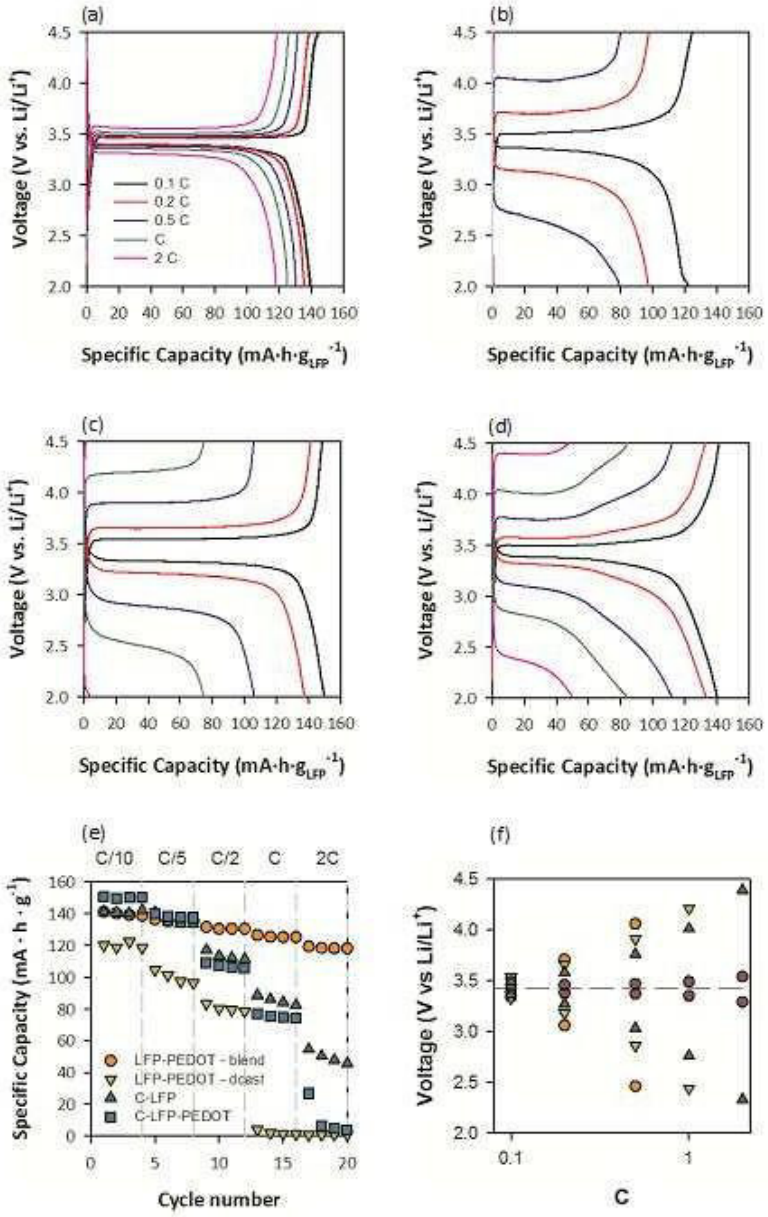

Fig. 3. Charge-Discharge curves (third cycle) at different rates for: a) LFP/PEDOT(blend), b) LFP/PEDOT(cast), c) C-LFP/PEDOT(cast), and d) C-LFP. e) Effect of cycle number and charge rate over the charge capacity for the four studied cathodes. f) Voltage of the charge/discharge plateau vs. C.

In summary, coating with a conductive polymer such as PEDOT reduces the transport limitations in the solid $LiFePO_4$ particles and increases the rate performance of the cathode. The carbon coating improves thermodynamic properties, while the kinetic behavior is more restricted in comparison with PEDOT coatings. Further to distinguish the effect of PEDOT and C in the cathodes, the impedance spectra of these batteries are discussed in the next section by means of EIS technique. The samples prepared with PEDOT (cast) show worse electrical response than those using blend method and have lower stability, thus the impedance spectra is discussed in the Supplementary Information (SI). It is noteworthy that synthesis method is crucial in the cathode operation and the following discussion is valid for the particular PEDOT and C deposition in LFP cathodes described in this manuscript.

3.3. Electrochemical impedance spectroscopy analysis

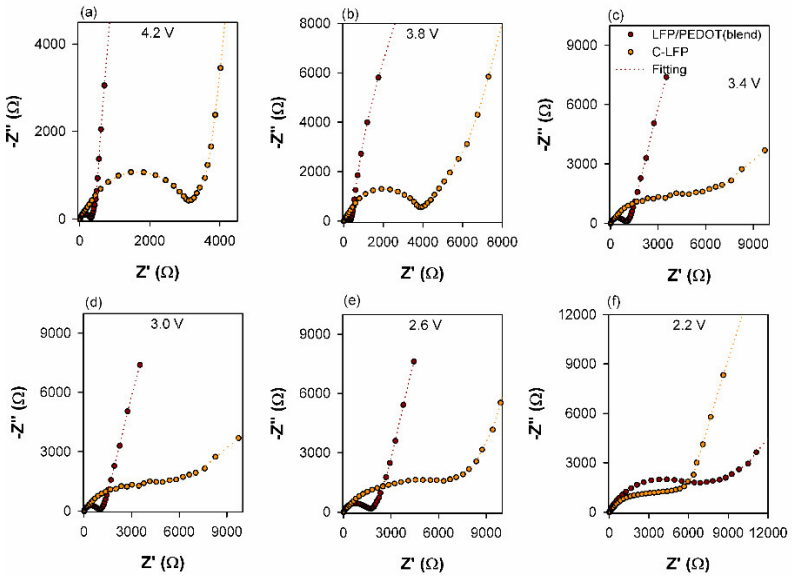

Fig.4. Nyquist plots of experimentally measured data (circles) and fitting results for the equivalent circuit model (Figure 5a) at different stages of discharge for: LFP/PEDOT(blend), and C-LFP.

Aiming at uncovering the origin for the superior rate capability exhibited by LFP/PEDOT(blend) cathodes, the assembled half batteries were characterized by means of EIS to discern the different steps involved in the charge-discharge process. After three CV cycles, the EIS measurements were carried out potentiostatically at different stages of the Li^+ ion insertion and extraction at a very low rate to ensure the steady-state condition. Figure 4 shows, as example, different Nyquist diagrams experimentally obtained during the lithiation process. The Nyquist plots for the delithiation process are represented in the SI, where the discussion is similar to that reported in the text for the lithiation process.

In general terms, the impedance spectra exhibit two patterns with distinguishable time constants associated to specific electrochemical mechanisms and an additional series resistance that accounts for the solution contribution, $R_s \approx 9\ \Omega$. First, at high frequencies a flattened arc is observed related to the interfacial charge transfer resistance, R_{ct}, in parallel with the double layer capacitance, C_{dl}. A detail of this arc shows in the case of C-LFP an additional small arc (effect clearly observed in the representation of capacitances that is shown and discussed in SI) related to the resistance and capacitance of the C-coating, R_C and C_C. Second, at low frequencies, the Nyquist plots show a capacitive behavior associated with the Li^+ ion storage inside the cathode which is manifested by its chemical capacitance, C_μ. [26] This capacitance refers to the differential change in electrode charge upon voltage variation and it is connected to the ability of the phosphate matrix to react with Li^+ ions. In fact it is a quasi-equilibrium (extremely slow-rate) version of the CV experiment that corresponds to the derivative of the charge-discharge curve as $C_\mu = -dQ/dV$. An additional capacitive element C_{Li^+} accounts for the contribution of inserted Li^+ before reaching stable sites within the Li matrix, i.e. before lithiation reaction is accomplished to form Li_xFePO_4. This capacitance appears at the intermediate-frequency arc of the impedance plots. [22,23]

These considerations suggest a simple equivalent circuit (Figure 5a) which accounts for the high-frequency response by means of R_{ct} and C_{dl} for both cathodes, and for C- LPF also by R_C and C_C. The low-frequency part is modeled by a series combination of resistive R_{lr} (lithiation reaction) and capacitive (chemical) C_μ elements in parallel to C_{Li^+}. It is noted here that the equivalent circuit in Figure 5a models the hindrance in the Li^+ final reaction with the host matrix by means of the resistive element R_{lr}. This is a phenomenological representation of a series of kinetic limitation mechanisms that comprises not only ion transport but also

reaction losses. In comparison with previously proposed equivalent circuits [27], our model connects the low-frequency subcircuit in series with the interfacial charge transfer resistance R_{ct} while putting C_{dl} in parallel. This circuit element connection agrees with the original Randles model accounting for the electrochemical impedance of surfaces.

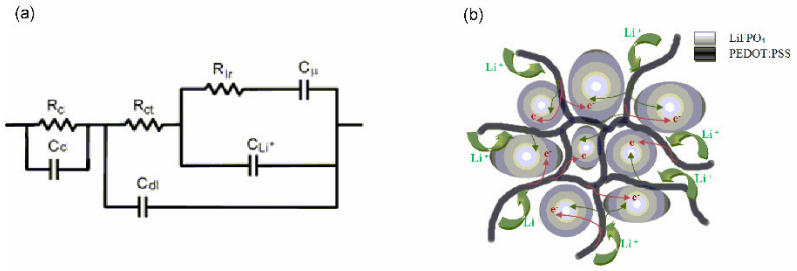

Fig. 5. a) Equivalent circuit used for fitting: *i*) resistance and capacity ascribed to the C- coating layer, R_c and C_c, for the cathode C-LFP; *ii*) the interfacial charge-transfer resistance, R_{ct}, combined with the double-layer capacitance, C_{dl}, that dominates the high-frequency response; and *iii*) reaction subcircuit modeled by chemical capacitance C_μ, Li^+ capacitance C_{Li^+}, and lithiation-reaction resistance, R_{lr}. b) Scheme of the PEDOT conducting molecular network during lithiation process in LFP/PEDOT(blend) cathode.

Main parameters extracted from fitting using the equivalent circuit in Figure 5a are summarized in Figure 6. With the calculated values it is easier to understand the lithiation process monitored by impedance spectra (Figure 4). It is observed that both C- LFP and LFP/PEDOT(blend) electrodes exhibit similar chemical capacitance values (Figure 6a) that peak at voltages near 3.5 V as the phosphate matrix reacts with Li^+ ions. This agrees with the potential plateau of charging/discharging profiles reported in Figure 3a and 3d. The observation of similar capacitances informs that the charging ability at sufficiently slow rate (quasi-equilibrium) is comparable and independent on the coating strategy. However, differences in kinetic limitation are evident by examining Figure 6b. It was found that C-LFP

electrodes exhibit higher resistances than LFP/PEDOT(blend) electrodes. In both cases the higher resistance at potentials in excess of 3.9 V is the charge transfer that is one order of magnitude higher for C-LFP than for LFP/PEDOT(blend). In the case of the C-LFP, R_{lr} increases one order of magnitude and becomes the dominant resistance of the cathode. This high resistive value slows down the phosphate lithiation. R_{lr} decreases with further discharge but it maintains high values, ca. 35 Ω g. This explains the width cathodic peak observed in the CV (Fig. 2) for C-LFP cathode. In the case of LFP/PEDOT(blend), the behavior is different. In this case, R_{lr} at 3.4 V is 3.4 Ω g, at the C_μ maximum. The low value of R_{lr} allows a fast lithiation process that is reflected in a well defined cathodic peak in CV (Fig. 2). As commented previously, the performance at quasi-equilibrium state of the impedance spectra shows that both cathodes have practically the same C_μ in all the voltage range, independently of the higher resistances present in the C-LFP cathode, and C_{dl} is higher in this cathode than the registered for LFP/PEDOT(blend). The same discussion can be applied to the charge process, which is performed in SI. Finally, R_c observed for the C-coated LFP particles is constant within the potential range with a value of 0.5 Ω g, that is lower than the other two resistances registered in the system.

These results demonstrate that C-coating and PEDOT(blend) not only facilitate the charge transfer but also affect on the resistance of the lithiation of the phosphate matrix. In this aspect, PEDOT(blend) is a more effective strategy, and the resistances in the electrode are below 10 Ω g until high level of lithiation of the cathode. This is caused by the high conductivity of both electrons and ions of the PEDOT polymer [28] and the good embedded structure of the LFP nanoparticles in the PEDOT matrix (Figure 1.b), which is represented in Figure 5.b.

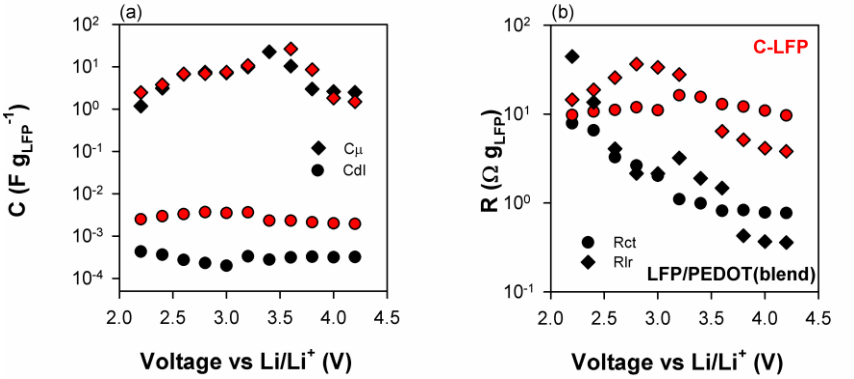

Fig. 6. Parameters fitting in discharge process for LFP/PEDOT(blend) (black symbols) and C-LFP (red symbols): the high frequency response, i.e. transference resistance (R_{ct}) and the double layer capacity (C_{dl}) are symbolized by circles (●), and the low frequency response, i.e. the resistance to the lithiation reaction (R_{lr}) and the chemical capacity (C_{μ}) to rhombus (◆).

4. Conclusions

The electrochemical effect of coating LFP particles by carbon or PEDOT, two of the widely used strategies to increase the conductivity of the $LiFePO_4/FePO_4$ matrix, has been evaluated in terms of resistances and capacities of the different steps in the lithiation/delithiation process present in the cathode. For this purpose, impedance spectra have been registered within the potential range of interest. The Nyquist plots exhibit two patterns with distinguishable time constants associated to specific electrochemical mechanisms. This effect allows to propose an equivalent model in which the high frequency processes are ascribed to surface processes (charge transfer resistance, R_{ct}, and double layer capacity, C_{dl}), and the low frequency response to the lithiation/delithiation inside the phosphate matrix (resistance to the lithiation, R_{lr}, and chemical capacity, C_{μ}). These results show that both strategies reduce the resistances R_{ct} and R_{lr}, albeit

PEDOT is more effective and it is able to reduce the resistances by one order of magnitude compared with C-coating. Suggesting the superior behavior from PEDOT, which favor the kinetics of the lithiation/delithiation processes in the cathode in large extent. In contrast, both strategies deliver similar thermodynamic properties and show similar chemical capacitances. These results explain that the specific capacity of both cathodes (LFP/PEDOT(blend) and C-LFP) are the same at low charge/discharge current (C/10 and C/5) and close to the theoretical value. When the charge/discharge current increases the LFP/PEDOT(blend) maintains almost complete the specific capacity (130 mAh g^{-1} at 2C) while for C-LFP the specific capacity decreases notably because of severe resistive limitations.

Acknowledgment

We thank financial support from Generalitat Valenciana (ISIC/ 2012/008 Institute of Nanotechnologies for Clean Energies).

References

1. G.R. Dahlin, K.E. Strøm, Lithium Batteries: Research, Technology, and Applications, Nova Science Publishers, 2010.
2. B. Kang, G. Ceder, Battery materials for ultrafast charging and discharging, Nature 458 (2009) 190–193.
3. B. Dunn, H. Kamath, J.-M. Tarascon, Electrical energy storage for the grid: a battery of choices, Science 334 (2011) 928–935.
4. C. Delmas, M. Maccario, L. Croguennec, F. Le Cras, F. Weill, Lithium deintercalation in $LiFePO_4$ nanoparticles via a domino-cascade model, Nature materials 7 (2008) 665–671.

5. W. Dreyer, J. Jamnik, C. Guhlke, R. Huth, J. Moškon, M. Gaberšcek, The thermodynamic origin of hysteresis in insertion batteries, Nature Materials 9 (2010) 448–453.
6. D. Xu, X. Chu, Y.-B. He, Z. Ding, B. Li, W. Han, H. Du, F. Kang, Enhanced performance of interconnected LiFePO4/C microspheres with excellent multiple conductive network and subtle mesoporous structure, Electrochimica Acta 152 (2015) 398–407.
7. Y. Wang, Y. Wang, E. Hosono, K. Wang, H. Zhou, The design of a LiFePO4/carbon nanocomposite with a core–shell structure and its synthesis by an in situ polymerizationrestrictionmethod, AngewandteChemie 120 (2008) 7571–7575.
8. X.L. Wu, L.Y. Jiang, F.F. Cao, Y.G. Guo, L.J. Wan, LiFePO4 Nanoparticles Embedded in a Nanoporous Carbon Matrix: Superior Cathode Material for Electrochemical Energy-Storage Devices, Advanced Materials 21 (2009) 2710–2714.
9. S.W. Oh, S.T. Myung, S.M. Oh, K.H. Oh, K. Amine, B. Scrosati, Y.K. Sun, Double carbon coating of LiFePO4 as high rate electrode for rechargeable lithium batteries, Advanced Materials 22 (2010) 4842–4845.
10. Y. Xing, Y.-B. He, B. Li, X. Chu, H. Chen, J. Ma, H. Du, F. Kang, LiFePO4/C composite with 3D carbon conductive network for rechargeable lithium ion batteries, Electrochimica Acta 109 (2013) 512–518.
11. H.C. Dinh, S.I. Mho, I.H. Yeo, Electrochemical Analysis of Conductive PolymerCoated LiFePO4 Nanocrystalline Cathodes with Controlled Morphology, Electroanalysis 23 (2011) 2079–2086.
12. N. Trinh, M. Saulnier, D. Lepage, S. Schougaard, Conductive polymer film supporting LiFePO4 as composite cathode for lithium ion batteries, Journal of Power Sources 221 (2013)

284–289.

13. D. Cíntora-Juárez, C.P. Vicente, S. Ahmad, J.L. Tirado, Improving the cycling performance of LiFePO4 cathode material by poly (3,4-ethylenedioxythiopene) coating, RSC Advances (2014).
14. V. Cauda, D. Pugliese, N. Garino, A. Sacco, S. Bianco, F. Bella, A. Lamberti, C. Gerbaldi, Multi-functional energy conversion and storage electrodes using flower-like Zinc oxide nanostructures, Energy 65 (2014) 639–646.
15. L. Groenendaal, F. Jonas, D. Freitag, H. Pielartzik, J.R. Reynolds, Poly(3,4-ethylenedioxythiophene) and its derivatives: past, present, and future, Advanced Materials (2000) 481–494.
16. A.K. Padhi, K. Nanjundaswamy, J.B.D. Goodenough, Phospho-olivines as positive-electrode materials for rechargeable lithium batteries, Journal of the Electrochemical Society 144 (1997) 1188–1194.
17. M. Armand, M. Gauthier, J.F. Magnan, N. Ravet, New process for synthesizing limpo4 materials with olivine structure, Google Patents, 2002.
18. C.W. Kim, J.S. Park, K.S. Lee, Effect of Fe2P on the electron conductivity and electrochemical performance of LiFePO4 synthesized by mechanical alloying using Fe3+ raw material, Journal of Power Sources 163 (2006) 144–150.
19. J.Y. Kim, S.H. Kim, H.H. Lee, K. Lee, W. Ma, X. Gong, A.J. Heeger, New Architecture for High-Efficiency Polymer Photovoltaic Cells Using SolutionBased Titanium Oxide as an Optical Spacer, Advanced Materials (Weinheim, Germany) 18 (2006) 572–576.
20. N. Recham, L. Dupont, M. Courty, K. Djellab, D. Larcher, M. Armand, J.-M. Tarascon, Ionothermal synthesis of tailor-made LiFePO4 powders for Li-ion battery applications, Chemistry of Materials 21 (2009) 1096–1107.

21. K.-F. Hsu, S.-Y. Tsay, B.-J. Hwang, Synthesis and characterization of nano-sized LiFePO4 cathode materials prepared by a citric acid-based sol–gel route, Journal of Materials Chemistry 14 (2004) 2690–2695.
22. G. Arnold, J. Garche, R. Hemmer, S. Ströbele, C. Vogler, M. Wohlfahrt-Mehrens, Fine-particle lithium iron phosphate LiFePO4 synthesized by a new low-cost aqueous precipitation technique, Journal of Power Sources 119 (2003) 247–251.
23. F. Martinez-Julian, A. Guerrero, M. Haro, J. Bisquert, D. Bresser, E. Paillard, S. Passerini, G. Garcia-Belmonte, Probing Lithiation Kinetics of Carbon-Coated ZnFe2O4 Nanoparticle Battery Anodes, The Journal of Physical Chemistry C 118 (2014) 6069–6076.
24. M. Haro, T. Song, A. Guerrero, L. Bertoluzzi, J. Bisquert, U. Paik, G. GarciaBelmonte, Germanium coating boosts lithium uptake in Si nanotube battery anodes, Physical Chemistry Chemical Physics 16 (2014) 17930–17935.
25. B. León, C.P. Vicente, J. Tirado, P. Biensan, C. Tessier, Optimized chemical stability and electrochemical performance of LiFePO4 composite materials obtained by ZnO coating, Journal of the Electrochemical Society 155 (2008) A211–A216.
26. V. Srinivasan, J. Newman, Existence of path-dependence in the LiFePO4 electrode, Electrochemical and solid-state letters 9 (2006) A110–A114.
27. J. Bisquert, Chemical capacitance of nanostructured semiconductors: its origin and significance for nanocomposite solar cells, Physical Chemistry Chemical Physics 5 (2003) 5360–5364.
28. N. Meethong, Y.-H. Kao, W.C. Carter, Y.-M. Chiang, Comparative Study of Lithium Transport Kinetics in Olivine Cathodes for Li-ion Batteries, Chemistry of Materials (2010) 1088–1097.
29. Y. Zhu, C. Wang, Galvanostatic Intermittent Titration

Technique for PhaseTransformation Electrodes, J. Phys. Chem. C 114 (2010) 2830–2841.

30. K. Weichert, W. Sigle, P.A. van Aken, J. Jamnik, C. Zhu, R. Amin, T. Acartürk, U. Starke, J. Maier, Phase Boundary Propagation in Large LiFePO4 Single Crystals on Delithiation, J. Am. Chem. Soc. 134 (2012) 2988–2992.
31. G. Oyama, Y. Yamada, R.I. Natsui, S.I. Nishimura, A. Yamada, Kinetics of Nucleation and Growth in Two-Phase Electrochemical Reaction of LixFePO4, J. Phys. Chem. C 116 (2012) 7306–7311.
32. J. Song, M.Z. Bazant, Effects of Nanoparticle Geometry and Size Distribution on Diffusion Impedance of Battery Electrodes, Journal of The Electrochemical Society 160 (2013) A15–A24.
33. J.P. Schmidt, T. Chrobak, M. Ender, J. Illig, D. Klotz, E. Ivers-Tiffée, Studies on LiFePO4 as cathode material using impedance spectroscopy, Journal of Power Sources 196 (2011) 5342–5348.
34. G. Li, P.G. Pickup, Ion transport in poly (3,4-ethylenedioxythiophene)–poly (styrene-4-sulfonate) composites, Physical Chemistry Chemical Physics 2 (2000) 1255–1260

Supporting Information

$LiFePO_4$ particle conductive composite strategies for improving cathode rate capability

Nuria Vicente[a], Marta Haro[a], Daniel Cíntora-Juárez[b], Carlos Pérez-Vicente[b], José Luis Tirado[b], Shahzada Ahmad[c]*, and Germà Garcia-Belmonte[a,]*

[a]*Photovoltaics and Optoelectronic Devices Group, Departament de Física, Universitat Jaume I, 12071 Castelló, Spain*
[b]*Laboratorio de Química Inorgánica, Campus de Rabanales, Universidad de Córdoba, 14071, Spain*
[c]*Abengoa Research, C/ Energía Solar nº 1, Campus Palmas Altas, 41014 Seville, Spain*

Email: garciag@uji.es

Impedance response of LFP-PEDOT-blend and C-LFP cathodes during charge process

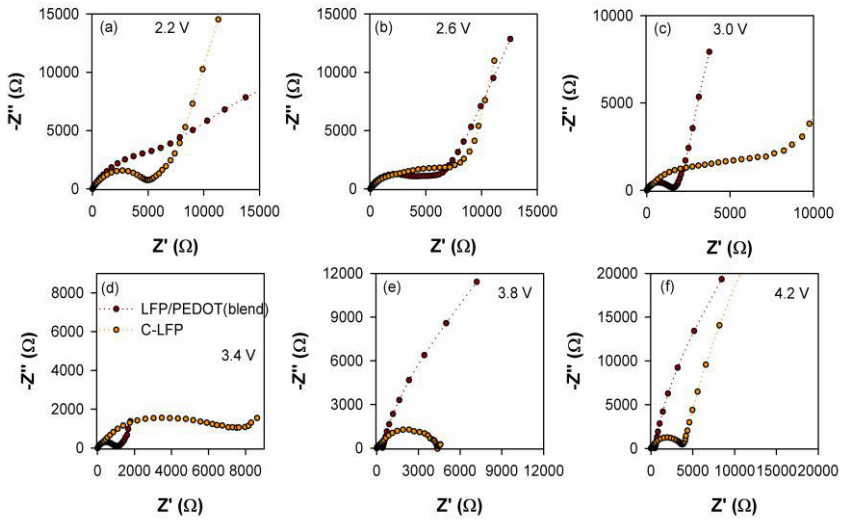

Fig.S1. Nyquist diagrams experimentally measured at different stages of charge for: LFP/PEDOT(blend), and C-LFP.

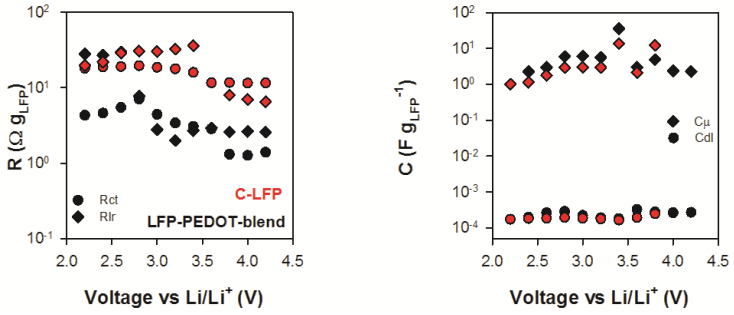

Fig. S2. Parameters fitting in charge process for LFP/PEDOT(blend) (black symbols) and C-LFP (red symbols): the high frequency response, i.e. transference resistance (R_{ct}) and the double layer capacity (C_{dl}) are symbolized by circles (●), and the low frequency response, i.e. the resistance to the lithiation reaction (R_{lr}) and the chemical capacity (C_{μ}) to rhombus (◆).

Nyquist diagrams and the main parameters extracted from the fitting of the equivalent circuit (Fig. 5a) of the LFP/PEDOT(blend) and C-LFP cathodes during the delithiation process are summarized in Fig. S1 and S2. The behavior is similar to the described for the discharge process. At low voltages, the R_{lr} for both cathodes is high and quite similar for both materials. With the increment of voltage, R_{lr} decreases ca. 1 order of magnitude when the cathode contains PEDOT while increases in the case of C-coating, obtaining a maximum at 3.6 V, where the onset of the Fe^{3+}/Fe^{2+} redox reaction upon lithium extraction peak is observed in the *CV* plot (Fig. 2). At this voltage is observed the peak for LFP/PEDOT(blend), where the delithiation process can occur without the presence of high resistances. In the case of capacities, both cathodes show similar values.

Impendance response of LFP/PEDOT(cast) and C-LFP/PEDOT cathodes during charge and discharge process

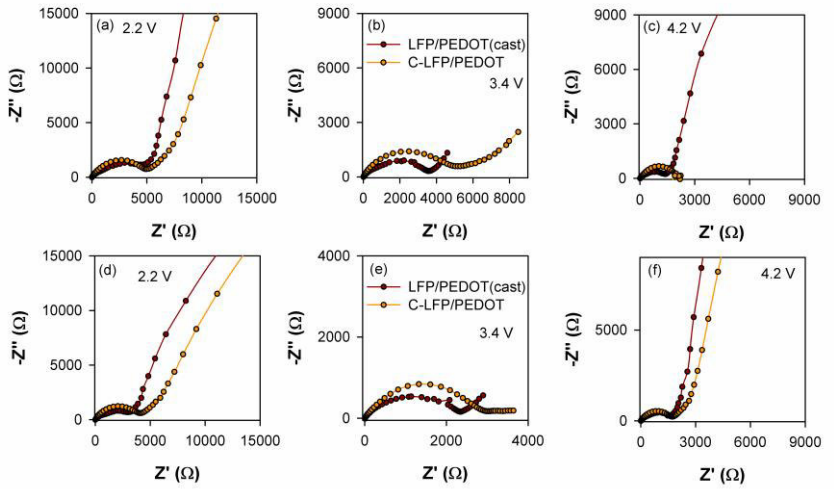

Fig.S3. Nyquist diagrams experimentally measured at different stages of charge (a, b and c) and discharge (d, e and f) for: LFP/PEDOT(cast), and C-LFP/PEDOT.

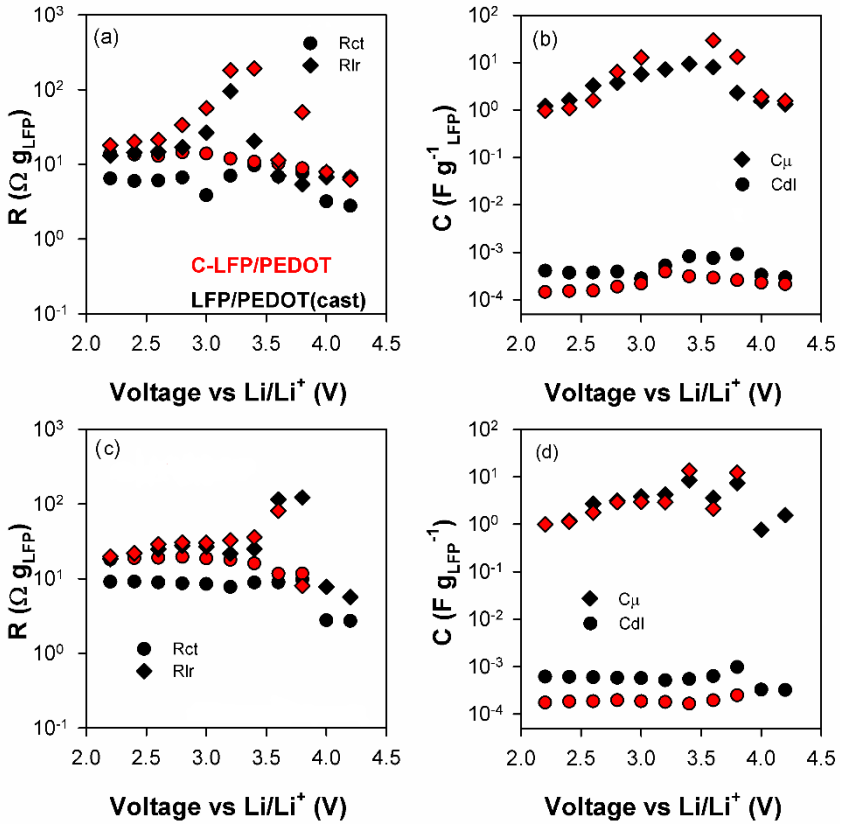

Fig. S4. Parameters fitting in discharge process (a, b) and charge process (c, d) for LFP/PEDOT(cast) (black symbols) and C-LFP/PEDOT (red symbols): the high frequency response, i.e. transference resistance (R_{ct}) and the double layer capacity (C_{dl}) are symbolized by circles (●), and the low frequency response, i.e. the resistance to the lithiation reaction (R_{lr}) and the chemical capacity (C_{μ}) to rhombus (◆).

Fig. S3 shows Nyquist diagrams of charge and discharge process a different voltages of the LFP/PEDOT(cast) and C-LFP/PEDOT cathodes. Main parameters get from fitting are plot in Fig S4. R_{ct} resistances are in the same order of magnitude than the observed for LFP/PEDOT(blend), which confirms the good activity of PEDOT as e^- and Li^+ supplier in the cathode. Nevertheless, R_{lr} values are ca. one

order of magnitude higher than the registered for LFP/PEDOT(blend). This fact suggests that the synthesis method mainly affects on the resistance related to the intercalation/extraction Li^+ hindrance in the oxide host. In the case of the capacities values, the four cathodes show similar values, with a peak around 3.6V (redox reaction), so it is the resistance value which determine the best behavior.

Effect of the C-coating at low frequencies in the LFP electrodes

In case of C-LFP electrode an extra arc at low frequencies is present, which needs a resistance (R_c) and a capacitance (C_c) parallel subcircuit to get a good fitting, as it can be seen in Fig S5. a. In Fig S5.b values of these parameters are plotted for charge and discharge profiles. It is observed that resistance data are approximately constant in the range voltage with a value close to 0.5 g, which is almost two orders of magnitude lower than the other two resistances. The capacities related to the C film are close to 10^{-5} F g^{-1} that is two orders of magnitude lower than the registered for C_{dl}.

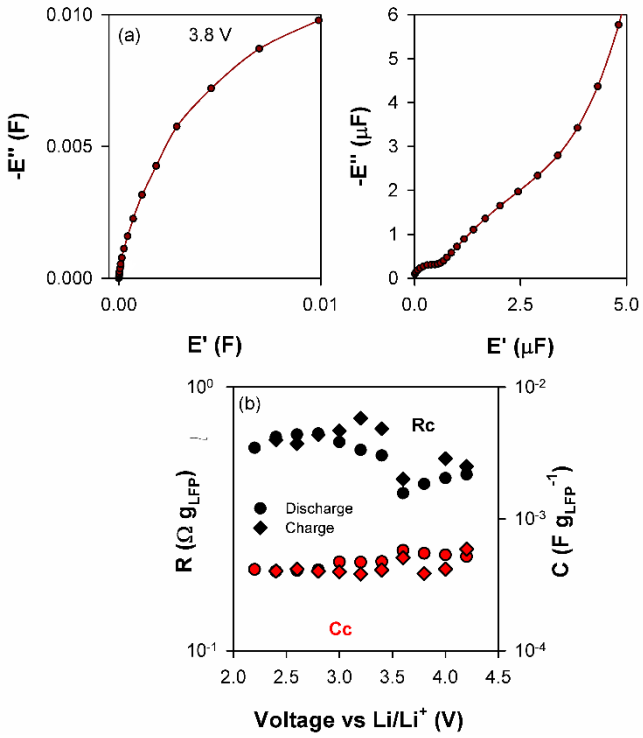

Fig. S5. a) Representation of capacitances to 3.8V b) Experimental data corresponding to R_c and C_c plots of C-LFP in discharge process, circles (●), and charge process, rhombus (◆) for a several process. Black is representing resistance and red data capacitance.

4

Publication 2

4.1. Candidate's contribution

In this case of Publication 2, the nature and extent of my contribution to the work was the following:

Nature of contribution	Extent of contribution
• Review of existint literatura about Li-O_2 batteries • Design experiments. analysis and discussion the experimental data • Performance the impedance study • Development and discussion of the validity the impedance model • Write the manuscrit drafts. Edit the manuscrit in accordance with the comments provided by co-authors.	70 %

4.2. Published manuscript

Marta Haro, Nuria Vicente, Germà Garcia-Belmonte. Oxygen Reduction Reaction Promotes Li^+ Desorption from Cathode Surface in Li-O_2 Batteries, *Advanced Materials Interfaces*, **2015**, 2 (16), 1500369.

Oxygen Reduction Reaction Promotes Li^+ Desorption from Cathode Surface in Li-O_2 Batteries

Marta Haro*, Nuria Vicente, and Germà Garcia-Belmonte*

Photovoltaic and Optoelectronic Devices Group, Departament de Física, Universitat Jaume I, 12071 Castelló, Spain

Correspondign authors Email: mharo@uji.es, garciag@uji.es

Abstract

Li-O_2 batteries are claimed to be one of the future energy storage technologies since it could provide a specific energy as high as 3500Wh kg^{-1}. A great number of scientific and technological challenges should be solved firstly to transform Li-O_2 battery from a promise to real practical devices. Proposed mechanisms for oxygen reduction assume a reservoir of solved Li^+ ions in the electrolyte. However, the role that adsorbed Li^+ on the electrode surface might have on the overall oxygen reduction reaction (ORR) has not deserved much attention. Adsorbed Li^+ consumption is monitored here providing a new perspective on the design of Li-O_2 batteries. The discharge process of a Li-air battery has been analyzed by impedance spectroscopy identifying kinetically-separated steps. Adsorbed Li^+ is inferred from extended electrochemical double layer capacitance, which depends on the carbon matrix surface area. The presence of O_2 drastically reduces the amount of adsorbed Li^+ signaling the kinetic competition between Li^+ surface adsorption and its consumption only for potentials corresponding to the oxygen reduction reaction. Noticeably double layer capacitance remains unaltered after cycling. This fact suggests that the ORR products (Li_2O_2 and Li_2CO_3) are not

covering the internal electrode surface, but deposited on the outer electrode-contact interface, hindering thereby the subsequent reaction. Current results show new insights into the discharge mechanism of Li-O_2 batteries and reveal the evidence of Li^+ desorption from the C surface when the oxygen reduction reaction starts.

Published
Advanced Energy Materials 2 (2015) 1500369,
DOI:10.1002/admi.201500369

1. Introduction

In an increasingly energy-dependent society, the need for renewable energy sources together to its storage is paramount to maintain current society paradigm in a sustainable way with the environment. Albeit Li batteries (LIBs) have invaded the electronic market, their energy densities are usually limited below 250 Wh kg^{-1} [1]. This limitation is mainly originated by the mechanisms through which the chemical energy is stored in the present commercial LIBs that is based on the reversible reaction of the electrode materials with Li^+ ions by means of intercalation mechanisms. Therefore, approaches based on new chemistry are necessary to increase the energy density in batteries, such as Li-S and Li-O_2, which can provide more than 1000 Wh kg^{-1} [1-2]. In particular, Li-O_2 batteries have received a great deal of attention as they can deliver the highest energy density among any other type of batteries. Li^+ ions and O_2 directly react with each other in the absence of any heavy transition metals or crystal framework. [3] Nevertheless, Li-O_2 battery technology is in its infancy and many fundamental issues are needed to be addressed before their practical application.

The chemical energy storage in Li-O_2 batteries is based on the oxygen reduction reaction (ORR) during discharge and oxygen evolution reaction (OER) in the charge, 2 Li^+ + O_2 + 2 e^- ⇌ Li_2O_2 (E^o = 2.96 V, with theoretical specific energy of 3500 $Whkg^{-1}$). To date, Li_2O_2 has been identified as the main discharge product by different techniques like Raman spectroscopy [4] and AFM [5]. Li_2O_2 is electronically insulating, very oxidative and insoluble, precipitating onto the electrode what causes the increase of the necessary potential for oxygen evolution reaction (OER) and the oxidation of the carbon electrode and/or electrolyte giving Li_2CO_3, [6] and as consequence the decrease of the cycleability of the Li-O_2 battery. Also, some authors note that the insulating nature of Li_2O_2 avoids its possible reduction to Li_2O, in this situation, Li-O_2 batteries would provide energy densities as high as 5200 Wh kg^{-1} [7].

It is then noticeable that to fully exploit the capacity of Li-O_2 batteries, the thermodynamic and kinetic mechanisms that govern and limit their functioning must be understood. From the pioneering studies of Abraham et al. [8] on the ORR to date, the oxygen reduction reaction has been widely analyzed in Li-O_2 batteries [9], and several models have been proposed, which have been recently unified by Bruce et al. [10]. Generally, the adsorption of O_2 molecules onto the cathode with one electron interchanged with the electrode is considered as the first step (O_2 + e^- ⇌ O^{2-}, E^o = 2.71 V). This adsorbed O^{2-} reacts with Li^+ ions to produce LiO_2 adsorbed or as solid dissolved in the electrolyte. Depending on the solvent nature and the chemisorption strength with the cathode different mechanisms have been proposed for the reaction of the adsorbed LiO_2 with Li^+ ions until Li_2O_2 is reached as final product. In all these studies, the ORR starts with the reduction of oxygen in the context of free electrode surface and solved Li^+ ions in the electrolyte. However, the role that adsorbed Li^+ ions on the electrode surface might have on the overall ORR has not deserved much attention. This last contribution was pointed out by Qu et al. [11], although no experimental evidence was

provided. The monitoring for the first time of the desorption process of Li^+ ions induced by ORR provides here revealing insights on the cathode surface processes in Li-O_2 batteries.

In this manuscript, Li-O_2 discharge process in different cathodes has been monitored by electrochemical impedance spectroscopy (EIS). This technique has been recently used suggesting that the overpotential during discharge is caused by internal resistance, and is dominated by the charge transport through the deposited Li_2O_2 at the end of discharge. [6, 12] Our study is based on a cathode made by carbon Super P with 30% of NiOCoO as catalyst in the presence and absence of O_2. Actually, both cathodes (with and without O2) show the same impedance spectra from 4.0 to 2.7 V, in which extended electrochemical double layer capacitance (EDLC) made up by adsorbed Li^+ is observed. This behavior has been verified on different systems and tested that is dependent on the surface area of the cathode. At lower voltages, the electrode in the presence of O_2 shows a huge capacitance increase at the same time that the EDLC is reducing. This fact evidences the depletion of the adsorbed Li+ during the ORR. The results show three steps with their characteristic reaction time and resistance in the Li-O_2 discharge: i) interfacial phenomena, ii) extended electrochemical double layer capacitance (EDLC), and iii) chemical capacitance generated by oxygen reduction reaction (ORR Capacitance). This study gives new insights onto the Li-O_2 discharge mechanism provided by impedance spectra, and highlights the key contribution on the overall ORR of adsorbed Li^+ on the electrode surface.

2. Results and discussion

2.1. Electrochemical behavior in the presence and absence of O2

Figure 1a shows the cyclic voltammetry (CV) of SP@30NiOCoO in the presence of O_2 during cycling and in absence of O_2 (third cycle). Without O_2, the CV signal shows some hysteresis (in the order of few mA g_c^{-1}) without any remarkable peak (inset of Fig. 1a). This shape is characteristic of supercapacitors in which the hysteresis is attributed to the extended electrochemical double layer capacitance (EDLC) built by the adsorption of Li^+ ions onto the carbon surface [13]. In the present case, the hysteresis is low because the surface area of the carbon matrix is small (S_{BET}=75 m^2 g^{-1}) compared to the carbon materials used for supercapacitors. The CV changes drastically in the presence of O_2, where a cathodic peak is observed with an onset at 2.9 V and the maximum at 2.4 V, with the typical shape reported in the literature [4, 14]. The shift of ORR peak from 2.7 V to 2.4 V has been attributed to the EC mechanism, that is, electrochemical reduction ($O_2 + e^- \rightarrow O^{2-}$) followed by a chemical step (reaction of Li^+ with O^{2-}) that severely deplete the concentration of O^{2-} [4]. With the number of cycles, the cathodic peak reduces conspicuously, and in rather less extension the anodic peak. For this air cathode (of low S_{BET}), the capacity is ca. 500 mAh g_c^{-1} (Figure SI.1). The main species formed in the discharge process is Li_2O_2, which is almost decomposed during charge process, as revealed the XPS spectra (Figure SI.2) that provides molecular percentage of Li in the form Li_2O_2 at 2.4 V and 3.4 V after 3, 5 and 7 cycles (Table 1). XPS also shows that, in this case, Li_2CO_3 is formed once Li_2O_2 (very oxidative species that can react with the C of the electrode and/or the electrolyte) is produced, [6, 15] albeit in little amount. Nevertheless, the decomposition of this residue is low and while Li_2O_2 almost disappears during charge process, the residue reduces nearly a half. The evolution of the electrode composition is observed by XPS, where we could observe that Li_2CO_3 is accumulated, as also pointed out by XRD (Figure 1b).

Before cycling, the electrode shows the peaks ascribed to the mesh substrate and the catalyst, NiOCoO, the same result than the electrode at 3.4 V (before reduction process) after being cycled 3 times. Nevertheless, the characteristic peaks of Li_2O_2 are observed after 5 CV, peaks that disappear after 7 cycles, where the characteristic Li_2CO_3 peaks are clearly observed.

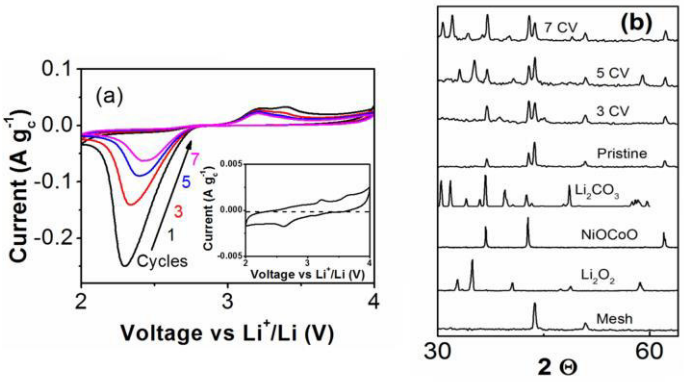

Figure 1a.CV of SP@30NiOCoO in the presence of O_2 along different number of cycles and in the absence of O_2 (inset). Scan rate: 0.1 mV s^{-1}. **b.** XRD patters of air cathode before being cycled (pristine) and after 3, 5 and 7 cycles. The patters of the mesh, Li_2O_2, NiOCoO, and Li_2CO_3 are also shown.

Sample	Specie (% mol)	
	Li (Li_2O_2)	Li (Li_2CO_3)
3 cycles, 2.4 V	3.6	1.4
3 cycles, 3.4 V	0.3	0.6
5 cycles, 3.4 V	5.6	11.2
7 cycles, 3,4 V	6.9	19.4

Table 1. Molecular percentage of Li in the form of Li_2O_2 and Li_2CO_3 determined by XPS (all data shown in SI) in the sample cycles three, five or seven times at different stop voltage: 2.4 and 3.4 V.

In order to assay the electrode in a representative state during Li-O_2 charge-discharge process, the electrochemical impedance spectroscopy was performed after three CV. The first cycle is discarded because it is not representative of a steady operation, and atthe third cycle residual compounds are negligible, as XPS (Table 1 and Figure SI.2) and XRD (Figure 1.b) data demonstrate. The EIS measurements were carried out potentiostatically at different stages of Li^+ ion insertion at a very low rate to ensure the steady-state condition. Figure 2 shows three different Nyquist diagrams, representative of the different stages during the discharge process. The low frequencies range of the impedance spectra (below 5 Hz, indicated in Figures 2a and 2b) of both systems give the same Nyquist plot from ca. 3.6 to 2.8 V. At 4.0 V (Figure 2a), the system with O_2 shows lower resistive behavior probably due to the degradation of the carbon cathode and the electrolyte solvent in the presence of O_2, since carbon becomes unstable at voltages above 3.5 V [16]. At 2.6 V (and lower voltages), the Nyquist plot of the cathode in presence of O_2 changes drastically and the arc associated to the low frequency decreases dramatically. A new electrochemical feature is now observed at frequencies lower than 10 mHz (Figure 2f). This process should be related to the limiting step for ORR and O_2 diffusion. At high frequencies (above 5 Hz, Figures 2d-f), the Nyquist plots of the battery in absence of O_2 show one arc while there are two smaller arcs in the presence of O_2.

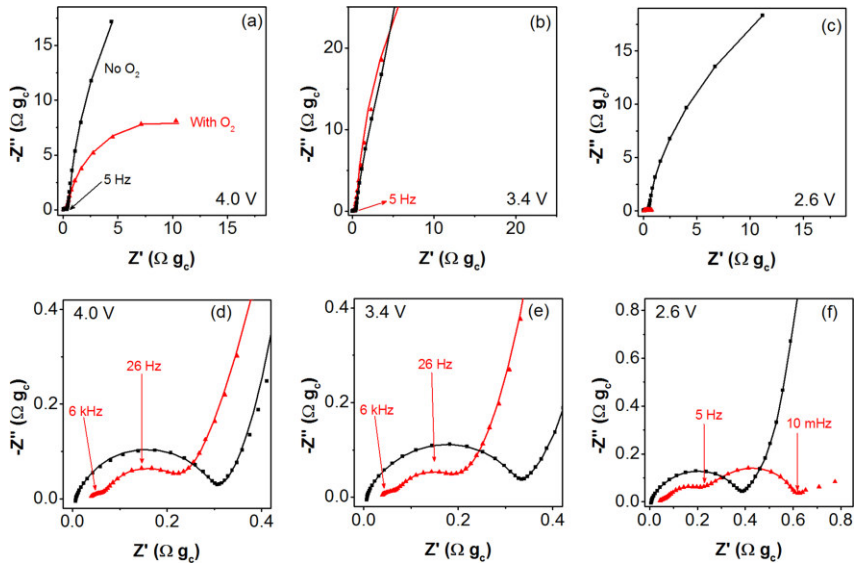

Figure 2. Nyquist plots of SP@30% NiOCoO with and without O_2. The low frequency (<5 Hz) region of the EIS is observed in graphs a-c, and the figures d-f show an enlargement of the high frequency region. The experimental data are represented by solid symbols and the lines are obtained by the fitting with the equivalent circuit model shown in Figure 4b.

To gain deeper insight on the Li-O_2 discharge kinetics, the impedance data are represented in terms of capacitance ($C = 1/i\omega Z$) in Figure 3. In this representation, the real part, C', is related to the electrode charging while the associated resistance caused by kinetic limitations determines the value reached by the imaginary part, C''. As explained elsewhere [17], capacitive representation allows straightforwardly extracting contributing capacitors and, consequently, inferring on charging mechanisms. Each arc in a capacitance plot is assimilated to a RC series subcircuit. In the region of low frequencies (below 5 Hz) an arc is observed that closes to ca. 6.5 F g_c^{-1} in the two systems (with and without O_2) within the voltage range 4.0-2.8 V. At lower voltages, a new arc is observed in the presence of O_2 that is more than two orders of magnitude higher than the previous one, and hides

it. At high frequencies (see Figure SI.3), smaller arcs linked to different capacitive features in the multistep discharge process are observed for both systems, although the capacitance in presence of O_2 is larger than in its absence.

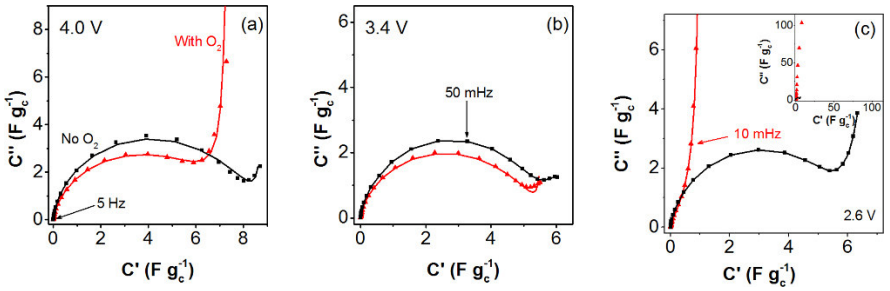

Figure 3. Capacitance plot of SP@30% NiOCoO with and without O_2. The experimental data are represented by solid symbols and the lines are obtained by the fitting with the equivalent circuit model shown in Figure 4.b.

2.2. Electrode mechanisms through equivalent circuits

Figure 4a represents the capacitance spectra, C', vs. characteristic time (inverse of measuring frequency) of the SP@30NiOCoO cathode in the presence (solid lines) and absence (dashed lines) of O_2. The horizontal axis is also represented in frequency scale, inversely than usually drawn, from high to low frequency in order to maintain the same reading direction of the equivalent circuit model. In this representation, a plateau is demonstrative of a capacitive step in the discharge mechanism occurring at a certain frequency range. For electrodes with and without O_2, two plateaus are observed: the first one at intermediate frequencies (ca. 100 Hz) is O_2 dependent, while the second at low frequencies (ca. 0.01 Hz) is O_2 independent only at higher potentials. These two plateaus correspond to the two arcs described in Figures 3 and SI.3. The plateau at low frequencies is unaltered by the presence of O_2 in all the discharge process until 2.6

V. Noticeably below this potential the presence of O_2 induces the capacitance decreasing by one order of magnitude showing a plateau that ends at 10 mHz. At lower frequencies the capacitance further increases in relation with the diffusion and reaction process discussed in Figure 2.f.

By observing Figure 4a one can distinguish three steps in the discharge process, which are marked with squares and represented in the different subcircuits of the equivalent circuit model shown in Figure 4b. The fitting of the proposed equivalent circuit model is represented in Figures 2 and 3 with solid lines. The observed steps during discharge are:

i) Interfacial phenomena (high frequency: > 5 Hz) that is O_2 dependent. In the presence of O_2 two arcs are observed in the Nyquist plot, which are represented by two resistances (R_{i1} and R_{i2}) in parallel with two capacitances (C_{i1} and C_{i2}). In the absence of O_2, only one arc is observed that is equivalent to a resistance (R_i) in parallel to the capacitance (C_i).

ii) Extended electrochemical double layer capacitance (EDLC) (intermediate frequency: 10 mHz $< f <$ 5 Hz) that is O_2 independent at high potentials. This mechanism is connected to the Li^+ adsorption on the internal electrode surface. This capacitance, C_{EDL}, is associated to an arc in the C'' vs C' representation that can be modeled by a series RC circuit [17-18]. The associated resistance Rads accounts for the Li^+ transport in the electrolyte within the porous matrix. More details of this subcircuit model are in Supporting Information.

iii) Chemical ORR capacitance (low frequency: <10 μHz) that only appears in the presence of O_2. When O_2 starts to react (at 2.8 V and below) a new parallel branch to the EDLC is represented in the equivalent circuit model by the chemical capacitance, C , in series to the associated resistance, R_{ORR}, accounting for the reduction reaction.

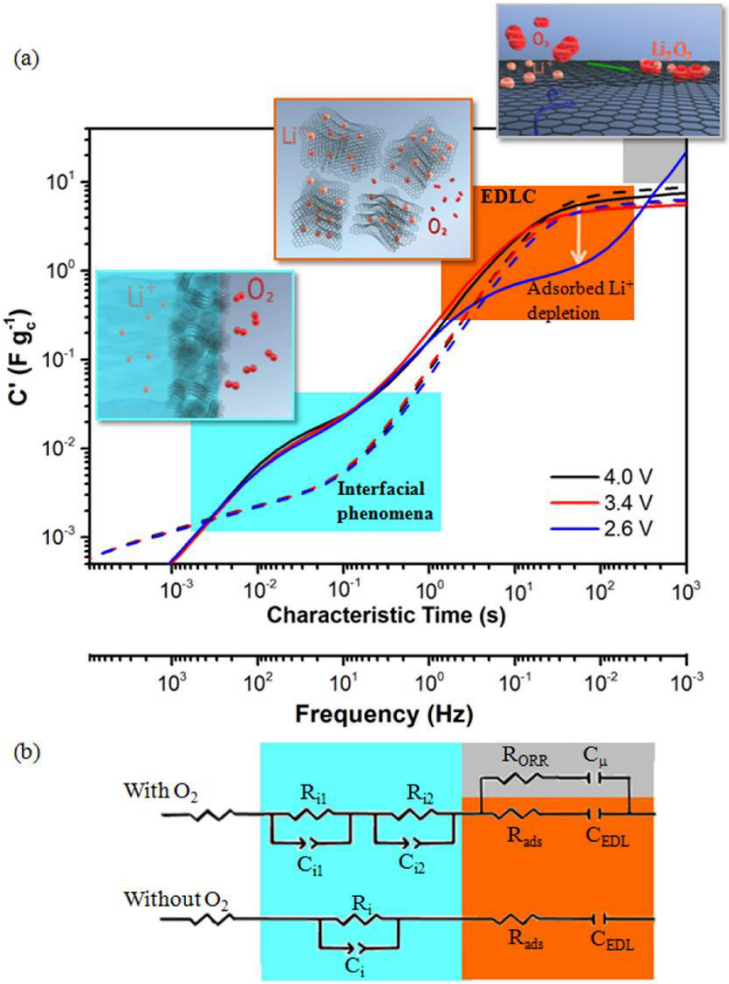

Figure 4.(a)C' vs characteristic time and frequency (in opposite order than usual, from fast to slow electrochemical processes for a more intuitive reading) for SP@30NiOCoO in the presence (solid lines) and absence (dashed lines) of O_2. Inset: Scheme of the three processes of the Li-O_2 discharge mechanism. The ORR is represented on the cathode surface by a graphitic layer, in which adsorbed Li^+ react with O_2. (b) Equivalent circuit model for the system in the absence and presence of O_2.

2.3. Interfacial phenomena

The electrochemical processes related to the interface are monitored by EIS at high frequencies. In the absence of O_2, a single semi-circle is observed in the Nyquist representation (Figure 2 d-f) that is associated with a semi-circle to the C'' vs C' representation, Figure SI3. This capacitance, C_i, and resistance, R_i, can be associated to the impedance generated at the contact interface between the electrode and the electrolyte solution. [19] In the presence of O_2, two small arcs are distinguished in Figure 2 d-f. One of the arcs can be ascribed to the formation of the isolating layer formed by Li_2O_2 and Li_2CO_3(as XPS and XRD shown) and the other to the impedance at the contact interface, as it has been assigned in the absence of O_2. In any case these resistive elements introduce limitations into the overall charging mechanism.

The fitting values obtained by the equivalent circuit model are represented in Figure 5. With the calculated values, we can indicate that C_{i2} and R_{i2} are related to the electrode/electrolyte contact since they are constant independently of the applied voltage. In this assumption, C_{i1} and R_{i1} should be related to the solid electrolyte interface (Li_2O_2 and Li_2CO_3) formed on the cathode, which explains why the capacitance increases with the oxygen reduction reaction.

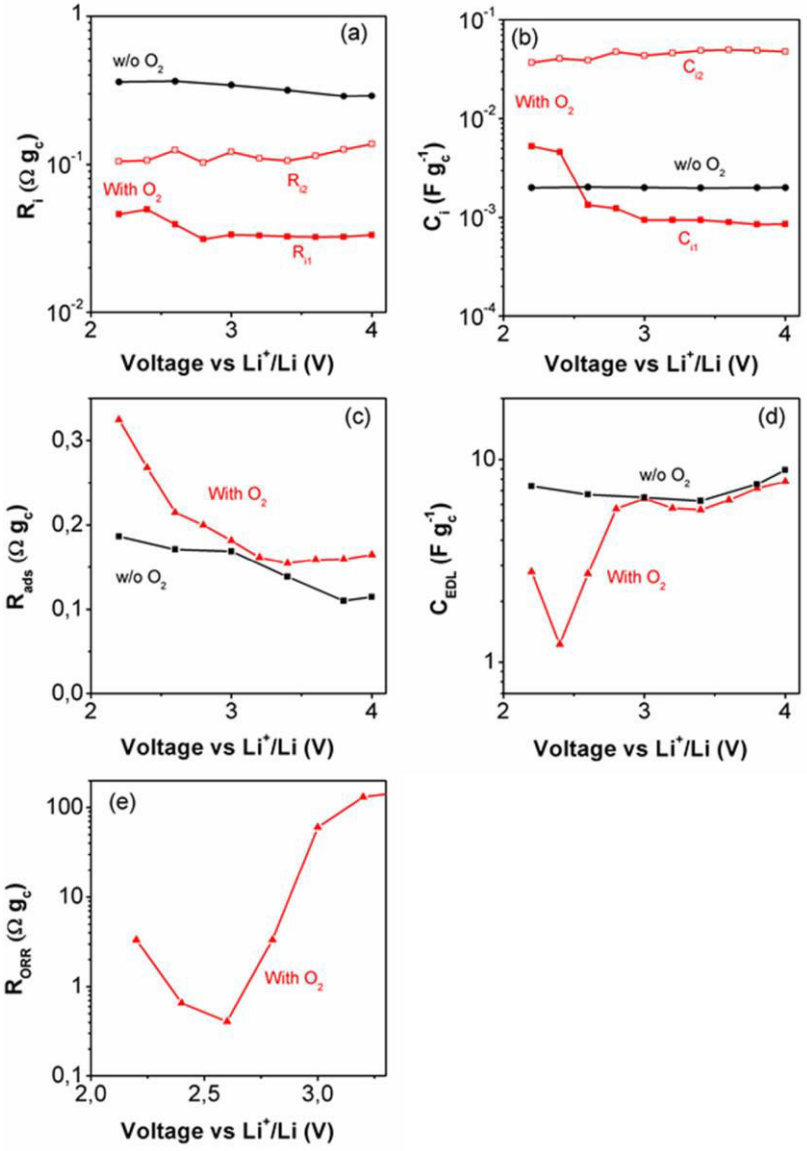

Figure 5. Parameters determined during discharge process by the EIS fitting with the equivalent circuit model shown in Figure 4.b: (a) resistance and (b) capacitance associated to the interface phenomena; (c) resistance, R_{ads}, and (d) capacitance, C_{EDL}, associated to the formation of the electrochemical double layer; (e) parallel resistance, R_{ORR}, which decrease at the applied voltages when the ORR starts.

2.4. Electrochemical double layer capacitance

With the equivalent circuit model (Figure 4b), the main parameters of the Li^+ adsorption step in the discharge process are obtained, Figure 5. In the absence of O_2, the capacity is practically constant, 6.5F gc-1(that corresponds to ca. 8 μF cm_c^{-2} considering an area S_{BET}= 75 $m^2 g^{-1}$), independently of the voltage. This value is within the range of reported electrochemical double layer capacitances in supercapacitors based on carbon materials (5-20 μF cm^{-2}) [13a]. In this case, the capacitance is in agreement with a lower value obtained with supercapacitors when an organic electrolyte is used compared to aqueous electrolytes [20]. Associated to the charge accumulation by physical electro-adsorption there is a resistance that has been related to the ion transport along the tortuous path of the micro/meso-porosity of the carbon matrix [21]. In the presence of O_2, the EDL capacitance is unaltered at high voltages and noticeably decreases when the ORR starts. This is in accordance with recent capacitance analysis. [12] The resistance of the Li^+ adsorption process consistently increases, showing the kinetic competition between Li^+ adsorption and consumption by ORR at voltages lower than 2.8 V. At the same time, the parallel resistance, R_{ORR}, decreases dramatically (close to three orders of magnitude) giving further support to the idea that the current runs along the parallel branch corresponding to the ORR subcircuit in Figure 4b. At lower voltages than ORR reaction, (i.e. 2.2 V), the capacitance of the EDL starts to increase again signaling a full recovering of the double layer features. We infer that the ORR branch in Figure 4b is kinetically favored at potentials 2.4-2.8 V.

To check the role of species involved in the EDLC formation as a step in the discharge mechanism, other systems have been measured for consistency. The same results have been obtained in the absence of catalyst (Figure SI.4) and the study with carbons of different S_{BET} has revealed that EDLC can be considered only dependent on the carbon surface area (Figure SI.5). This point is further discussed in

the SI since depending on the size of the pores the area can be active or not to the formation of the EDL like in the case of the supercapacitors.

In order to analyze the effect of cycling on the formation of the electric double layer, the electrochemical impedance spectrum at 3.4 V (during lithiation process) has been registered along several CV cycles. The Nyquist and capacitance plots are represented in Figure 6 and the obtained fitting parameters in Figure SI.6. Surprisingly, no significant differences are observed in the Nyquist plots and the EDL capacitances are practically constant, independently of the cycling number. This result shows that the electrode textural property is not modified with the number of cycles, and Li^+ cations can freely adsorb in the carbon porosity, independently on the formation of Li_2O_2 and Li_2CO_3, which presence is evidenced by XPS and XRD.

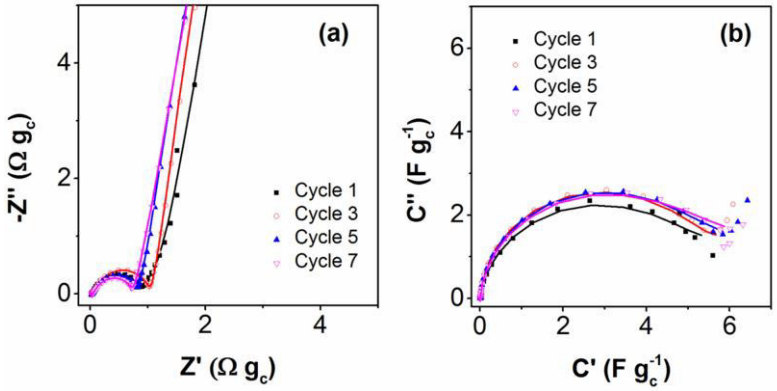

Figure 6. a) Nyquist and b) EDL capacitance plots of the SP@30% NiOCoO air cathode at 3.4 V at different number of CV cycles.

With all the data in mind, the fact that EDL capacitance decreases when ORR starts due to a hiding phenomenon can be discarded since the EDL capacitance remains unaltered after cycling. If the reaction products (mainly Li_2O_2) partially cover the carbon surface one would

expect a reduction of the EDLC with cycling that does not occur at 3.4 V (Fig. 6b). Therefore, the EDLC decrease with ORR should be associated to Li^+ desorption, which can be either caused by: i) displacement of physisorbed Li^+ by chemisorbed O^{2-} when ORR starts, followed by the subsequent chemical reaction between adsorbed O^{2-} with the solved Li^+ in the electrolyte or ii) to a direct reaction between the physisorbed Li^+ with the molecular O_2 at the oxygen reduction potential to give Li_2O_2. Nevertheless, once the potential of ORR is surpassed (i.e. 2.2 V), the EDL capacitance increases again, what suggests that Li_2O_2 is not forming a monolayer on the top of the carbon surface. This idea is also supported by the study of C_{EDL} with the number of cycles, in which is observed that the same capacitance is obtained independently on the number of CV cycles, and then, on the formation of Li_2O_2 and Li_2CO_3. This result discards that the transport limitation and the cause of the low rechargeability of the current battery is the formation of an insulating layer (Li_2CO_3 or Li_2O_2) on the carbon porosity, as some authors have reported. [6, 22] Therefore, the transport blocking most probably become from the accumulation of these two species on one of the two sides of the electrode (electrode-electrolyte or electrode-O_2). Since the surface phenomena monitored by EIS (related to the electrode-electrolyte interface) are scarcely affected by the presence of these two species, one can infer that the accumulation of both, Li_2O_2 and Li_2CO_3, is at the electrode-O_2 interface, that finally limits the O_2 diffusion. [23] Noticeably EDLC remains unaltered after cycling. This fact suggests that the ORR products (Li_2O_2 and Li_2CO_3) are not covering the internal electrode surface, but deposited on the outer electrode-O_2 interface, hindering thereby the subsequent reaction.

In all the models for Li-O_2 discharge mechanism, the surface of the cathode is considered as a raw graphitic layer where the Li^+ ions arrive from the electrolyte side. This study demonstrates that the surface is already covered by adsorbed Li^+ when ORR starts what could imply that once the soluble O_2 react with Li^+, the molecular O_2

can first react with the adsorbed Li^+ on the surface nearly the O_2, forming Li_2O_2 and avoiding further reaction. Qu et al. [11] reported that the discharge capacitance can be increased with O_2 pressure higher than 1 atm since the electrolyte was forced back from the interface and the complete wetting of the cathode is avoided. Therefore, adsorbed Li^+ consumption provides a new context of the cathode surface where the oxygen reduction reaction develops.

2.5. ORR Capacitance

At low voltages the reduction reaction of O_2 takes place. ORR is the main process in Li-O_2 batteries that provides the unique high capacity, but the main drawback for following this reaction by EIS is its extremely slow rate; it is registered at frequencies below 10 mHz. For this reason, the fitting of the data is only partial. In Figure 4b has been represented by a resistance in series with the chemical capacitance for the purpose of clarity. Nevertheless, in the Nyquist plot is observed that the real part of the impedance (-Z') increases, then signaling an extra resistive behavior in addition to the capacitive one observed in Figure 4a. For this reason, more elements than the chemical capacitance are certainly needed. It is indeed the final limiting step related to the O_2 diffusion through different layers. It is obvious that it is necessary to fast up this process in order to make it fully observable by impedance methods.

3. Experimental

All the agents were purchased from Sigma Aldrich, and were used as received. The cathodes were prepared by painting a carbon/PVdF slurry onto a stainless steel mesh. The slurries were prepared by mixing carbon black/PVdF/catalyst (60:10:30 % wt) and the

addition of 1-Methyl-2-pyrrolidone. All the cathodes were dryed in vacuum, at 110 ºC overnight. Mixed-metal oxides are proved to be good catalysts for both ORR and OER in Li-O_2 batteries. [24] In this study, a commercial nanopowder, nickel cobalt oxide, (of size lower than 150 nm, CAS 5859-45-0, Sigma-Aldrich) was observed to accelerate H_2O_2 oxidation (Figure SI.8) and, consequently, it is a good candidate as catalyst for Li-O_2 batteries,[25] albeit no reference of its use has been found in the literature. Despite its study is out of the topic of this manuscript, we have seen that its main contribution is the reduction of the charge transfer resistance (Figure SI.9).

Cell assembly (Swagelok type) was carried out in a N_2 filled glovebox. This consists simple in clamping together a Li metal foil anode, an electrolyte-soaked separator, the electrolyte that is 1M hexafluorophosphate lithium salt ($LiPF_6$) dissolved in tetraethylene glycol dimethyl ether (TEGDME), the cathode under study and the stainless steel current collector. The cathode collector is a tube in which pure O_2 (>99.9999 to avoid contamination issues) flows, the pressure is maintained at 1 atm during all the experiment.

Electrochemical characterization was performed using a PGSTAT-30 potentiostat from Autolab equipped with an impedance module. The CV was carried out in the voltage window of 2-4.0V at 100 $V\ s^{-1}$ scan rate. After 3 CV scans, the EIS spectra were performed (every 200 mV) within this voltage range with an amplitude perturbation of 10 mV, and in the frequency range of 1 MHz to 1 mHz. The approximation to the different voltages of measurement was potentiostically controlled at 10 $V \cdot s^{-1}$ to assure the quasi-equilibrium state of the battery. Also, before each measurement the system was stabilized during 30 minutes. All the data are normalized to the carbon mass.

The cycled electrodes were characterized by means of X-ray powder diffraction (XDR) using Bruker AXS-D4 Endeavor Advance X-ray

diffractometer using Cu_{λ} radiation. X-ray photoelectron spectroscopy (XPS) was performed on Sage 150 de Specs with non- monochromatic radiation Al Kα (1486.6 eV) to 20 mA and 13 kV, a constant pass energy 75 eV for global analysis and 30 eV for specific binding energy of each element analysis, and an area measuring 1x1 mm^2. The base pressure of XPS chamber was 7×10^{-9} hPa. XPS spectra were fitted with CasaXPS software, which models the Gauss-Lorentzian contributions, after background subtraction. Also, energy spectra were calibrated by setting the C 1s photoemission peak for sp^2-hybridized carbon to 284.8 eV. Samples were washed out by anhydrous dimethyl carbonate (DMC, Sigma-Aldrich) solvent several times, and dried in a vacuum chamber at 60 ºC for 2 h previous XRD and XPS measurements. [26]

4. Conclusions

This manuscript analyzes the discharge process of Li-O_2 batteries by impedance spectroscopy and provides a novel equivalent circuit model. In this model, different electrochemical processes during discharge mechanism are identified: i) interfacial phenomena, ii) extended electrochemical double layer capacitance (EDLC), and iii) ORR chemical capacitance. EDLC has been monitored in Li-O_2 batteries and it is observed to be independent of the presence of O_2 at voltages higher than those at which oxygen reduction reaction occurs. Noticeably EDLC is fully recovered after electrode charging, and remains unaltered after cycling. This fact suggests that the ORR products (Li_2O_2 and Li_2CO_3) are not covering the internal electrode surface, but deposited on the outer electrode-O_2 interface, hindering thereby the subsequent reaction. At this moment, further research is necessary to elucidate if these adsorbed Li^+ at the internal electrode double layer can directly react with the O_2 molecules at the voltage where ORR starts or they are merely displaced by the reduction of

O_2 molecules. The novel equivalent circuit model and the consideration that Li^+ ions are already adsorbed on the carbon surface when ORR starts provide new tools in the study and design of Li-O_2 cathodes.

Acnknowlegments

We thank financial support from Generalitat Valenciana (ISIC/2012/008 Institute of Nanotechnologies for Clean Energies). The authors acknowledge Dr. Conchi Ania from National Institute of Carbon for providing PSCo and AG carbons and their characterization.

References

1. P. G. Bruce, S. A. Freunberger, L. J. Hardwick, J.-M. Tarascon, Nature materials 2012, 11, 19-29.
2. N. S. Choi, Z. Chen, S. A. Freunberger, X. Ji, Y. K. Sun, K. Amine, G. Yushin, L. F. Nazar, J. Cho, P. G. Bruce, Angewandte Chemie International Edition 2012, 51, 9994-10024.
3. (a) Z. Peng, S. A. Freunberger, Y. Chen, P. G. Bruce, Science 2012, 337, 563-566; (b) H.-G. Jung, J. Hassoun, J.-B. Park, Y.-K. Sun, B. Scrosati, Nature chemistry 2012, 4, 579-585; (c) B. G. Kim, H.-J. Kim, S. Back, K. W. Nam, Y. Jung, Y.-K. Han, J. W. Choi, Scientific reports 2014, 4; (d) Z. L. Wang, D. Xu, J. J. Xu, L. L. Zhang, X. B. Zhang, Advanced Functional Materials 2012, 22, 3699-3705.
4. Z. Peng, S. A. Freunberger, L. J. Hardwick, Y. Chen, V. Giordani, F. Bardé, P. Novák, D. Graham, J. M. Tarascon, P. G. Bruce, Angewandte Chemie 2011, 123, 6475-6479.

5. R. Wen, M. Hong, H. R. Byon, Journal of the American Chemical Society 2013, 135, 10870-10876.
6. B. McCloskey, A. Speidel, R. Scheffler, D. Miller, V. Viswanathan, J. Hummelshøj, J. Nørskov, A. Luntz, The Journal of Physical Chemistry Letters 2012, 3, 997-1001.
7. B. Scrosati, K. M. Abraham, W. A. van Schalkwijk, J. Hassoun, Lithium Batteries: Advanced Technologies and Applications, Wiley, 2013.
8. C. O. Laoire, S. Mukerjee, K. Abraham, E. J. Plichta, M. A. Hendrickson, The Journal of Physical Chemistry C 2009, 113, 20127-20134.
9. (a) M. D. Radin, D. J. Siegel, Energy & Environmental Science 2013, 6, 2370-2379; (b) C. O. Laoire, S. Mukerjee, K. Abraham, E. J. Plichta, M. A. Hendrickson, The Journal of Physical Chemistry C 2010, 114, 9178-9186; (c) M. Safari, B. D. Adams, L. F. Nazar, The Journal of Physical Chemistry Letters 2014, 5, 3486-3491; (d) B. Horstmann, B. Gallant, R. Mitchell, W. G. Bessler, Y. Shao-Horn, M. Z. Bazant, The Journal of Physical Chemistry Letters 2013, 4, 4217-4222; eJ.-J. Xu, Z.-L. Wang, D. Xu, L.-L. Zhang, X.-B. Zhang, Nature communications 2013, 4.
10. (a)L. Johnson, C. Li, Z. Liu, Y. Chen, S. A. Freunberger, P. C. Ashok, B. B. Praveen, K. Dholakia, J.-M. Tarascon, P. G. Bruce, Nature chemistry 2014, 6, 1091-1099; (b) K.-H. Xue, E. McTurk, L. Johnson, P. G. Bruce, A. A. Franco, Journal of The Electrochemical Society 2015, 162, A614-A621.
11. C. Tran, X.-Q. Yang, D. Qu, Journal of power sources 2010, 195, 2057-2063.
12. J. Højberg, B. D. McCloskey, J. Hjelm, T. Vegge, K. Johansen, P. Norby, A. C. Luntz, ACS applied materials & interfaces 2015, 7, 4039-4047.

13. (a) P. Simon, Y. Gogotsi, Nature materials 2008, 7, 845-854; (b) M. Haro, G. Rasines, C. Macias, C. Ania, Carbon 2011, 49, 3723-3730.
14. (a) S. Y. Kim, H.-T. Lee, K.-B. Kim, Physical Chemistry Chemical Physics 2013, 15, 20262- 20271; (b) F. Li, R. Ohnishi, Y. Yamada, J. Kubota, K. Domen, A. Yamada, H. Zhou, Chem. Commun. 2013, 49, 1175-1177.
15. S. A. Freunberger, Y. Chen, N. E. Drewett, L. J. Hardwick, F. Bardé, P. G. Bruce, Angewandte Chemie International Edition 2011, 50, 8609-8613.
16. M. M. Ottakam Thotiyl, S. A. Freunberger, Z. Peng, P. G. Bruce, Journal of the American Chemical Society 2012, 135, 494-500.
17. F. Martinez-Julian, A. Guerrero, M. Haro, J. Bisquert, D. Bresser, E. Paillard, S. Passerini, G. Garcia-Belmonte, The Journal of Physical Chemistry C 2014, 118, 6069-6076.
18. M. Haro, T. Song, A. Guerrero, L. Bertoluzzi, J. Bisquert, U. Paik, G. Garcia-Belmonte, Physical Chemistry Chemical Physics 2014, 16, 17930-17935.
19. W.-C. Chen, T.-C. Wen, Journal of power sources 2003, 117, 273-282.
20. C. Vix-Guterl, S. Saadallah, K. Jurewicz, E. Frackowiak, M. Reda, J. Parmentier, J. Patarin, F. Beguin, Materials Science and Engineering: B 2004, 108, 148-155.
21. F. Béguin, E. Frackowiak, Carbons for electrochemical energy storage and conversion systems, CRC Press, 2009.
22. P. Albertus, G. Girishkumar, B. McCloskey, R. S. Sánchez-Carrera, B. Kozinsky, J. Christensen, A. Luntz, Journal of The Electrochemical Society 2011, 158, A343-A351.
23. S. Sandhu, J. Fellner, G. Brutchen, Journal of power sources 2007, 164, 365-371.
24. (a) J.-J. Xu, Z.-L. Wang, D. Xu, F.-Z. Meng, X.-B. Zhang, Energy & Environmental Science 2014, 7, 2213-2219; (b) J. J.

Xu, D. Xu, Z. L. Wang, H. G. Wang, L. L. Zhang, X. B. Zhang, Angewandte Chemie International Edition 2013, 52, 3887-3890.
25. V. Giordani, S. Freunberger, P. Bruce, J.-M. Tarascon, D. Larcher, Electrochemical and Solid-State Letters 2010, 13, A180-A183.
26. M. H. Rui Wen, and Hye Ryung Byon, Journal of the American Chemical Society 2013, 135, 10870 - 10876.

Figure Captions

Figure 1. (a) CV of SP@30NiOCoO in the presence of O_2 along different number of cycles and in the absence of O_2 (inset). Scan rate: 0.1 mV s^{-1}. (b) XRD patters of air cathode before being cycled and after 3 and 7 cycles. The patters of the pristine mesh, Li_2O_2, $NiO \cdot CoO$, and Li_2CO_3 are also shown.

Figure 2. Nyquist plots of SP@30% NiOCoO with and without O_2. The low frequency (< 5 Hz) region of the EIS is observed in graphs a-c, and the figures d-f show an enlargement of the high frequency region. The experimental data are represented by solid symbols and the lines are obtained by the fitting with the equivalent circuit model shown in Figure 4 b.

Figure 3. Capacitance plot of SP@30% NiOCoO with and without O_2. The experimental data are represented by solid symbols and the lines are obtained by the fitting with the equivalent circuit model shown in Figure 4.b.

Figure 4. (a) C' vs characteristic time and frequency (in opposite order than usual, from fast to slow electrochemical processes for a more intuitive reading) for SP@30NiOCoO in the presence (solid lines) and absence (dashed lines) of O_2. Inset: Scheme of the three processes of the Li-O_2 discharge mechanism. The ORR is represented

on the cathode surface by a graphitic layer, in which adsorbed Li^+ react with O_2. (b) Equivalent circuit model for the system in the absence and presence of O_2.

Figure 5. Parameters determined during discharge process by the EIS fitting with the equivalent circuit model shown in Figure 4.b: (a) resistance and (b) capacitance associated to the interface phenomena;(c) resistance, R_{ads}, and (d) capacitance, C_{EDL}, associated to the formation of the electrochemical double layer; (e) parallel resistance, R_{ORR}, which decrease at the applied voltages when the ORR starts.

Figure 6. (a) Nyquist and (b) EDL capacitance plots of the SP@30% NiOCoO air cathode at 3.4 V at different number of CV cycles. Adsorbed Li^+ consumption is monitored during oxygen reduction reaction (ORR) providing further understanding on the discharge process of Li-O_2 batteries. Adsorbed Li^+ is inferred from extended electrochemical double layer capacitance (EDLC), which is function on the carbon matrix surface area. EDLC is independent of the presence of Li_2O_2 and Li_2CO_3, what indicates that the precipitation occurs at the electrode-O_2 interface and not inside the electrode porosity.

Keyword

Li-O_2 Batteries, Adsorption, Impedance Spectroscopy, Electrochemical Double Layer

Marta Haro*, Nuria Vicente, GermàGarcia-Belmonte*

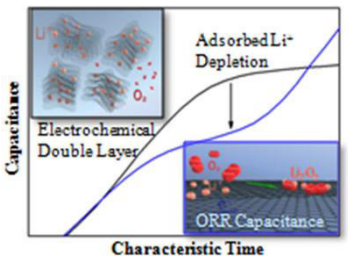

Supporting Information

Oxygen Reduction Reaction Promotes Li^+ Desorption from the Cathode Surface in Li-O_2 Batteries

Marta Haro*, Nuria Vicente, and Germà Garcia-Belmonte*

Photovoltaics and Optoelectronic Devices Group, Departament de Física, Universitat Jaume I, 12071 Castelló, Spain

Email: mharo@uji.es,garciag@uji.es

28 August 2015

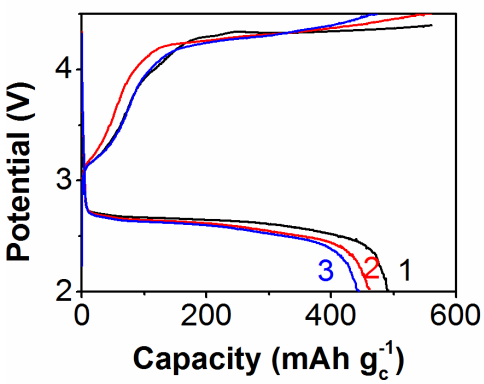

Figure SI.1. Charge-discharge plot SP@30% NiOCoO in the presence of O_2 at 50 mA g_c^{-1}.

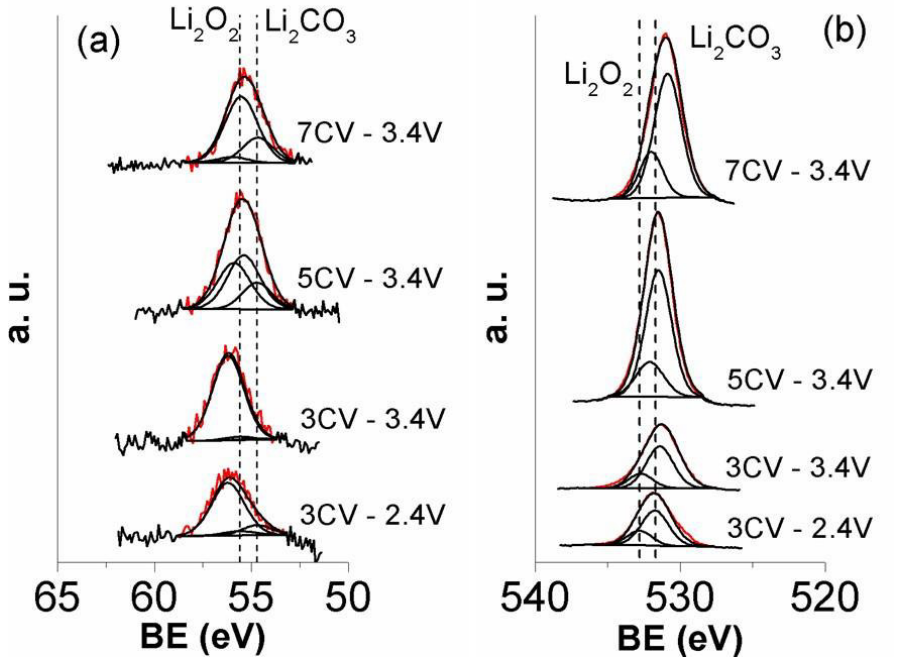

Figure SI.2. XPS spectrum of samples which were assayed with three, five or seven cyclic voltammetry and stopped at different potential in case of three CV. (a) Li-1s spectrum (b) O-1s spectrum.

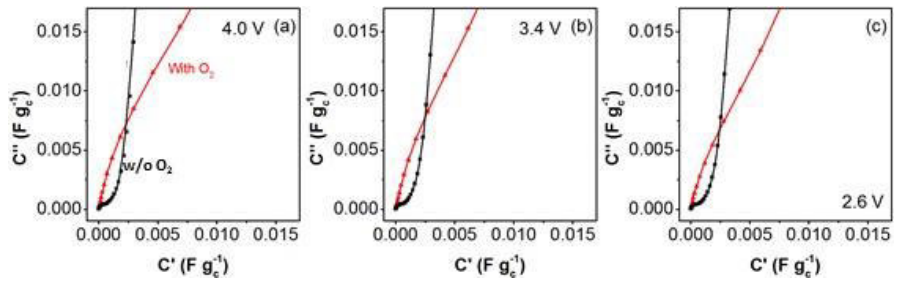

Figure SI.3. Capacities of SP@30% NiOCoO with (red triangles) and without (black squares) O_2. The experimental data are represented by solid symbols and the lines are obtained by the fitting with the equivalent circuit model shown in Figure 4.b.

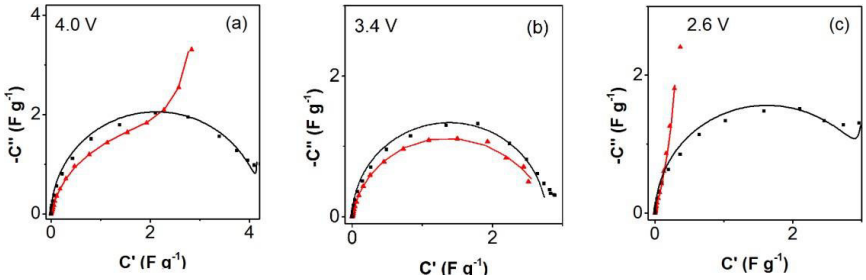

Figure SI. 4. Nyquist representation of SP with (red triangles) and without (black squares) O_2. The experimental data are represented by solid symbols and the lines are obtained by the fitting with the equivalent circuit model shown in Figure 4.b.

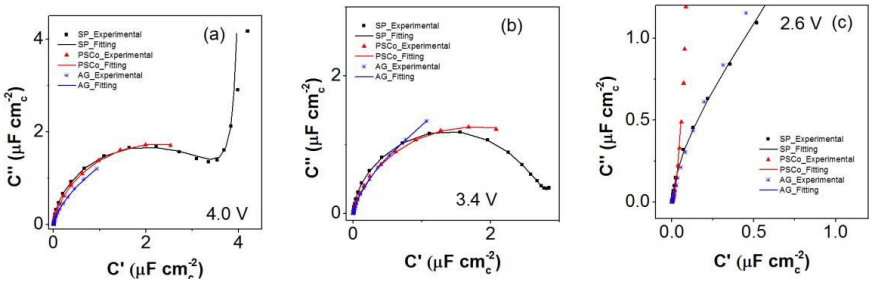

Figure SI. 5. Nyquist representation of three different carbons: SP (S_{BET} = 75 m^2 g^{-1}), AG (S_{BET} = 626 m^2 g^{-1}) and PSCo(S_{BET} = 1040 m^2 g^{-1}) with 15% of NiOCoO and in the presence of O_2. The experimental data are represented by solid symbols and the lines are obtained by the fitting with the equivalent circuit model shown in Figure 4.b. AG is an aerogel while PSCo is a carbon template synthesized. In this figure small differences are observed that can be ascribed to the different pore size distribution. PSCo has a well-defined mesoporosity while AG has a wide distribution of pore sizes.

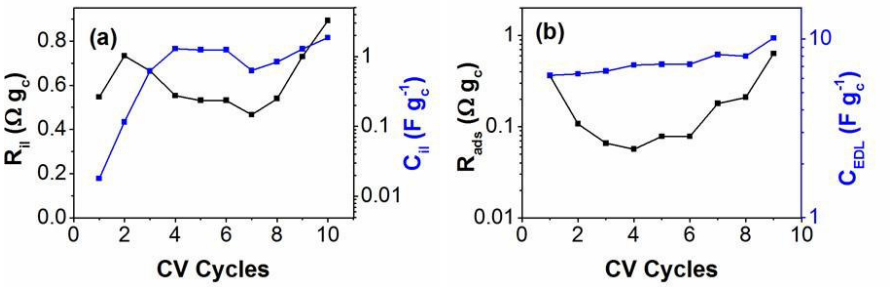

Figure SI.6. Fitting parameters of the EIS spectra registered at 3.4 V vs Li^{+}/Li upon cycling for the air cathode SP@30% NiOCoO: (a) resistance ($R_{il} = R_{i1} + R_{i2}$) and capacitance ($1/C_{il} = 1/C_{i1} + 1/C_{i2}$) at the electrode-electrolyte interface.

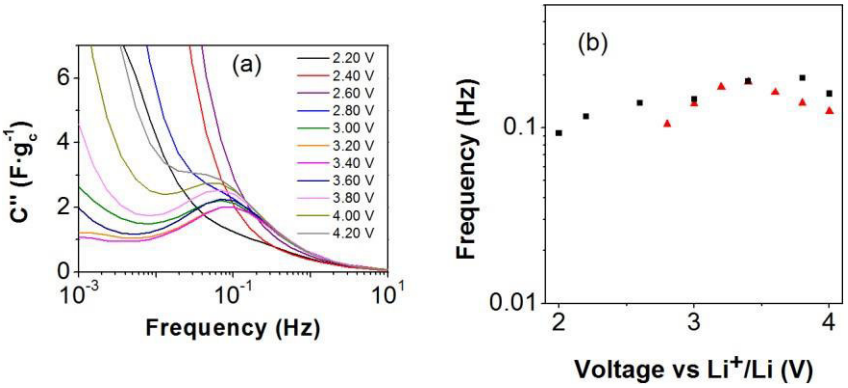

Figure SI.7. (a) C'' vs Frequency of SP@30% NiOCoO, where the peak related to EDLC is observe at 0.1 Hz. (b) Fitting values of the frequency obtained by the model Figure 4.b, where it is observed the good match with the experimental data.

Subcircuit related to EDL

This capacitance is associated to an arc in the C'' vs C' representation that can be modeled by a RC serie circuit, which product ($R \cdot C$) gives the characteristic time, c, of the process [1]. The resistance is represented by a constant phase circuit element (CPEads) in which has the value between 0 and 0.2 [1, 2]

Catalyst activity

The decomposition of Li_2O_2 ($Li_2O_2 \rightarrow 2Li + O_2$) can be studied if it is correlated with the decomposition reaction of diluted hydrogen peroxide aqueous solution ($H_2O_2 \rightarrow H_2O + ½\ O_2$).[3] This allows us to study quickly, qualitative/quantitative, the ability of catalyst to perform the expected reaction during charge process in batteries.

According to Giordani's experimental conditions we evaluated the NiOCoO catalyst activity: 25 mg of nanopowder were introduced into three-necked glass vessel containing 40 mL H_2O and it was sealed and purged with Ar. The outlet gas was analyzed by a chromatographAgilent Technologies AG-490 (with thermal conductivitydetector (μTCD) together with a narrow-bore column) to measure the volume of oxygen that was generated. The suspension was maintained under vigorous stirring and carry out at 25 ºC.

First, knowing the no-oxygen is present in the system, we inject H_2O_2 to achieve a concentration of 0.1 mol/L aqueous solution of H_2O_2 (Sigma Aldrich, d = 1.135, 30% in water), and immediately were taking data as a function of time to assess the reaction progress. In our experimental conditions 45.6 mL is maximum volume which could be get with initial H_2O_2 amount. Fig 8 shows the amount of O_2 released as a function of time for NiOCoO and compared to the carbon matrix, SP.Due to the good activity of this nanostructured oxide material regards H_2O_2 degradation, we decided to use NiOCoO as catalyst in the current study.

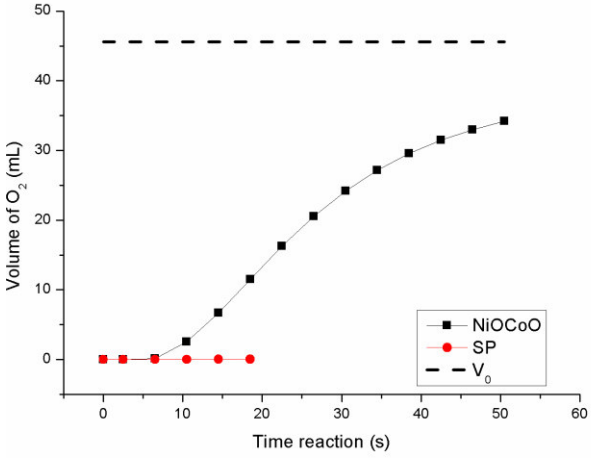

Figure SI.8. O2 evolution in the H_2O_2 degradation study in the presence of NiOCoO and the pristine carbon, SP.

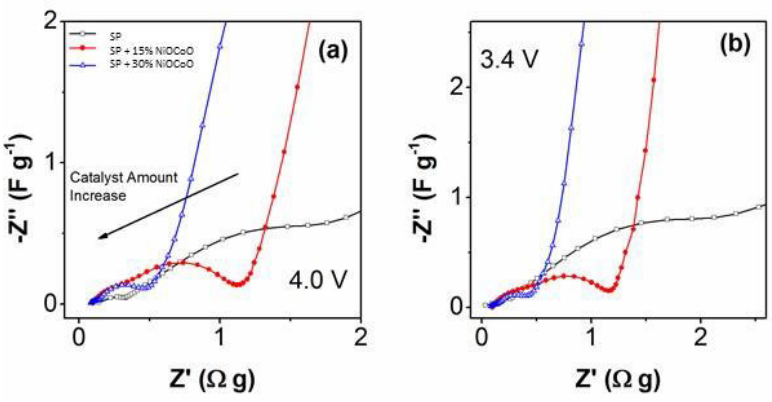

Figure SI.9.a, b) Nyquist plots in the region of high frequency of three electrodes with different amount of catalyst: SP (without catalyst), SP with 15% of NiOCoO and SP with 30 % of NiOCoO. It is observed that the second arc related to the charge transference decreases with the amount of catalyst. In this case, the normalization was performed to the electrode mass (carbon+catalyst) in place of the SP carbon mass.

References

1. F. Martinez-Julian, A. Guerrero, M. Haro, J. Bisquert, D. Bresser, E. Paillard, S. Passerini, G. Garcia-Belmonte, Probing lithiation kinetics of carbon-coated $ZnFe_2O_4$ nanoparticle battery anodes, The Journal of Physical Chemistry C, 118 (2014) 6069-6076.
2. M. Haro, T. Song, A. Guerrero, L. Bertoluzzi, J. Bisquert, U. Paik, G. Garcia-Belmonte, Germanium coating boosts lithium uptake in Si nanotube battery anodes, Physical Chemistry Chemical Physics, 16 (2014) 17930-17935.
3. V. Giordani, S. Freunberger, P. Bruce, J.-M. Tarascon, D. Larcher, H_2O_2 decomposition reaction as selecting tool for catalysts in Li–O_2 cells, Electrochemical and Solid-State Letters, 13 (2010) A180-A183.

5

Publication 3

5.1. Candidate's contribution

In this case of Publication 3, the nature and extent of my contribution to the work was the following:

Nature of contribution	Extent of contribution
• Review of existint literatura • Design experiments. Analysis and discussion the experimental data • Development and discussion the validity the impedance model • Write the manuscrit drafts. • Edit the manuscrit in accordance with the comments provided by co-author	80 %

5.2. Published manuscript

Nuria Vicente, Germà Garcia-Belmonte. Methylammonium lead bromide perovskite battery anodes reversibly host high Li-ion concentration, *The Journal of Physical Chemistry Letters*, **2017**, 8 (7), 1371-1374.

Methylammonium Lead Bromide Perovskite Battery Anodes Reversibly Host High Li-ion Concentrations

Nuria Vicente and Germà Garcia-Belmonte*

Institute of Advanced Materials (INAM), Universitat Jaume I, 12006 Castelló, Spain Corresponding author's e-mail: garciag@uji.es (G. G.-B)

Abstract

Ions migrate through the hybrid halide perovskite lattice allowing for a variety of electrochemical applications as perovskite-based electrodes for batteries. It is still unknown how extrinsic defects as lithium-ions interact with the hybrid perovskite structure during the charging process. It is shown here that Li^+ intake/release proceeds by topotactic insertion into the hybrid perovskite host, without drastic structural alterations or rearrangement. Even the perovskite electronic band structure remains basically unaltered upon cycling. The occurrence of conversion or alloying reactions producing metallic lead is discarded. Stable specific capacity ≈200 mA h g^{-1} is delivered which entails outstanding Li-ion concentration, x in $Li_xCH_3NH_3PbBr_3$, approaching 3. Slight distortions of the perovskite lattice upon cycling explain the highly-reversible Li^+ intercalation reaction that also exhibits an excellent rate capability.

TOC figure

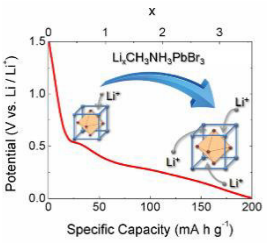

Hybrid perovskites have emerged as a family of multifunctional materials with applications in photovoltaics,[1-2] optoelectronics,[3-5] lasers,[6-7] and electrochromism.[8] Besides the interesting electronic and photonic properties exhibited by hybrid perovskites, ionic migration allows for a variety of application in electrochemical devices. Ion transport within the lattice of perovskite compounds have applications in solid-oxide fuel cells and oxygen permeation membranes.[9-10] It is also known that hybrid perovskites behave as charge storage materials for lithium-ion battery anodes.[11] In addition, native defects in hybrid lead halide perovskite materials are able to migrate within the perovskite structure because of the soft character of the compounds.[12] Despite the relevance extrinsic ion reaction with hybrids perovskites might have on their potential use in electrochemical devices, only a few works have addressed that issue.[11] How lithium-ions interact with the hybrid perovskite structure during the charging process is still an open question.[13] It is revealed here that perovskite-based electrodes exhibit high stability upon electrochemical cycling without severe distortions of the crystal structure. This fact indicates a topotactic intercalation for Li^+ storage into the perovskite host, without drastic structural alterations or rearrangement. Lithiation proceeds in such a way that several Li-ions are hosted within the same unit cell of the crystal lattice ($Li_xCH_3NH_3PbBr_3$) with x approaching 3. Moreover, the occurrence of conversion or alloying reactions producing metallic lead can be discarded.

In the present work, the hybrid perovskite $CH_3NH_3PbBr_3$ has been utilized as active material for the anode electrodes. Its interest in energy storage is related to their 3D framework of corner-connected MX_6 (M = Pb, X = Br) octahedrons with organic methylammonium cations located between them (Figure 1d). The hybrid halide perovskite AMX_3 can be then regarded as a compact structure in which the dimensionality of Li^+ transport is 3D, similarly to that occurring for spinels such as $LiMn_2O_4$ in contrast to low-dimension

insertion compounds. We present here promising preliminary results and progress into the understanding of the electrochemical charging of nanostructured lead halide perovskite materials, which exhibit rather stable specific capacity ≈200 mA h g^{-1} with an excellent reversibility. Rate capability between 1 C and 0.25 C charging rates does not significantly change, enabling for high-power performance. Although exhibiting similar electrochemical response, the issue of the underlying intercalation mechanism is not addressed by the previous works on perovskite-based anodes.[11]

Starting material were synthesized by slow evaporation of N, N-dimethylformamide (DMF, Sigma-Aldrich) in a solution containing stoichiometric amounts of lead bromide ($PbBr_2$, TCI) and methylammonium bromide (CH_3NH_3Br, >98% TCI) 1M in DMF. First $PbBr_2$ and CH_3NH_3Br were dissolved in DMF, and then the solution was heat up 90 ºC in magnetic stirring in a close bottle for 12 hours. Solid precipitated is orange color at the end of the reaction. The solution was stirred with a spatula to ensure the evaporation process of trapped solvent. Finally, it was taken out and cooled down to room temperature naturally. XRD to confirm the pure perovskite crystallographic were measured using Bruker AXS-D4 Endeavor Advance X-ray diffractometer using Cu Kα, wavelength λ=1.5406 Å.

To fabricate the working electrode, the homogeneous slurry was prepared by mixing $CH_3NH_3PbBr_3$, conductive carbon black (Super P) and poly(vinylidenedifluoride) binder (PVDF, Sigma-Aldrich) with an 80:10:10 weight ratio, respectively, by using N- methyl-2-pyrrolidone (NMP) as solvent. The slurry was coated on a copper foil by doctor blade and dried at 100ºC overnight. Composite electrodes slices with a diameter of 10 mm were cut and used as working electrodes for structural investigation and electrochemical analysis.

To investigate the lithium storage performance of the anode under study, a two- electrode Swagelok cell-type was used. Li metal foil was used as the counter and reference electrode and an electrolyte-soaked,

microporous monolayer membrane (Celgard 2500) was employed as separator. The electrolyte is 1M of hexafluorophosphate lithium slat (LiPF6, Sigma-Aldrich) dissolved in ethylene carbonate, ethyl-methyl carbonate and dimethyl carbonate (EC:EMC:DMC, Sigma- Aldrich) with 1:1:1 v/v. Cell assembly was carried out in a N2 filled glovebox. For electrochemical characterization, a PGSTAT-30 potentiostat from AUTOLAB equipped with an impedance module was employed. Cyclic voltammetry (CV) was performed in the voltage range from 0.01 to 2.00V with a rate of 5 mV s^{-1}. The constant current charge and discharge profiles of the battery in the voltage range from 0.01 V to 1.80 V at different rates of 50, 100 and 200 mA g^{-1}. All the data are normalized to the load $CH_3NH_3PbBr_3$ mass.

It is shown in Figure 1a XRD patterns of $CH_3NH_3PbBr_3$ powders fabricated by means of the procedure previously described. It can be indexed as a cubic perovskite structure with a =5.9394 Å (space group = Pm-3m). Diffraction peaks are assigned similarly to those appearing in previous publications.[16] It is shown in Figure 1S (Supporting Information) how diffraction peak positions remain unaltered upon lithiation- delithiation, which informs on the integrity of the structure. Recent XRD analyses on $CsPbBr_3$ films after electrochemical doping reveal slight increase of the lattice constant as a consequence of lithiation, signaling negligible structural variations.[8] Figure 1b and Figure 1c show SEM images of pristine $CH_3NH_3PbBr_3$ anodes. Most particles are regular and uniform with average size around 65 nm. Electrode surface is uniform although some pinholes are observed within which secondary particle agglomeration occurs. It is noted here that our synthesis produces nanometer-sized particles different from those reported in previous work,[11] which shows the formation of large micrometer- sized structures by hydrothermal methods.

With the aim of investigating the chemical stability of the lead bromide perovskite upon cycling, a detailed ex-situ XPS analysis at different charging states during the first charge-discharge cycle is

shown in Figure 1e and Figure 1f. Samples were washed out by anhydrous dimethyl carbonate (DMC) solvent several times, and dried in a vacuum chamber at 60°C for 2 h previous XPS analysis.[14] Here two elements are analyzed: bromine and lead. XPS spectra for different samples were studied using a C peak at 285.0 eV as reference, which allows identifying the valence states of the elements in pristine and cycled electrodes. In all studied electrodes, the XPS spectrum of lead appears as Pb^{+2} (Pb 4f) in Figure 1e, and exhibits two peaks attributed to Pb 4f7/2 and Pb 4f5/2 levels at binding energies (BE) of 138.7 eV and 143.6 eV, respectively. This is in full agreement to values reported previously.[15-16] In no case it is observed any signal corresponding to metallic lead (Pb^0). A recent analysis on $CsPbBr_3$ large single crystals has detected the presence of Pb^0 by electrochemical lithiation but using much wider (-5 V<V<5 V) potential windows.[8] Our results also indicate that Pb does not react to form any kind of Li-Pb alloy. It should be noted that the increase in binding energy of the Pb 4f lines (0.3 eV) upon discharge is hardly attributed to a change in the Pb oxidation state. After delithiation, XPS peaks recover in part the initial position. Small shifts can be related to a redistribution of bond electron charges.[17] It has been recently reported that ionic accumulation in perovskite compounds produces reversible lattice swell/shrink of approximately 4.4%.[18] It is then not surprising that Pb bonds will undergo slight variations upon Li^+ intake and release.

Spectra of Br 3p shows the Br 3p3/2 level that has a binding energy of 182.4 eV and Br 3p1/2 level of 189.1 eV (Figure 1f), similar to those observed earlier. Analysis of C 1s spectra present two peaks (see Figure 2S, Supporting Information), at 285.0 eV and 290.0 eV, respectively. The peak at higher energy can be assigned to Li_2CO_3 residuals, which could be formed because of electrolyte decomposition upon cycling. Finally, in the case of O 1s, the XPS bands appear at 531.8 eV and 532.9 eV, which is consistent with the presence of Li_2CO_3 as a cycling byproduct. Consequently, our analysis clearly

confirms the stable presence $CH_3NH_3PbBr_3$ after electrochemical cycling, indicating that successive lithium-ion intake and release does not cause severe distortions into the perovskite crystallographic structure. Moreover, also the electronic structure remains basically unaltered. It is already known that $[PbBr_6]^{4-}$ clusters largely dictate the electronic structure near the band edge.[19] Our findings point to the permanent presence of $PbBr_6$ building blocks upon lithiation and, consequently, continuity of the basic band structure. A detailed analysis of the band positions at different intercalation states would help us on this concern.[20] Electronic changes affecting the A-site organic cation cannot be discarded. These last facts signal the occurrence of a topotactic Li^+ insertion into the perovskite lattice, without severe alterations of crystal or main band structure, and unlikely occurrence of conversion or alloying reactions.

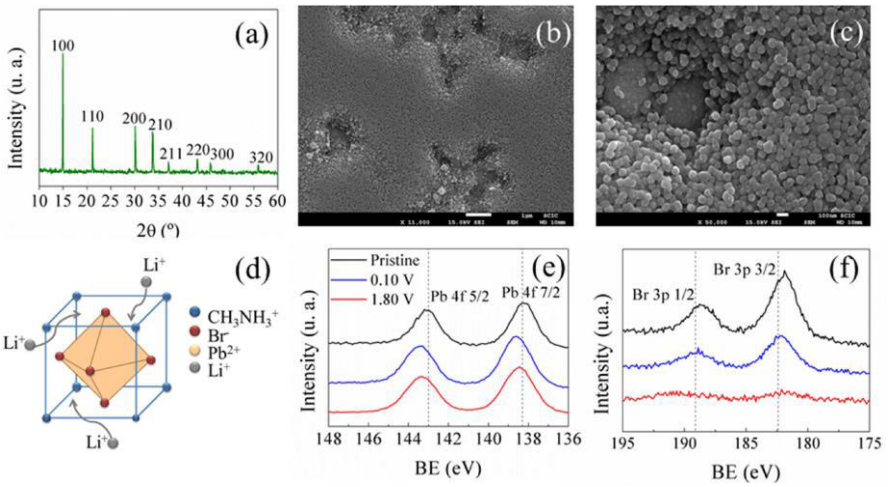

Figure 1. Structural analysis of lead bromide perovskite. (a) X–ray diffraction patterns of $CH_3NH_3PbBr_3$ powder, which can be indexed as cubic perovskite (space group = Pm-3m, a = 5.9394 Å. SEM morphology images of the $CH_3NH_3PbBr_3$ electrodes. Scale bar: (b) 1 µm; (c) 100 nm. Average perovskite particle size 65 nm. (d) Schematic crystal structure of organometal halide perovskite $CH_3NH_3PbBr_3$

indicating multiple Li-ion intake (e) Pb 4f and (f) Br 3d core level XPS signal of $CH_3NH_3PbBr_3$ anodes at different states: pristine, 0.10 V (discharge), and 1.80 V (subsequent charge).

For testing electrochemical response, perovskite-based anodes were monitored by cyclic voltammetry. Figure 2a shows the first four cycles that do not change significantly through continuous cycling. It confirms the good reversibility of the electrode material. The redox peaks related to Li^+ insertion is observed at 0.49 V and 0.27 V vs. Li/Li^+, and the extraction from the matrix produces two peaks in the delithiation current at 0.65 V and 0.75 V vs. Li/Li^+. The width of the peaks and the separation between them are related to the kinetic limitations (resistances) present in the electrode. The anodic and cathodic peaks relate to the charge-discharge voltage plateaus in the galvanostatic profiles (Figure 2c). As inferred from previous XPS analysis, ion intake proceeds without severe structural changes and explains the observed redox response. In order to check if the lead precursor shows electrochemical activity, $PbBr_2$ electrodes are investigated to compare them with $CH_3NH_3PbBr_3$ electrodes (Figure 2a). As observed, the redox response does take place into the perovskite lattice and not within its precursors.

Galvanostatic charge-discharge test of electrodes within the voltage range 0.01 V to 1.80 V vs Li/Li^+ at different charging current rate of 50, 100 and 200 mA g^{-1} can be seen in Figure 2b. A gradual fading is seen during the first several cycles. The charge and discharge specific capacities situate around 200 mA h g^{-1}, with the Coulombic efficiency above 99 %, till around 20 cycles. These specific capacity values are higher than the theoretical capacity of commercial $Li_4Ti_5O_{12}$, 175.5 mA h g^{-1}. From known values of lattice constant (a=5.93 Å), density (3.83 g cm-3), and molecular weight (478.92 g mol-1) of $CH_3NH_3PbBr_3$,[21] one can readily estimate the reached Li concentration per unit cell, x in $Li_xCH_3NH_3PbBr_3$. As observed in Figure 2c, lithiation attains molar contents as high as x=3. This is

certainly an outstanding charging value in comparison to other intercalation compounds that signals multiple unit cell Li^+ intake. It is remarkable that the first voltage plateau at 0.5 V is reached for insertion concentrations approaching x=1 (Figure 2c). This can be interpreted in terms of a full charging, with each unit cell hosting one Li-ion, before subsequent multiple insertion. Provided the attained high Li^+ concentration, one can expect electronic density values approaching 1022 cm^{-3}. This is uncommon for intercalation compounds and might indicate the intrinsic ability of hybrid perovskites of holding huge amounts of conduction band electrons without changes of the electronic structure. Recent papers have pointed out the occurrence of electronic accumulation zones at perovskite interfaces, which also imply large electronic density values.[22]

Higher capacity is reached in the first discharge curve (~600 mA h g^{-1}), which presumably correspond to the formation of a solid electrolyte interface (SEI) layer. On the other hand, cyclability has been evaluated at 50 mA g^{-1} after initial 10 cycles (Figure 2c). Discharge profiles delivers specific capacities decreasing from ≈265 mA h g^{-1} to ≈165 mA h g^{-1}. After 10 days of relax, additional 15 cycles show diminution in specific capacity from 150 down to 100 mA h g^{-1} (Figure 2c). As observed in Figure 2b the rate capability does not significantly change for cycling performed between 1C and 0.25C rate charging currents (assuming 1C equaling 200 mA g^{-1}). This fact signals the occurrence of fast Li^+ intake and release presumably produced by a large value of the ionic diffusion coefficient in the lead bromide perovskite lattice.

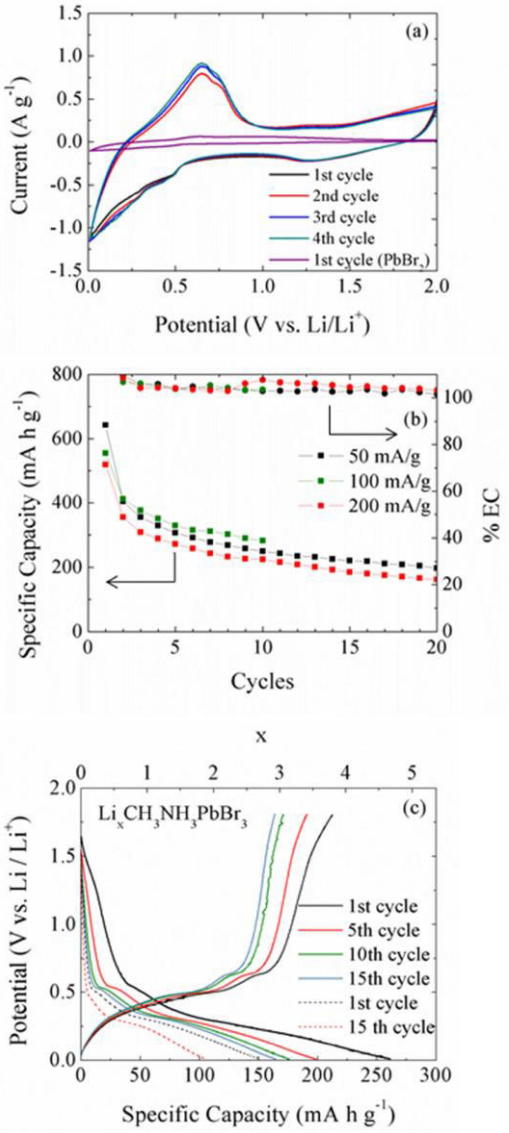

Figure 2. Battery electrochemical characterization. (a) Comparative cyclic voltammograms of $CH_3NH_3PbBr_3$ electrodes for the first four cycles in comparison to $PbBr^2$ electrode. (b) Specific capacity and Coulombic efficiency of $CH_3NH_3PbBr_3$ anodes corresponding to initial 20 cycles at different charging current densities: 50, 100 and 200 mA g^{-1}. (c) Discharge/charge voltage profiles as a function of specific capacity and corresponding Li-ion content after 10 initial cycles (continuous lines), and after 10 days relax performing additional 15 cycles (dashed line).

In summary, $CH_3NH_3PbBr_3$ is reported to be a promising anode material. Reversible Li^+ storage occurs by ion intercalation into the host electrode without severe distortion of the $CH_3NH_3PbBr_3$ lattice. Even the basic band structure remains basically unaltered for the potential window of interest. Long-term specific capacity attains significant values approaching 200 mA h g^{-1}. Lithiation reaches molar contents as high as x=3 (moles of lithium per mole of methylammonium), an outstanding value in comparison to other intercalation compounds. $CH_3NH_3PbBr_3$ gathers then two main advantages: (i) it allows for high insertion concentrations with x>>1, and simultaneously (ii) it exhibits small structural distortions (topotactic intercalation). Importantly, the rate capability does not exhibit significant reduction for charging currents between 1 C and 0.25 C, indicating the potentiality of perovskite-based materials for high power battery applications. Our findings reveal the outstanding electronic and ionic properties of lead halide perovskites, and their potential use as energy storage materials.

Associated Content

Supporting Information

Additional XPS spectra, and XRD analysis of lithiated and delithiated electrodes.

Author Information.

Corresponding author

*E-mail: garciag@uji.es ORCID

Nuria Vicente: 0000-0002-9823-7131

Germà Garcia-Belmonte: 0000-0002-0172-6175

Acknowledgments

We thank financial support by Generalitat Valenciana under Prometeo Project (PROMETEO/2014/020), and Ministerio de Economía y Competitividad (MINECO) of Spain under Project (MAT2016-76892-C3-1-R). N.V. acknowledges University Jaume I through FPI Fellowship Program (PREDOC/2015/54). SCIC from Universitat Jaume I is also acknowledged. The authors acknowledge Celgard for supplying separator membranes.

References

1. Kim, H.-S.; Lee, C.-R.; Im, J.-H.; Lee, K.-B.; Moehl, T.; Marchioro, A.; Moon, S.-J.; Humphry-Baker, R.; Yum, J.-H.; Moser, J. E.; et al. Lead Iodide Perovskite Sensitized All-Solid-State Submicron Thin Film Mesoscopic Solar Cell with Efficiency Exceeding 9%. Sci. Rep. 2012, 2, 591.
2. Liu, M.; Johnston, M. B.; Snaith, H. J. Efficient Planar Heterojunction Perovskite Solar Cells by Vapour Deposition. Nature 2013, 501, 395–398.
3. Dou , L.; Yang , Y.; You, J.; Hong, Z.; Chang, W.-H.; Li, G.; Yang, Y. Solution- processed Hybrid Perovskite Photodetectors with High Detectivity. Nat. Commun. 2014, 5, 5404.
4. Kim, Y.-H.; Cho, H.; Heo, J. H.; Kim, T.-S.; Myoung, N.; Lee, C.-L.; Im, S. H.; Lee, T.-W. Multicolored Organic/Inorganic Hybrid Perovskite Light-Emitting Diodes. Adv. Mater. 2015, 27, 1248.
5. Suárez, I.; Juárez-Pérez, E. J.; Bisquert , J.; Mora-Seró, I.; Martínez-Pastor, J. P. Polymer/Perovskite Amplifying Waveguides for Active Hybrid Silicon Photonics. Adv. Mater. 2015, 27, 6157–6162.
6. Deschler, F.; Price, M.; Pathak, S.; Klintberg, L. E.; Jarausch, D.-D.; Higler, R.; Hüttner, S.; Leijtens, T.; Stranks, S. D.; Snaith, H. J.; et al. High Photoluminescence Efficiency and

Optically Pumped Lasing in Solution-Processed Mixed Halide Perovskite Semiconductors. J. Phys. Chem. Lett. 2014, 5, 1421–1426.

7. Xing, G.; Mathews, N.; Lim, S. S.; Yantara, N.; Liu, X.; Sabba, D.; Gratzel, M.; Mhaisalkar, S.; Sum, T. C. Low-temperature Solution-processed Wavelength-tunable Perovskites for Lasing. Nat. Mater. 2014, 13, 476.
8. Jiang, Q.; Chen, M.; Li, J.; Wang, M.; Zeng, X.; Besara, T.; Lu, J.; Xin, Y.; Shan, X.; Pan, B.; et al. Electrochemical Doping of Halide Perovskites with Ion Intercalation. ACS Nano 2017, 11, 1073–1079.
9. Li, M.; Pietrowski, M. J.; De Souza, R. A.; Zhang, H.; Reaney, I. M.; Cook, S. N.; Kilner, J. A.; Sinclair, D. C. A Family of Oxide Ion Conductors Based on the Ferroelectric Perovskite $Na_{0.5}Bi_{0.5}TiO_3$. Nat. Mater. 2014, 13, 31–35.
10. Mizusaki, J.; Arai, K.; Fueki, K. Ionic Conduction of the Perovskite-type Halides. Solid State Ionics 1983, 11, 203-211.
11. Xia, H.-R.; Sun, W.-T.; Peng, L.-M. Hydrothermal Synthesis of Organometal Halide Perovskites for Li-ion Batteries. Chem. Comm. 2015, 51, 13787-13790.
12. Unge, E. L.; Hoke, E. T.; Bailie, C. D.; Nguyen, W. H.; Bowring, A. R.; Heumüller, T.; Christoforod, M. G.; McGehee, M. D. Hysteresis and Transient Behavior in Current–Voltage Measurements of Hybrid-Perovskite Absorber Solar Cells. Energy Environ. Sci. 2014, 7, 3690–3698.
13. Zhang, W.; Eperon, G. E.; Snaith, H. J. Metal Halide Perovskites for Energy Applications. Nat. Energy 2016, 1, 16048.
14. Haro, M.; Vicente, N.; Garcia-Belmonte, G. Oxygen Reduction Reaction Promotes Li^+ Desorption from Cathode Surface in Li-O_2 Batteries. Adv. Mater. Interfaces 2015, 2, 1500369.
15. Schmidt, L. C.; Pertegás, A.; González-Carrero, S.; Malinkiewicz, O.; Agouram, S.; Minguez Espallargas, G.;

Bolink, H. J.; Galian, R. E.; Pérez-Prieto, J. Nontemplate Synthesis of $CH_3NH_3PbBr_3$ Perovskite Nanoparticles. J. Am. Chem. Soc. 2014, 136, 850-853.

16. Lindblad, R.; Jena, N. K.; Philippe, B.; Oscarsson, J.; Bi, D.; Lindblad, A.; Mandal, S.; Pal, B.; Sarma, D. D.; Karis, O. Electronic Structure of $CH_3NH_3PbX_3$ Perovskites: Dependence on the Halide Moiety. J. Phys. Chem. C 2015, 119, 1818- 1825.
17. Momose, H.; Honbo, H.; Takeuchi, S.; Nishimura, K.; Horiba, T.; Muranaka, Y.; Kozono, Y.; Miyadera, H. X-ray Photoelectron Spectroscopy Analyses of Lithium Intercalation and Alloying Reactions on Graphite Electrodes. J. Power Sources 1997, 68, 208-211.
18. Zhang, Y.; Wang, Y.; Xu, Z.-Q.; Liu, J.; Song, J.; Xue, Y.; Wang, Z.; Zheng, J.; Jiang, L.; Zheng, C.; et al. Reversible Structural Swell−Shrink and Recoverable Optical Properties in Hybrid Inorganic−Organic Perovskite. ACS Nano 2016, 10, 7031−7038.
19. Manser, J. S.; Christians, J. A.; Kamat, P. V. Intriguing Optoelectronic Properties of Metal Halide Perovskites. Chem. Rev. 2016, 116, 12956−13008.
20. Miller, E. M.; Zhao, Y.; Mercado, C. C.; Saha, S. K.; Luther, J. M.; Zhu, K.; Stevanovic, V.; Perkins, C. L.; van de Lagemaat, J. Substrate-controlled band positions in $CH_3NH_3PbI_3$ perovskite films. Phys. Chem. Chem. Phys. 2014, 16, 22122.
21. Weber, D. $CH_3NH_3PbX_3$, a Pb(II)-System with Cubic Perovskite Structure. Z. Naturforsch. 1978, 33b, 1443-1445.
22. Zarazua, I.; Bisquert, J.; Garcia-Belmonte, G. Light-Induced Space-Charge Accumulation Zone as Photovoltaic Mechanism in Perovskite Solar Cells. J. Phys. Chem. Lett. 2016, 7, 525−528.

Supporting Information

Methylammonium Lead Bromide Perovskite Battery Anodes Reversibly Host High Li-ion Concentrations

Nuria Vicente and Germà Garcia-Belmonte*

Institute of Advanced Materials (INAM), Universitat Jaume I, 12006 Castelló, Spain

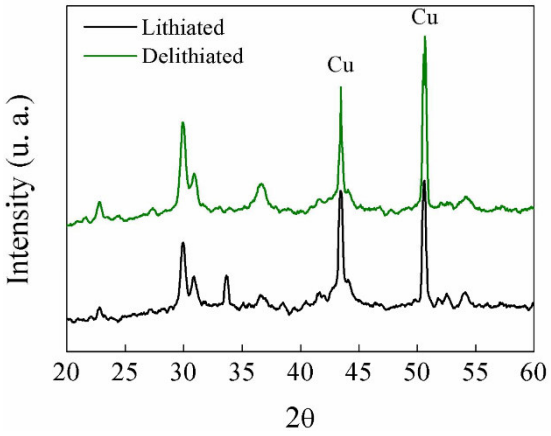

Figure 1S. XRD patterns at different states: lithiated electrode (0.1 V) and delithiated electrode (1.8 V), where the peak positions corresponding to $CH_3NH_3PbBr_3$ perovskite remain unaltered (2 position: 30.09°, 33.78°, 37.12° and 43.10º).

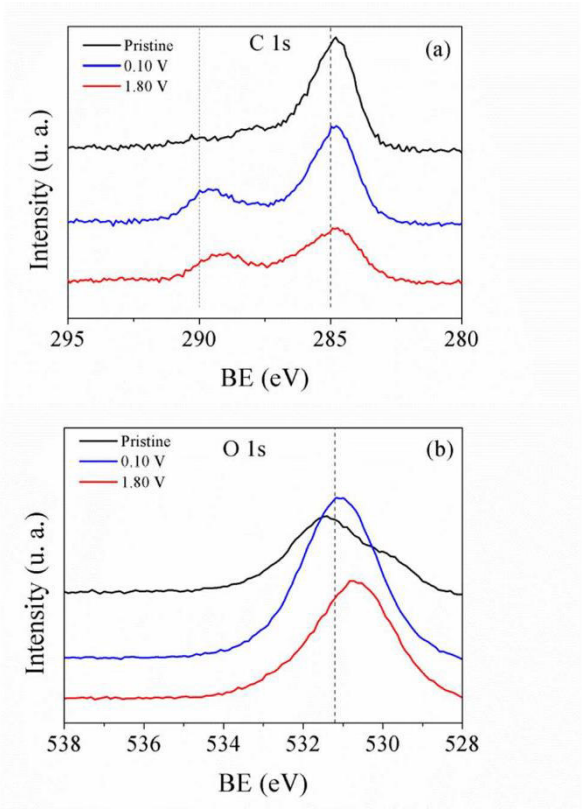

Figure 2S. (a) C1s and (b) O 1s core level XPS signal of $CH_3NH_3PbBr_3$ anodes at different states: pristine, 0.10 V (discharge), and 1.80 V (subsequent charge

6

Publication 4

6.1. Candidate's contribution

In this case of Publication 4, the nature and extent of my contribution to the work was the following:

Nature of contribution	Extent of contribution
• Review of existint literatura • Design experiments • Analysis and discussion the experimental data • Development the Impedance Model • Discussion validity of the model • Performance the impedance study • Write the manuscrit drafts. • Edit the manuscrit in accordance with the comments provided by co-author and referees.	80 %

6.2. Published manuscript

Nuria Vicente, Germà Garcia-Belmonte. Organohalide Perovskites are Fast Ionic Conductors, *Advanced Energy Materials*, **2017**, 7 (19), 1700710.

DOI: 10.1002/aenm.201700710

Article type: Communication

Organohalide Perovskites Are Fast Ionic Conductors

Nuria Vicente and Germà Garcia-Belmonte*

N. Vicente, Prof. G. Garcia-Belmonte

Institute of Advanced Materials (INAM), Universitat Jaume I, 12006 Castelló, Spain E-mail: garciag@uji.es

Keywords: perovskites, ion conduction, batteries, impedance, lithium-ion diffusion

Fast ionic conductors constitute a family of materials exhibiting high values of the ionic conductivity while their crystal structure remains rather rigid. Perovskite-like compounds are known to be good ionic conductors with applications as solid electrolytes. In hybrid halide perovskites both intrinsic (native) and extrinsic defect migration are regarded to occur. Ion diffusivity analysis is inherently ambiguous in all-solid-state configurations because of the multicomponent environment. Here a liquid electrolyte in contact to the perovskite material forms a reservoir of Li^+ that is forced to intercalate and migrate within the perovskite electrode. This approach decouples different contributions to transport in such a way that ion diffusion kinetics is easily accessible by means of impedance methods. Room-temperature chemical diffusion coefficient of lithium-ion within the perovskite lattice exhibits values as high as $D_{\mu} \sim 10^{-7}$ cm^2 s^{-1}, which implies conductivities within the range of 10^{-3} Ω^{-1} cm^{-1} for highly lithiated electrodes. This confirms the superionic intrinsic property of

organohalide perovskites from a direct and unambiguous measurement that does not rely upon simulation tools.

Fast ionic conductors (also known as superionic conductors) constitute a family of materials exhibiting high values of the ionic conductivity or diffusivity.[1, 2] Their principal feature is the ability to keep the crystal structure rather frozen while permitting the migration of ionic species. Fast ionic conductors are of particular interest for technological applications in the field of solid electrolytes for electrochemical devices such as batteries, supercapacitors, sensors, electrochromic windows, and ionic membranes for fuel cells. Typically ionic conductivity lies within the range of 10^{-4} - 10^{-1} Ω^{-1} cm^{-1} at room temperature to consider a material as superionic conductor. Some fast ionic conductors also exhibit prominent electronic conductivity and are known as mixed ionic-electronic conductors. Many perovskite-type oxides belong to this class of materials and have well-known applications in solid-oxide fuel cells and oxygen permeation membranes. [3, 4] Even halide perovskites of the type $CsPbX_3$ (X=Cl, Br) are also known to be good ionic conductors.[5] Native defects in hybrid lead halide perovskite materials are known to migrate within the perovskite lattice because of the soft character of the compounds. First-principles computational studies have identified facile migration of iodine anions through a vacancy-assisted mechanism, and also long-range displacement of the organic cation, although different calculated activation energies have been reported.[6-8] These simulations observe presence in equilibrium of several ionic vacancies and interstitials (I^-, Br^-, Pb^{2+} and CH_3NH^{3+}) at room temperature. Also extrinsic defects as hydrogen has been studied by First-principles.[9] However, there is no clear agreement concerning the ion diffusion time scale or the dominant ionic species. Whereas some studies have reported diffusivity values of native defects in organohalide perovskites of the order of those encountered in common solid state ionic conductors, D~10^{-12} cm^2 s^{-1}, [7, 10, 11] other analyses give much faster ion migration coeficients D~10^{-8} – 10^{-7} cm^2 s^{-1}.[12, 13] Despite

the recognized need for knowing about the kinetics of ion migration, the complex defect chemistry exhibited by organohalide perovskites makes it difficult discerning about specific mobile ion diffusivity.

Since determination of defect diffusivities in perovskite films is inherently complex, it is proposed here an approach that takes advantage of the intercalation and migration of extrinsic lithium ions into methylammonium lead bromide perovskite to unambiguously extract diffusivity values. Instead of working on all-solid-state configurations, a reservoir of Li^+ makes part of the liquid electrolyte in contact to the perovskite material. In this configuration (Figure 1a) Li^+ is forced to intercalate and migrate within the perovskite electrode in such a way that the ion diffusion kinetics is easily accessible by means of impedance methods. Provided the mixed conduction character of organohalide perovskites with very high electronic mobilities,[14] our approach decouples the electronic from the ionic transport thereby avoiding the intrinsic ambiguity of solid state methods. This is feasible because both electronic and ionic densities increase by the same amount upon intercalation, in such away that electronic conductivity always exceeds the ionic conductivity. It is the slowest charge carrier that determines the kinetics.

In the present work, the hybrid perovskite $CH_3NH_3PbBr_3$ has been utilized as active material for the anode electrode of lithium-ion half-battery set-up (Figure 1a). Easy Li^+ intercalation is related to the framework of corner-connected MX_6 (M = Pb, X = Br) octahedrons with organic methylammonium cations located between them.[15] The hybrid halide perovskite behaves as a compact structure in which the dimensionality of Li^+ transport is 3D similarly to that occurring for intercalation spinel compounds such as $LiMn_2O_4$. Moreover, perovskite electrodes allow checking ion diffusion dynamics of extrinsic defects (Li^+) in a fully controllable way. Hence, our strategy avoids the inherent uncertainty found in analyzing native defect migration in a multicomponent environment. It is observed that

room- temperature chemical diffusion coefficient of lithium-ion within the perovskite lattice exhibits values as high as D_{μ}~10^{-7} cm^2 s^{-1}, which implies ionic conductivities within the range of 10^{-3} Ω^{-1} cm^{-1} for highly lithiated electrodes. This confirms the fast ionic conductor character of hybrid perovskite materials from a direct and unambiguous measurement that does not rely upon simulation tools.

Perovskite-based electrodes are prepared as described in the Experimental Section and recently reported.[16] XRD analysis confirms the pure perovskite crystallographic phase (Figure 1b). Electrodes comprises $CH_3NH_3PbBr_3$ composed of 65 nm average size particles, conductive carbon black and poly(vinylidenedifluoride) binder (PVDF, Sigma-Aldrich), with a 80:10:10 weight ratio, deposited on Cu foils (Figure 1a). The use of carbon black assures a good electronic connection between Cu and the perovskite particles. The driving force for Li^+ transport relates to the ion chemical potential gradient $\Delta\mu$ that establishes the electrode potential as $eV = -[\mu(x) - \mu_{ref}]$, being e the positive elementary charge, x is the molar concentration in $Li_xCH_3NH_3PbBr_3$, and refers to the Li-metal electrode potential reference. For testing electrochemical response, perovskite-based anodes were monitored by cyclic voltammetry (see Experimental Section for details). Figure 1c shows stable signal that does not change significantly through continuous cycling.[16] It confirms a good reversibility for the electrode material. The reaction peaks related to Li^+ insertion are observed at 0.49 V and 0.27 V vs. Li/Li^+, and the Li^+ extraction from the matrix produces two peaks in the delithiation current at 0.65 V and 0.75 V vs. Li/Li^+. Contrary to that occurring for conducting polymer[17] or redox molecule modified electrodes,[18] in which the energy landscape of electronic states dictate the electrochemical response, perovskite-based anodes are driven by the ionic energetics. As recently reported, $CH_3NH_3PbBr_3$ electrodes exhibit a highly reversible lithium uptake and release without severe distortion of the perovskite lattice (topotactic intercalation). Even the basic band structure remains basically unaltered for the

potential window of interest.[16] As observed in Figure 1c, electrodes comprising perovskite precursors ($PbBr_2$) have no electrochemical activity in comparison to perovskite-based electrodes. Hence, the electrochemical set-up used here constitutes an excellent approach to investigate ion diffusion through the perovskite lattice.

Electrochemical impedance spectroscopy (EIS) analysis is performed potentiostatically at different charge states after the first cycles, for discharging (lithiation) steps of 50 mC. Galvanostatic lithiation profile of electrodes within the voltage range 1.80 V to 0.01 V vs Li/Li^+ during EIS measurements is shown in Figure 2a. See recent report on charge/discharge curves and rate capability.[16] The impedance plots in Figure 2b consist of three well-defined parts: the high-frequency semicircle related to electrode/electrolyte processes, the middle frequency diffusion pattern, and an inclined low-frequency line in response to the electrochemical charging. The impedance spectra could be modeled by means of a well-known Randles' equivalent circuit as shown in inset of Figure 2a. The equivalent circuit includes a parallel subcircuit of R_{ct} and C_{dl} that accounts for the polarization charge-transfer resistance and the double-layer capacitance associated to the electrode/electrolyte interface. At high frequencies, a rather voltage- and electrode thickness-independent arc is found with C_{dl} 2.8 mF g^{-1} (C_{dl} = 10 µF cm^{-2}; see Figure S1) and R_{ct} = 0.14 Ω g (R_{ct} = 20.16 Ω cm^2).

These trends and values allow readily connecting them to mechanisms occurring at the outer electrode/electrolyte interface. In addition, series resistance accounts for the ohmic resistance R_s = 0.04 Ω g (R_s = 5.6 Ω cm^2).

The intermediate- and low-frequency impedance response points to a diffusive-capacitive behavior that depends on the voltage (charge) state. This performance informs on the electrode ability of varying its capacity because of the intercalation of Li^+ inside perovskite structure. By examining this behavior, it is possible to know how fast

ions can be inserted into or withdrawn (extracted) from a rather stable host crystal lattice. The impedance model used here corresponds to the classical spatially restricted diffusion element, which exhibits the so-called anomalous diffusion response, Z_D in the inset of Figure 2a.[19] This scheme assumes large enough electronic conductivity so as to render Li^+ diffusion as determining parameter of the charging process. This is expected to be the case provided the high electronic mobility reported for solar perovskite materials.[14] Diffusion impedances undergo a pattern change at a certain characteristic frequency ω_d at which a transition between a Warburg- to a capacitive- like behavior is observed.[20, 21] The frequency ω_d is located near the elbow of the impedance plot, as marked in Figure 2b, and relates to the chemical diffusion coefficient D_μ as

$$\omega_d = \frac{D_\mu}{L^2} \quad (1)$$

Here L accounts for the thickness of the electrode. The finite-length diffusion element is given by

$$Z_D = R_d \left(\frac{i\omega}{\omega_d}\right)^{-\gamma/2} coth\left[\left(\frac{i\omega}{\omega_d}\right)^{-\gamma/2}\right] \quad (2)$$

Being ω the angular frequency, and $i = \sqrt{-1}$. R_d is the resistance associated with the ionic diffusion, and γ relates to the deviation from the ideal spatially restricted diffusion impedance ($\gamma = 1$). The anomalous diffusion mechanism ($\gamma < 1$) is expected to occur in a multiphasic matrix.[22] Models based on spatially-restricted ion diffusion were proposed to account for intermediate-frequency distortions relaying on a distribution of diffusion lengths,[23] or electronic transport limitations.[24] Diffusion of ions gives rise to distinctive impedance paterns characterized by Warburg-like responses as $Z \propto (iw)^{-\gamma/2}$ at intermediate frequencies. At lower frequencies the electrode charging is manifested in the capacitive response of the impedance through the chemical capacitance $C_\mu =$

$e^2Ndx/d\mu$ element, being N the total density of intercalation ion sites in the perovskite lattice. It is related to the characteristic frequency as

$$\omega_d = \frac{1}{R_d C_\mu} \quad (3)$$

By fitting the equivalent circuit in the inset of Figure 2a to the impedance data in Figure 2b for different voltage stages during discharge process, it is found that the diffusion resistance decreases with voltage, from 0.18 Ω g at 1.20 V down to 0.08 Ω g at 0.30 V. It is also checked for consistency that the chemical capacitance extracted from impedance and that derived from cyclic voltammetry as $C\mu = -dQ / dV$ yields similar values (Figure 2c), with a voltage shift in the peak position related to kinetic limitations in the case of large-amplitude, out-of-equilibrium techniques as cyclic voltammetry at usual scan rates.

Some caution words are in order here about the applicability of the previously outlined diffusion model. The extraction of the chemical diffusion coeficient D_μ using Equation 1 relays on a proper determination of the diffusion length that, in certain experimental conditions, does not coincide with the electrode thickness L . If the electrolyte penetrates the electrode and wets the active particles the effective diffusion length in the solid-state may be significantly reduced $L_{eff} <<< L$, giving rise to large overestimations in D_μ. The so-called porous impedance model allows addressing these last cases.[23-25] Hence, it is a matter of experimental check to discern if $L_{eff} \sim L$, in such a way that the finite-length diffusion mechanism in Equation 2 can be exploited to determine D_μ. Here electrodes with diferent thickness, by varying the weight of the active material, have been tested by impedance.

As the perovskite lithiation progresses, specific capacity values as high as 400 mA h g^{-1} are reached (Figure 2a), which implies a Li-ion

concentration as high as 1021 cm^{-3}, given perovskite densities approximately equal to 4.16 g cm^{-3}. The host matrix becomes fully lithiated at potentials below 0.5 V, as discussed very recently.[16] It is worth determining the chemical diffusion coefficient in Equation 1, where the diffusion characteristic frequency is extracted from long-range Li^+ displacements corresponding to the thickness of the electrode.

The variation of the diffusion characteristic frequency ω_d with voltage is shown in Figure 3a. One can observe that ω_d appears to be rather voltage-independent but exhibits a clear correlation with the electrode thickness in agreement with Equation 1. A close examination of the average values of d as a function of L allows verifying the validity of our approach (Figure 3b). Here it has been checked that fitting the expression $\omega_d = \frac{D_\mu}{L^n}$ yields a value for the thickness coefficient equaling $n = 2.8 \pm 0.6$. This agrees with the thickness dependence predicted by Equation 1 as n=2 within the experimental error. This observation allows extracting $D_\mu = (2.8 \pm 1.0) \cdot 10^{-7}$ cm^2 s^{-1} given the strong correlation between ω_d and the electrode thickness. An additional point reinforcing that $L_{eff} \approx L$ is the elEctrode thickness-independent trend exhibited by the double-layer capacitance. As shown in Figure S1, C_{dl} is always situated around typical values in the order of μF cm^{-2}, not correlated with L at all. This is in contradiction with that derived from the porous electrode model in which the electrolyte/electrode interface is extended within the matrix producing double-layer capacitances largely exceeding μF cm^{-2} values.[26] Moreover, one would expect strong correlations between C_{dl} and the electrode thickness for the porous electrode model. These trends have neither been observed in our samples.

Diffusivity attains rather voltage-independent values in the range of $D_\mu \sim 10^{-7}$ cm^2 s^{-1}. This high lithium diffusivity corresponds to conductivities within the range of 10^{-3} Ω^{-1} cm^{-1} for highly lithiated

electrodes. It is checked here that the procedure to determine the chemical diffusion coefficient is consistent with the electrode thickness variation. This fact allows us to discard relating dto the perovskite particle size (65 nm) and verifies the proposed diffusion model in Equation 2 in which L equals the thickness of the host matrix.

To sum up, our findings unambiguously show that lead halide perovskites can be regarded as fast ionic conductors with large diffusion coefficients. The approach followed here, using an electrolyte/electrode contact, allows decoupling electronic from ionic transport. This avoids the inherent ambiguity of all-solid-state experimental techniques. Room-temperature chemical diffusion coefficient of Li^+ within the perovskite lattice exhibits values as high as $D\mu \sim 10^{-7}$ cm^2 s^{-1}, which implies conductivities within the range of 10^{-3} Ω^{-1} cm^{-1} for highly lithiated electrodes. The proved superionic intrinsic property of organohalide perovskites opens new room for devising applications and devices in which fast ionic migration is an essential requirement.

Experimental Section

Perovskite material were synthesized by slow evaporation of N, N-dimethylformamide (DMF, Sigma-Aldrich) in a solution containing stoichiometric amounts of lead bromide ($PbBr_2$, TCI) and methylammonium bromide (CH_3NH_3Br, >98% TCI) 1M in DMF, as recently reported.[16] Solid precipitated becomes orange at the end of the reaction. Bruker AXS-D4 Endeavor Advance X-ray diffractometer using Cu Kα, wavelength λ=1.5406 Å, is employed in XRD to confirm the pure perovskite crystallographic structure.

The working anode electrode (Figure 1a) was prepared by mixing $CH_3NH_3PbBr_3$ composed of 65 nm average size particles, conductive carbon black and poly(vinylidenedifluoride) binder (PVDF, Sigma-Aldrich) with a 80:10:10 weight ratio, and N-methyl-2-pyrrolidone

(NMP) as solvent.[16] Also the blank electrode comprising $PbBr_2$ contains the same weight ratio (80:10:10). The slurry was coated on a copper foil by Dr. Blade and dried at 100ºC overnight. Working electrodes for electrochemical analysis were made up of composite material slices with a diameter of 10 mm using Swagelok-type cells. Li metal foil was used as the counter and reference electrode (Figure 1a), and an electrolyte-soaked, microporous monolayer membrane (Celgard 2500) is employed as separator. The electrolyte is 1M of hexafluorophosphate lithium salt ($LiPF_6$, Sigma-Aldrich) dissolved in ethylene carbonate, ethyl-methyl carbonate and dimethyl carbonate (EC:EMC:DMC, Sigma-Aldrich) with 1:1:1 v/v. Cell assembly was carried out in an N2 filled glovebox. For electrochemical characterization, a PGSTAT-30 potentiostat from AUTOLAB equipped with an impedance module was employed. Cyclic voltammetry (CV) was performed in the voltage range from 0.01 to 2.00 V with a rate of 5 mV s^{-1}. After the first cycle, in the second discharge electrochemical impedance (EIS) test was carried out potentiostatically every 50 mC of discharge (Figure 2a), with an amplitude perturbation of 10 mV in the frequency range of 1 MHz to 10 mHz. The approximation to the different measuring voltages was galvanostatically controlled at 50 mA g^{-1} to assure the quasi-equilibrium state of the electrode. All the data are normalized to the load $CH_3NH_3PbBr_3$ mass.

Supporting Information

Supporting Information is available from the Wiley Online Library or from the author.

Acknowledgements

We thank financial support by Generalitat Valenciana under Prometeo Project (PROMETEO/2014/020), and Ministerio de

Economía y Competitividad (MINECO) of Spain under Project (MAT2016-76892-C3-1-R). N.V. acknowledges University Jaume I through FPI Fellowship Program (PREDOC/2015/54) and Project (UJI-B2016-35). SCIC from Universitat Jaume I is also acknowledged. The authors acknowledge Celgard for supplying separator membranes.

Received: ((will be filled in by the editorial staff))
Revised: ((will be filled in by the editorial staff))
Published online: ((will be filled in by the editorial staff))

References

1. H. L. Tuller, P. K. Moon, Materials Science and Engineering: B 1988, 1, 171.
2. S. Adams, J. Swenson, Phys. Rev. Lett. 2000, 84, 4144.
3. M. Li, M. J. Pietrowski, R. A. De Souza, H. Zhang, I. M. Reaney, S. N. Cook, J. A. Kilner, D. C. Sinclair, Nat. Mater. 2014, 13, 31.
4. H. Hayashi, H. Inaba, M. Matsuyama, N. G. Lan, DokiyaM. , H. Tagawa, Solid State Ionics 1999, 122, 1.
5. J. Mizusaki, K. Arai, K. Fueki, Solid State Ionics 1983, 11, 203.
6. J. M. Azpiroz, E. Mosconi, J. Bisquert, F. De Angelis, Energy Environ. Sci. 2015, 8, 2118.
7. C. Eames, J. M. Frost, P. R. F. Barnes, B. C. O'Regan, A. Walsh, M. S. Islam, Nat. Commun. 2015, 6, 7497.
8. J. Haruyama, K. Sodeyama, L. Han, Y. Tateyama, J. Am. Chem. Soc. 2015, 137, 10048−10051.
9. D. A. Egger, L. Kronik, A. M. Rappe, Angew. Chem. Int. Ed. 2015, 54, 12437
10. M. Bag, L. A. Renna, R. Y. Adhikari, S. Karak, F. Liu, P. M. Lahti, T. P. Russell, M. T. Tuominen, D. Venkataraman, J. Am. Chem. Soc. 2015, 137, 13130.

11. G. Richardson, S. E. J. O'Kane, Niemann Ralf G. , T. A. Peltola, J. M. Foster, P. J. Cameron, A. B. Walker, Energy Environ. Sci. 2016, 9, 1476.
12. T.-Y. Yang, G. Gregori, N. Pellet, M. Grätzel, J. Maier, Angew. Chem. Int. Ed. 2015, 127, 8016
13. O. Almora, A. Guerrero, G. Garcia-Belmonte, Appl. Phys. Lett. 2016, 108, 043903.
14. S. D. Stranks, G. E. Eperon, G. Grancini, C. Menelaou, M. J. P. Alcocer, T. Leijtens, L. M. Herz, A. Petrozza, H. J. Snaith, Science 2013, 342, 341.
15. H.-R. Xia, W.-T. Sun, L.-M. Peng, Chem. Comm. 2015, 51, 13787.
16. N. Vicente, G. Garcia-Belmonte, J. Phys. Chem. Lett. 2017, 8, 1371−1374.
17. J. Bisquert, G. Garcia-Belmonte, J. Garćia-Cañadas, J. Chem. Phys. 2004, 120, 6726.
18. D. A. Miranda, P. R. Bueno, Phys. Chem. Chem. Phys. 2016, 18, 25984.
19. J. Bisquert, A. Compte, J. Electroanal. Chem. 2001, 499, 112.
20. G. Garcia-Belmonte, Z. Pomerantz, J. Bisquert, J.-P. Lellouche, A. Zaban, Electrochim. Acta 2004, 49, 3413.
21. J. García-Cañadas, F. Fabregat-Santiago, I. Porqueras, C. Person, J. Bisquert, G. Garcia-Belmonte, Solid State Ionics 2004, 175, 521.
22. J. Bisquert, G. Garcia-Belmonte, A. Pitarch, ChemPhysChem 2003, 4, 287.
23. M. D. Levi, D. Aurbach, J. Phys. Chem. B 2004, 108, 11693.
24. J. P. Meyers, M. Doyle, R. M. Darling, J. Newman, J.Electrochem. Soc. 2000, 147, 2930.
25. J. Bisquert, G. Garcia-Belmonte, F. Fabregat-Santiago, A. Compte, Electrochem. Commun. 1999, 1, 429.
26. M. Haro, N. Vicente, G. Garcia-Belmonte, Adv. Mater. Interfaces 2015, 2, 1500369.

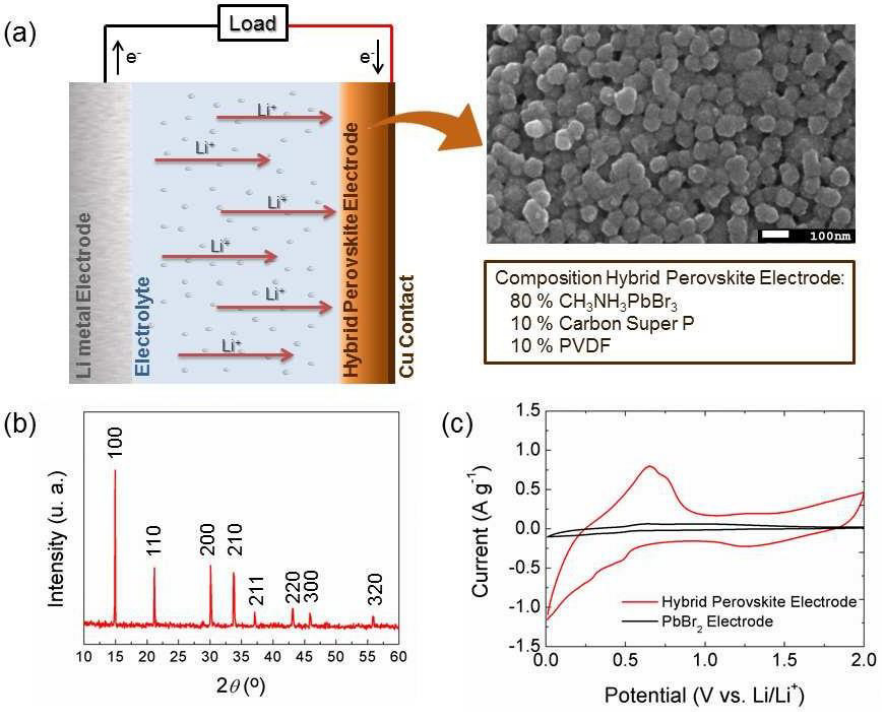

Figure 1. (a) Schema of half-battery set-up indicating the composition of the hybrid perovskite electrode deposited on a cooper contact. SEM image showing the compact structure formed by $CH_3NH_3PbBr_3$ particles. (b) X–ray diffraction patterns of CH3NH3PbBr3. The vertical peaks correspond to the $CH_3NH_3PbBr_3$ cubic phase signals. (c) Stable cyclic voltammetry of $CH_3NH_3PbBr_3$ electrodes after the first four cycles, compared to the electrochemical activity of $PbBr_2$ electrodes.

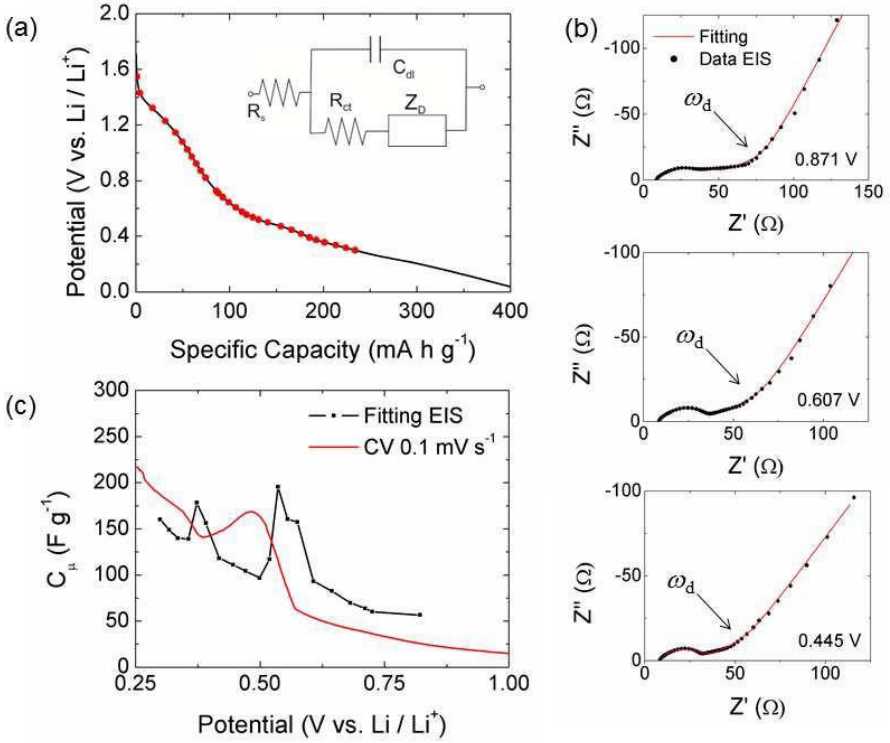

Figure 2. Electrochemical impedance analysis. (a) Selected potentials and charge state of the electrode lithiation process for in-situ EIS analysis during the discharge process. Inset: Randles' equivalent circuit used in the EIS fitting. (b) Impedance spectroscopy response of $CH_3NH_3PbBr_3$ anodes at different steady-state voltages as indicated. Solid line corresponds to fits using the equivalent circuit. The diffusion response frequency d is marked. (c) C calculated from different data: EIS and cyclic voltammetry plotted vs. potential during discharge process.

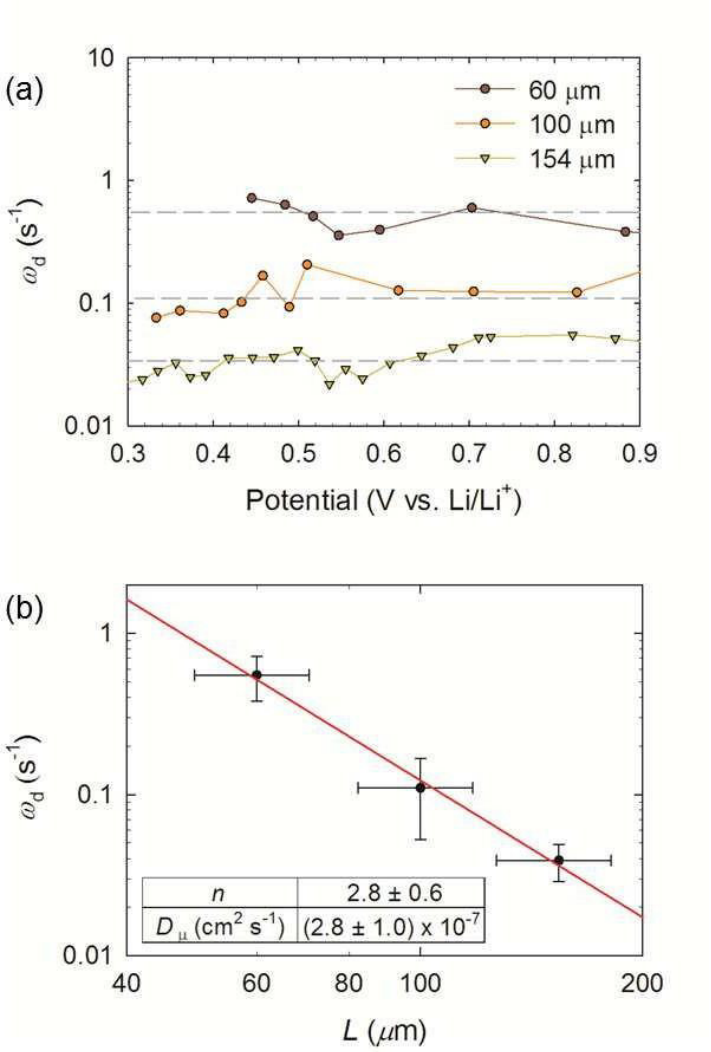

Figure 3. (a) Variation of the diffusion characteristic frequency, d as a function of the battery voltage for three different electrode thicknesses. Dashed lines signals average frequency values. (b) Dependence of the diffusion characteristic frequency with electrode thickness. The used fitting function $\omega_d = D_\mu L^{-n}$ provides values for D_μ = (2.8±1.0) 10^{-7} cm^2 s^{-1}, and thickness coeficient n = 2.8±0.6, considering the experimental error.

From impedance measurements, it is confirmed the superionic intrinsic property of organohalide perovskites. Chemical diffusion coefficient of lithium ions is determined to be as high as 10^{-7} cm^2 s^{-1}. The fast ionic character opens new room for devising applications and devices in which fast ionic migration is an essential requirement.

Perovskites

N. Vicente, G. Garcia-Belmonte*

Organohalide Perovskites Are Fast Ionic Conductors

Supporting Information

Organohalide Perovskites Are Fast Ionic Conductors

Nuria Vicente and Germà Garcia-Belmonte*

Driven mechanism for ion intercalation. Usually intercalation compounds operate by incorporating ionic species, Li^+ most commonly, from the electrolyte. The well-known approach identifies the driving force for ion motion to the gradient in the ion chemical potential. This means that the measured potential relates to the imbalance in the ion chemical potential respect to the reference electrode (Li-metal in our case). The modification of composition in $Li_xCH_3NH_3PbBr_3$ electrodes determines the chemical potential variation $\mu(x)$, with respect to Li/Li^+ potential, μ_{ref}. Therefore the working electrode potential is $eV = -[\mu(x) - \mu_{ref}]$ being e the positive elementary charge. This last expression corresponds to the steady-state situation in which the Li^+ profile inside the electrode is considered to be position-independent. This picture assumes important points concerning the electronic charge: 1) either the chemical potential is mainly determined by the incoming ions or the electronic contribution to the chemical potential does not vary dramatically with composition. This point is fulfilled as the potential range for Li^+ intercalation (0.5 V vs. Li/Li^+) situates more than 1.5 eV above the perovskite conduction band. 2) The electrical field is largely shielded. 3) Electronic mobility largely exceeds ionic mobility. The measured chemical capacitance $C\mu = e^2 N dx/d\mu$ can be determined as the inverse derivative of the equilibrium voltage–composition curve, or from the electrochemical impedance

analysis because it uses a small- amplitude modulation to probe diffusion-capacitive processes.

Decoupling ionic from electronic mobility. Upon intercalation both electronic and ionic densities increase in the perovskite because the Cu foil and carbon used assures a good electronic contact between the active material and the external circuit. Both types of charges (electronic and ionic) participate in the intercalation kinetic process, but the largely superior electronic mobility assures that the overall mechanism is governed by the slowest charge (ions). It is known that the electronic diffusivity (electrons and holes) is $D_e > 10^{-2}$ cm^2 s^{-1} (ref. 14). This assures fulfilling the condition $D_e >> D_i$. This fact allows decoupling iònic from electronic mobility. Because the same amount of ionic (Li^+) and electronic charge (e^-) is inserted upon intercalation, electronic conductivity should always exceeds ionic one. This fact entails that electrons rapidly equilibrate and shield the electrical field while the ion transport effectively governs the kinetics of electrode charging to reach a given potential.

Double-layer capacitance. The variation of double-layer capacitance with voltage for several layer thickness values allows confirming the outlined ion diffusion model.

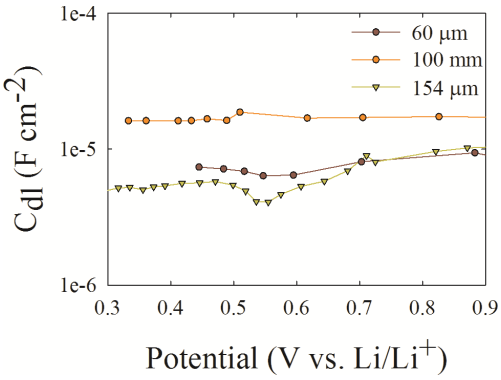

Figure S1. Example of variation of the double-layer capacitance as a function of the battery potential for different electrode thicknesses. As observed there is no correlation between both parameters. C_{dl} is always situated around typical vàlues in the order of 10 µF cm^{-2}.

7

Publication 5

7.1. Candidate's contribution

In this case of Chapter 6, the nature and extent of my contribution to the work was the following:

Nature of contribution	Extent of contribution
• Design in-situ experiments in Helmholtz Insitute Ulm under supervision Prof. Passerini • Analysis and discussion the experimental data • Discussion validity of the proposed mechanism for perovskites anodes • Write the manuscrit drafts. • Edit the manuscrit in accordance with the comments provided by co-authors and referees.	80 %

7.2. Published manuscript

Nuria Vicente, Dominic Bresser, Stefano Passerini, Germà Garcia-Belmonte. Probing the 4-step Lithium storage Mechanism in $CH_3NH_3PbBr_3$ Perovskite Electrode by Operando-XRD Analysis, *ChemElectroChem*, **2019**, 6, 456 – 460.

Probing the 3-step Lithium Storage Mechanism in $CH_3NH_3PbBr_3$ Perovskite Electrode by *Operando*-XRD Analysis

Nuria Vicente[a], Dominic Bresser[b,c], Stefano Passerini[b,c] and Germà Garcia-Belmonte[a,*]

[a] Institute of Advanced Materials (INAM), Universitat Jaume I, 12006 Castelló, Spain

[b] Helmholtz Institute Ulm (HIU), Helmholtzstrasse 11, 89081 Ulm, Germany

[c] Karlsruhe Institute of Technology (KIT), P.O. Box 3640, 76021 Karlsruhe, Germany

*Corresponding author's e-mail: G. Garcia-Belmonte (garciag@uji.es)

Abstract

Organic-inorganic hybrid materials have gradually become one of the most actively studied research fields due to their fascinating properties. The reaction between lithium and organic-inorganic halide perovskite has just recently been proposed. However, the exact mechanisms taking place in this electrode material have not been fully elucidated, yet. To shed light on these processes an *operando*-X-ray diffraction study has been performed and is reported herein. According

to our results the lithiation of $CH_3NH_3PbBr_3$ entails three reaction steps, distinguishable during the initial galvanostatic lithiation for different Li-ion molar contents x: [1] the initial Li^+ insertion into the perovskite phase in which pure perovskite and lithiated phases coexist ($0 < x < 1$), [2] the perovskite conversion reaction leading to the formation of metallic lead ($1 < x < 2$), and finally, [3] the alloying of lithium with the metallic lead previously formed. In more detail, for $x > 0.3$, the formation of a Li_x:$CH_3NH_3PbBr_3$ phase with distinctive X-ray diffraction peaks is clearly detected, which coexists with the pristine material, till abruptly both phases disappear at $x \sim 1$ and CH_3NH_3Br and Pb metal are formed. It is shown that this conversion reaction is an irreversible process. The proposed mechanism for lithium storage gives a complete perspective of the complex structural environment involving the use of perovskite materials as electrodes for Li-ion batteries.

TOC figure:

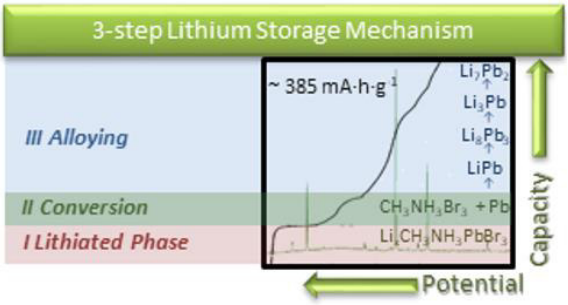

A Table of Contents text:

By *operando*-X-ray diffraction analysis, lithiation of $CH_3NH_3PbBr_3$ occurs through three reaction steps. For Li-ion molar contents ($0 < x < 1$), perovskite and lithiated phases coexist without drastic structural reordering. A conversion reaction leading to the formation of metallic lead ($1 < x < 2$) is observed, followed by the alloying of lithium with the metallic lead previously formed ($x > 2$).

1. Introduction

Studies on the already well-established Li-ion battery (LIB) technology are focusing on novel lithium storage materials and electrode architectures, enhancing the cycling stability and safety as well as lowering the overall cost through the design of innovative materials. A recent publication proposed the use of organic-inorganic hybrid perovskite materials as promising anodes to improve the battery performance of LIBs [1]. These materials attract tremendous scientific attention in the field of photovoltaics since 2009 when the first application of hybrid perovskites in solar cells was reported [2]. The revolution in the use of hybrid perovskites for solid state solar cells started in 2012, when photovoltaic power conversion efficiencies of 9.7% and 10.9%, were reported [3, 4]. Motivated, moreover, by its prominent properties (high absorption coefficient, low charge-carrier recombination rates, as well as easy and low cost of cell fabrication by chemical methods and abundance of raw materials) further work lead to the achievement of impressive power conversion efficiencies of more than 20.0% [5]. Furthermore, because of their ability to host extrinsic elements such as Li^+ or Na^+, while simultaneously exhibiting high ion diffusivity, its potential for battery applications should be deeply studied. However, a complete analysis of the mechanisms taking place during the charge and discharge processes in these kinds of electrodes has not been reported, yet.

The first works exploring hybrid perovskites as storage materials and the early proposed mechanisms have been based on *ex-situ* experiments. The first report dates from 2015. Therein, methylammonium lead halide perovskites were suggested as active material for Li-ion battery anodes by Xia et al. [1]. The authors prepared $CH_3NH_3PbI_3$ and $CH_3NH_3PbBr_3$ by hydrothermal synthesis,

characterized them as anodes, and demonstrated first cycle discharge capacities of 43.6 and 331.8 $mA \cdot h \cdot g^{-1}$, respectively. After 200 charge–discharge cycles, the capacity was still 121 $mA \cdot h \cdot g^{-1}$ in the case of $CH_3NH_3PbBr_3$ with a relative capacity retention of 76.9%, highlighting the important role of the composition of organometallic halide perovskite (AMX_3) on the lithium storage performance.

Afterwards, numerous groups working on perovskite materials and/or batteries have entered this research subject –either with studies on innovative hybrid materials or theoretical calculations to evaluate the electrochemical performance. The influence of composition and crystalline structure, as two important factors contributing to the high de-/lithiation capacity and reversibility, have been studied by Tathavadekar et al. [6]. They showed that the specific capacity and cycling stability can be improved by tuning the dimensionality of halide-perovskites from 3D to 1D. It is said that the molecularly engineered low-D perovskites exhibit an open structure, which adopts a morphology favorable for facile ion access. The benzidine-mediated, 1D lead iodide-based perovskites show high reversible capacity values of 646 $mA \cdot h \cdot g^{-1}$ with great cycling stability [6]. These parameters are superior in comparison to the usual 3D lead iodide based perovskite. By performing *ex-situ* XRD, it was revealed that the storage primarily occurs *via* the Li_xPb alloying process. Meanwhile, a deeper study on the 2D hybrid perovskite using powder composite electrodes was carried out by Ramirez et al. [7]. They reported that 3D $CH_3NH_3PbBr_3$ reached a high discharge capacity of ~500 $mA \cdot h \cdot g^{-1}$, followed by a reduced charge capacity of 160 $mA \cdot h \cdot g^{-1}$. It was proposed that this irreversibility resulted also from other processes taking place during the lithiation reaction, since the newly synthesized 2D $(CH_3NH_3)_2(CH_3(CH_2)_2NH_3)_2Pb_3Br_{10}$ with a layered structure showed

100% reversibility during cycling with capacities of ~375 $mA \cdot h \cdot g^{-1}$. As a consequence, it has been concluded that 2D layered structures are advantageous for the reversible lithium-ion storage. The authors, moreover, contributed to an enhanced understanding of the lithium insertion/extraction mechanism by revealing the initial occurrence of the intercalation process in the hybrid material, accompanied by the reversible alloying process of the Li_xPb intermetallic compounds formed.

On the other hand, also the properties of lithium-doped $CsPbBr_3$ all-inorganic perovskite have been studied [8]. It has been reported in that study that lithium doping enhances the light emission of LEDs with low turn-on voltage and its absorption of light. It was further found that the lithium doping leads to a diamagnetic behavior, PL blue-shift, as well as higher photovoltage and photocurrent behavior, indicating that the presence of lithium can improve the photovoltaic performance of the material. The doping ratio, however, was controlled to avoid the degradation of the perovskite structure. Nonetheless, the electrochemical studies evidenced that about three lithium ions can be doped in the $CsPbBr_3$ crystal [9]. In a recent publication [10], the protocol for electrochemical tests of all-inorganic $CsPbBr_3$ and hybrid organic–inorganic $CH_3NH_3PbI_3$ perovskites has been proposed. By *ex-situ* experiments, such as XRD, XPS, SEM-EDX analysis, it has been shown that metallic Pb is eventually formed upon reduction [10]. During oxidation and reduction, the Br^- and Pb^{2+}, respectively, are gradually decreasing due to the degradation of the $CsPbBr_3$ structure. Two oxidation steps and one reduction step were revealed by spectroelectrochemical studies, at potentials of +0.8 V, +1.1 V, and −0.75 V vs. Ag/Ag^+, respectively.

These redox processes were coupled with the decrease in the absorbance related to $CH_3NH_3PbI_3$ and its degradation rate.

The complete mechanism of the hybrid perovskite electrode operation has been proposed very recently [11]. A combination of simulation methods (density functional theory, DFT, with the *ab initio* code VASP) and *ex-situ* powder X-Ray diffraction (PXRD) techniques has been used to analyze a wide variety of electronic, structural, and defect properties of hybrid halide perovskites as Li-ion battery active material. The calculations revealed a conversion process to lithium halides (LiX) and Pb metal, which dominates the electrode reactions, particularly for $CH_3NH_3PbBr_3$ and $CH_3NH_3PbCl_3$.

In our previous publication [12], we obtained high capacity values for $CH_3NH_3PbBr_3$ upon the first discharge, i.e., ~600 $mA \cdot h \cdot g^{-1}$, followed by an important decrease in the second cycle to ~400 $mA \cdot h \cdot g^{-1}$, and finally delivering a stable capacity of ~200 $mA \cdot h \cdot g^{-1}$. This is interpreted as an indication that additional processes are taking place, such as the formation of a solid electrolyte interphase (SEI) and changes in the perovskite structure [7, 11]. The theoretical discharge capacity for these materials is close to 50 $mA \cdot h \cdot g^{-1}$, for a Li-ion molar fraction of $x = 1$ in the pristine hybrid materials for an insertion mechanism. Accordingly, the processes taking place during lithiation are very complex and some kind of electrode restructuring is occurring. Moreover, by electrochemical impedance spectroscopy the diffusivity coefficient in $CH_3NH_3PbBr_3$ was determined, providing diffusivity values as high as $D_\mu \approx 10^{-7}$ $cm^2\ s^{-1}$ [13]. This value highlights the fast ionic conductivity of hybrid perovskite compounds, as recently corroborated for intrinsic defect migration [14].

Here, we elucidate the complexity of the mechanisms taking place in $CH_3NH_3PbBr_3$ when utilized as lithium-ion anode material. The structural evolution of $CH_3NH_3PbBr_3$ is studied by *operando*-XRD during the discharge–charge (lithiation-delithiation) process, revealing for the first time that the hybrid perovskite material suffers a critical crystal structure rearrangement at Li^+ molar contents higher than 1. Before this limit, the pure perovskite phase is maintained despite the high Li^+ density, coexisting with a lithiated phase and the formation of metallic Pb. For $1 < x < 2$, the presence of the CH_3NH_3Br precursor is detected, signaling the occurrence of the conversion reaction, leading to the formation of Pb^0. For a higher Li^+ molar content, $x > 2$, the alloying reaction occurs, resulting in the formation of the Li-Pb alloy. Moreover, the substantial irreversibility observed for the first cycle is associated with the conversion reaction, as also reflected by the corresponding electrochemical response.

2. Experimental

The perovskite material was synthesized by the slow solvent evaporation from a solution containing stoichiometric amounts of lead bromide ($PbBr_2$, TCI) and methylammoniumbromide (CH_3NH_3Br, >98% TCI) in *N,N*-dimethylformamide (DMF, Sigma-Aldrich), resulting in the formation of an orange precipitate. A Bruker AXS-D4 Endeavor Advance X-ray diffractometer using Cu K , wavelength = 1.5406 Å, is employed for the X-ray diffraction (XRD) analysis to confirm the phase-pure perovskite crystallographic structure [12].

Perovskite-based electrodes were prepared by casting slurries, which solid content was 80 wt% active material ($CH_3NH_3PbBr_3$; 65 nm average size particles), 10 wt% Super C65 (TIMCAL), and 10 wt%

PVdF (5130 Solvay), dispersed in *N*-methyl-2-pyrrolidone as solvent, on copper foil (Schlenk). Li metal foil (battery grade, Honjo Metal Co.) was used as the counter and reference electrode and an electrolyte-soaked sheet of glass fiber (Whatman) was employed as separator. The electrolyte was 1M lithium hexafluorophosphate ($LiPF_6$, Sigma-Aldrich) in ethylene carbonate, ethyl-methyl carbonate, and dimethyl carbonate (EC:EMC:DMC = 1:1:1 vol; UBE). Cell assembly was carried out in an argon-filled glovebox with O_2 and H_2O content lower than 1 ppm.

The study of the Li uptake mechanism was performed via *operando*-XRD analysis coupled with galvanostatic lithiation (discharge) and delithiation (charge) steps. The *operando*-XRD study was performed using the Cu K_α radiation on the D8 Advance (Bruker) in Bragg–Brentano mode. Electrodes were prepared by casting the active material slurry directly on the beryllium (Be) window, which served as current collector and "window" for the X-ray beam.[15] The active material mass loading of the electrodes was about 10 $mg \cdot cm^{-2}$. The assembled cell was allowed to rest for one hour. Subsequently, the cell was galvanostatically cycled by means of a Solartron 1287 potentiostat, applying a specific current of 10 $mA \cdot g^{-1}$, calculated according to a complete discharge (cathodic cut-off potential: 0.05 V) in 37.8 h. In parallel, XRD analysis was performed within a 2θ range of 10° to 50° and with a step size of 0.02°, resulting in a complete scan every 30 min. After discharging to 0.05 V, the cell was charged to an anodic cut-off potential of 1.80 V. All potential values reported in this work refer to the Li/Li^+ quasi-reference couple and all capacity data are normalized to the mass of the $CH_3NH_3PbBr_3$ active material. Further details regarding the structural, morphological, and electrochemical

characterization of the active material can be found in our previous works [12, 13].

3. Results and discussion

$CH_3NH_3PbBr_3$ is gaining interest as a negative electrode material for Li-ion batteries because of its high specific capacity exceeding the specific capacity of graphite and $Li_4Ti_5O_{12}$ [16]. However, the various intermediate conversion and alloying reactions occurring during lithiation/delithiation, as well as the electrolyte stability have not been fully elucidated and many ambiguities remain. In **Figure 1a,** the galvanostatic charge-discharge curves of the perovskite-based electrode at a specific current of 100 $mA \cdot g^{-1}$ are shown and several voltage plateaus are observed. During the first discharge, a first plateau is observed at around 2.3 V vs. Li/Li^+, where Li is assumed to be inserted into the perovskite structure. Between 2.3 and 1.85 V vs. Li/Li^+, it is assumed that $CH_3NH_3PbBr_3$ and $Li_xCH_3NH_3PbBr_3$ phases coexist. The subsequent plateau at 1.4 V is presumably related to the formation of Pb^0 through the conversion reaction. Then, between 0.60 and 0.29 V vs. Li/Li^+, several Li_xPb_y phases with increasing lithium content are formed. The first discharge will be explained in more detail below. Following the first discharge process, a significant irreversibility is observed. The material is unable to recover the initial capacity, which dramatically fades during the initial 10 cycles. In fact, no XRD signal corresponding to $CH_3NH_3PbBr_3$ can be observed even after the complete galvanostatic delithiation (Figure 1b), indicating that the initial conversion reaction

is essentially irreversible and only the subsequent alloying process provides the observed charge-discharge capacities.

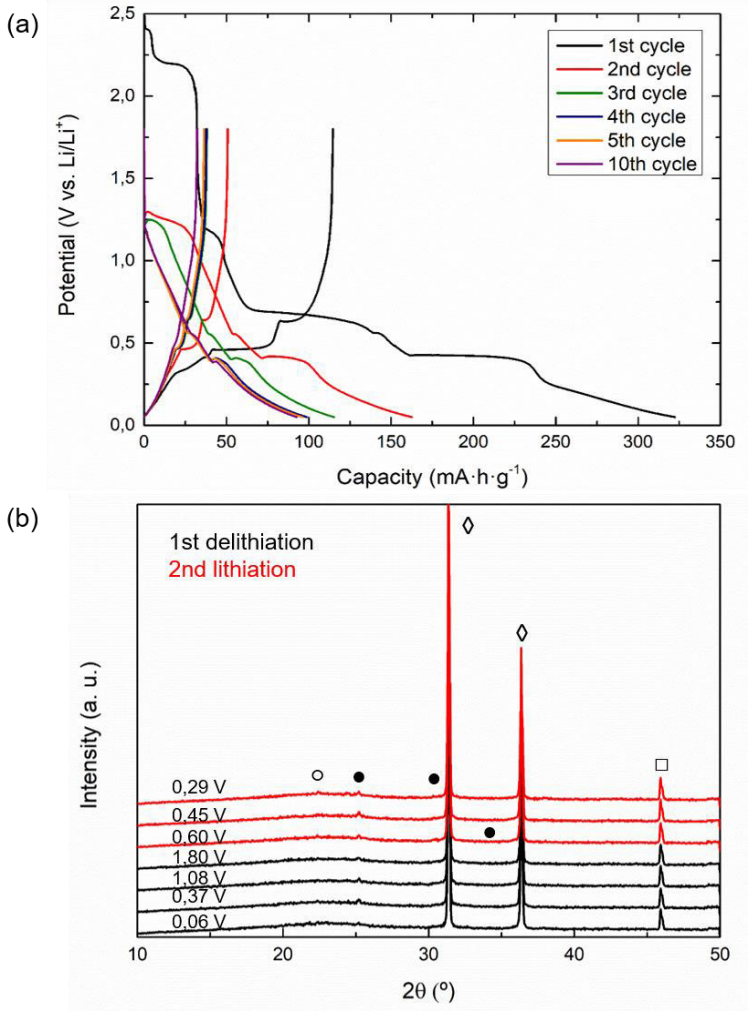

Figure 1. (a) Galvanostatic dis-/charge profiles for $CH_3NH_3PbBr_3$ as lithium-ion active material at a specific current of 100 mA · g^{-1} for the first 10 cycles. (b) In *operando*-XRD scans corresponding to the alloying stage during the first delithiation and second lithiation: (○) Li_8Pb_3,(•) LiPb, (◊) Pb and (□) Be.

The *operando*-XRD patterns obtained during the first lithiation of the sample (galvanostatic discharge down to 0.05 V) are presented in **Figure 2**. The diffractograms show that $CH_3NH_3PbBr_3$ is always present at potentials higher than 1.85 V. For the pristine material (red diffractograms in Figure 2), the characteristic perovskite reflections are observed, whose corresponding lattice parameter (a = 5.9394 Å; space group: P3-m3) is in good agreement with a previous report [1]. For the first stage of the discharge curve, a reflection at 45.9º is observed, which corresponds to the overlapping of two reflections related to the perovskite and metallic beryllium. After the conversion stage, only the beryllium reflection is observed (space group $P6_3/mmc$, $a = b = 2.285$ Å and $c = 3.622$ Å).

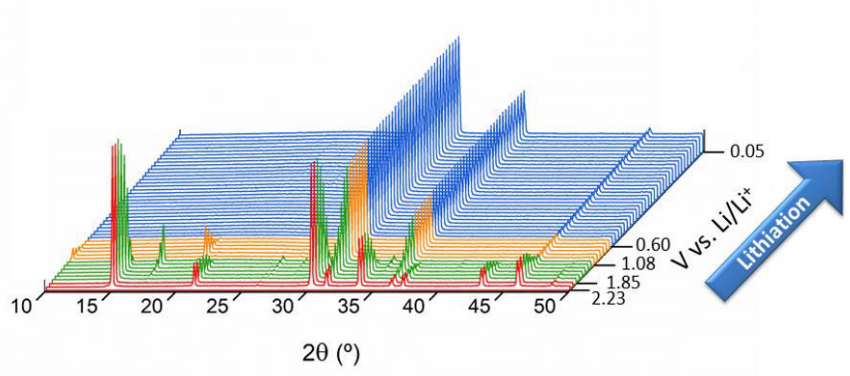

Figure 2. First discharge *operando*-XRD patterns recorded for the $CH_3NH_3PbBr_3$–based electrode. Different stages are indicated by different colors: Stage I: pristine material (red) and lithiated phase (green); Stage II: conversion (orange); and Stage III: alloying (blue).

The *operando*-XRD measurement reveals that the pristine perovskite active material is detected only at the beginning, i.e., for the four first

XRD patterns (red diffractograms in Figure 2). A new phase is formed, when the Li^+ molar content approaches $x \sim 0.3$. The appearance of diffraction peaks at 17.3º, 26.5º, 28.3º, 33.3º, 35.0º, and 40.5º can be attributed to the formation of a lithiated phase Li_x:$CH_3NH_3PbBr_3$ that distorts the perovskite structure (green diffractograms in Figure 2). Therefore, two phases coexist for a Li^+ molar content of $x < 1.08$ (stage I). In addition, the appearance and growth of two reflections at 31.2º and 36.3º, corresponding to metallic Pb, are observed, presumably indicating the concurrence of the conversion reaction at least on the active material particles surface. During this stage (green XRD patterns in Figure 2), the characteristic perovskite diffraction peaks become weaker upon further lithiation, while the reflections for the lithiated phase become more evident. Both phases (pure $CH_3NH_3PbBr_3$ and lithiated Li_x:$CH_3NH_3PbBr_3$) disappear abruptly at the beginning of the next stage, which occurs for a lithium content of $x > 1.08$ and a cell voltage of 1.85 V vs. Li/Li^+ (stage II; orange diffractograms). It appears that the structure cannot insert more Li^+ without severe structural distortions and, as a consequence, the cubic structure vanishes. **Figure 3** shows the proposed transformation diagram, which links the characteristic XRD patterns for each stage with the discharge profile, specific capacity, and lithium content.

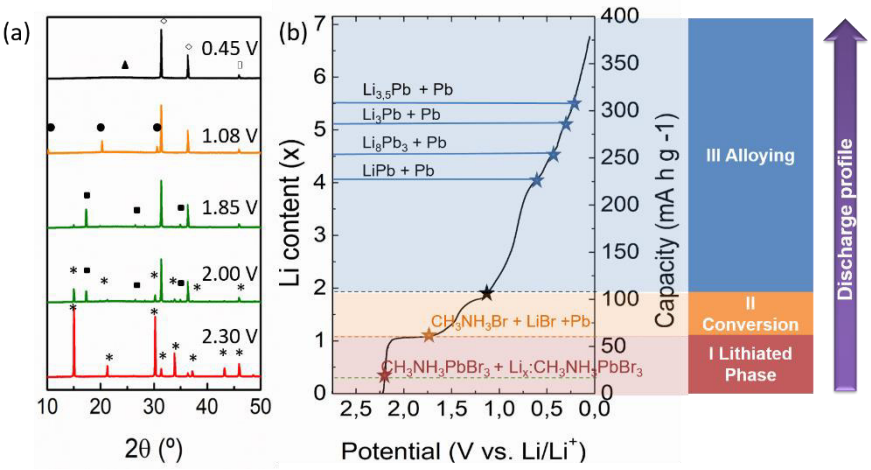

Figure 3. (a) Selected characteristic *operando*-XRD patterns of $CH_3NH_3PbBr_3$ for every stage: (*) $CH_3NH_3PbBr_3$, (▪) $Li_xCH_3NH_3PbBr_3$, (•) CH_3NH_3Br, (▲) Li_8Pb_3 (better resolution Fig. 1.b), (◊) Pb, and (□) Be. (b) The recorded discharge profile, where each stage is highlighted in a different color: First, the pure material (red), and lithiated phase (red); second, the conversion stage (orange), and, third, the alloying stage (blue). The occurring alloying reactions, i.e., the different lithium/lead phased are provided in the figure.

When the pristine material and the lithiated phase disappear, new diffraction peaks are observed at 10.1º and 20.3º, as shown in Figure 3a. The new diffraction peaks correspond to the CH_3NH_3Br precursor [17], indicating the loss of the initial perovskite structure and the occurrence of a conversion reaction according to $Li{:}CH_3NH_3PbBr_3 \rightarrow CH_3NH_3Br + LiBr + Pb$ (stage II). This phase, however, disappears at the end of the conversion stage, i.e., for a Li^+ molar content of $x \sim 2$, it could be caused by its dissolution in electrolyte, such is

actually the case for LiBr. In agreement with previous XRD results,[18] the plateau in the discharge profile near ~1.08 V vs. Li/Li^+ corresponds to the Pb(II) → Pb(0) reduction process. It is possible to identify two reflections at 31.2º and 36.3º, which can be matched to metallic Pb (space group Fm3m, a = 4.951 Å).

Subsequently, the Li-Pb alloying starts ($x > 2$; stage III). The corresponding plateaus in the discharge profile between 0.4—0.6 V vs. Li/Li^+ are associated with the formation of different Li-Pb phases, such as LiPb, Li_8Pb_3, Li_3Pb, and $Li_{3.5}Pb$, which have been also identified in the same voltage range for electrodes based on pure lead metal.[18] For our *operando*-XRD, first, one new, relatively weak reflection appears at 25.29º, which is assigned to the formation of LiPb (see also Figure 1b). After $x \sim 4.1$, this reflection disappears and another new diffraction peak is observed at 22.3º, corresponding to Li_8Pb_3. The occurrence of these two phase transitions are related to the two voltage plateaus at 0.601 V and 0.449 V, respectively. Finally, the formation of Li_3Pb is observed ($2\theta \sim 23$º), while no appreciable reflection for the formation of $Li_{3.5}Pb$ is detected. At the end of the discharge process, around 6 Li^+ per formula unit of the perovskite has been stored in the electrode. After all, the reverse evolutions of diffraction peaks corresponding to Pb and Li-Pb alloys can be followed down to 1.5 V vs. Li/Li^+ (Figure 1b) [18]. The irreversibility of the conversion reactions leave the alloying reaction as the only storage mechanism, as also confirmed by the long-term cycling experiments and in accordance with previous studies [1, 7, 12].

Based on this *operando*-XRD analysis, we propose the following series of electrochemical reactions for the complete lithiation mechanism, shown in **Table 1**. In Figure 3b the lithiated phase and conversion

products as well as the alloying reactions are shown, accompanying the discharge curve and the potentials of the observed plateaus. Based on these reactions, the theoretical discharge capacity of the investigated perovskite material (for $x \sim 6$) is around 358 $\mathrm{mA \cdot h \cdot g^{-1}}$. By calculating the potential derivative of the initial lithiation curve as $-\mathrm{d}Q/\mathrm{d}V$, one can observe a set of reaction peaks (Supporting Information) that corroborate the proposed mechanisms.

Table 1. Lithium content, products formed at characteristics potentials, and the electrode's capacity for the different stages: lithiated phase, conversion, and alloying.

Li^+ content x	**Detected Phases**	**End Potential of Stage (V vs. Li/Li^+)**	**Capacity ($mA \cdot h \cdot g^{-1}$)**	**Stage**
$0.00 < x < 1.10$	$CH_3NH_3PbBr_3$ $Li_xCH_3NH_3PbBr_3$	≈ 1.85	≈ 55	I Lithiated Phase
$1.10 < x < 1.90$	CH_3NH_3Br, LiBr, Pb	≈ 1.08	≈ 110	II Conversion
$1.90 < x < 4.10$	Pb	≈ 0.60	≈ 225	III Alloying
$4.10 < x < 4.50$	Pb, LiPb	≈ 0.60	≈ 225	
$4.50 < x < 5.15$	Pb, Li_8Pb_3	≈ 0.45	≈ 255	
$5.15 < x < 5.50$	Pb, Li_3Pb	≈ 0.37	≈ 285	
$x > 5.50$	Pb, $Li_{3.5}Pb$	≈ 0.29	≈ 315	

The proposed mechanism comprises the occurrence of different stages: First, an insertion mechanism, for which only the initial

perovskite structure is present (stage I), followed by further lithiation until the appearance of the lithiated phase; the second stage is characterized by a pure conversion reaction (stage II), before eventually reaching the final alloying stage III. The stages I and II are irreversible, causing the greatly modified electrochemical response after the first full lithiation. On the other hand, the alloying reactions are considered to be partially reversible reactions as it is evidenced in Figure 1a. Lead alloying reaction reversibility was deeply studied in previous work [19].

4. Conclusions

In summary, this exhaustive experimental study reports *operando*-XRD results for an organic-inorganic halide perovskite-like anode for Li-ion batteries, $CH_3NH_3PbBr_3$. It has been probed that the lithiation proceeds by a complex 3-step storage mechanism in this electrode material. Li-ion insertion is followed by conversion processes with the eventual formation of CH_3NH_3Br and metallic Pb. After these stages, the metallic lead is alloying with lithium by forming a series of Li-Pb phases: LiPb, Li_8Pb_3, and Li_3Pb. The findings reveal that the structural evolution of such organic-inorganic perovskite during the first lithiation process is largely irreversible, which explains the extensive capacity fading after the first discharge. This work proposes a complete mechanism for perovskite-based electrodes with important insights that are anticipated to foster their potential application in the field of batteries. Moreover, these insights into the reaction mechanism and ion accommodation into the crystal structure may guide also the application of lithium-doped perovskites in the field of

solar cells, as Li-containing solar cells show a varying hysteresis depending on the scan rate due to the different kinetics of extrinsic and intrinsic ion migration [20].

Author Information.

Corresponding author: garciag@uji.es

ORCID

Nuria Vicente: 0000-0002-9823-7131

Dr. Dominic Bresser: 0000-0001-6429-6048

Prof. Stefano Passerini: 0000-0002-6606-5304

Prof. Germà Garcia-Belmonte: 0000-0002-0172-6175

Notes

The authors declare no competing financial interest.

Acknowledgments

We are grateful for financial support by Ministerio de Economía y Competitividad (MINECO) of Spain under Project (MAT2016-76892-C3-1-R). N. Vicente acknowledges Universitat Jaume I (UJI) through FPI Fellowship Program (PREDOC / 2015/54) and (E-2017-18) within framework of Action 2 of the Mobility Program for Research

Staff under the 2017 Research Promotion Plan. SCIC from Universitat Jaume I is also acknowledged.

Keywords

Extrinsic ion, hybrid perovskite, lithium doping, storage mechanism, X-ray diffraction

References

1. H.-R. Xia, W.-T. Sun, L.-M. Peng *Chem. Commun.* **2015**, *51*, 13787-13790.
2. A. Kojima, K. Teshima, Y. Shirai, T. Miyasaka *J. Am. Chem. Soc.* **2009**, *131*, 6050-6051.
3. L. Etgar, P. Gao, Z. Xue, Q. Peng, A. K. Chandiran, B. Liu, M. K. Nazeeruddin, M. Grätzel *J. Am. Chem. Soc.* **2012**, *134*, 17396-17399.
4. M. Lee, J. Teuscher, T. Miyasaka, T. Murakami, H. Snaith *Science.* **2012**, *338*, 643-647.
5. M. A. Green, Y. Hishikawa, E. D. Dunlop, D. H. Levi, J. Hohl-Ebinger, A. W. Y. Ho-Baillie *Prog. Photovoltaics Res. Appl .* **2018**, *26*, 3-12.
6. M. Tathavadekar, S. Krishnamurthy, A. Banerjee, S. Nagane, Y. Gawli, A. Suryawanshi, S. Bhat, D. Puthusseri, A. D. Mohite, S. Ogale *J. Mater. Chem. A.* **2017**, *5*, 18634-18642.
7. D. Ramirez, Y. Suto, N. C. Rosero-Navarro, A. Miura, K. Tadanaga, F. Jaramillo *Inorg. Chem.* **2018**, *57*, 4181-4188.

8. Q. Jiang, X. Zeng, N. Wang, Z. Xiao, Z. Guo, J. Lu *ACS Energy Lett.* **2018**, *3*, 264-269.
9. Q. Jiang, M. Chen, J. Li, M. Wang, X. Zeng, T. Besara, J. Lu, Y. Xin, X. Shan, B. Pan, C. Wang, S. Lin, T. Siegrist, Q. Xiao, Z. Yu *ACS Nano.* **2017**, *11*, 1073-1079.
10. G. F. Samu, R. A. Scheidt, P. V. Kamat, C. Janáky *Chem. Mater.* **2018**, *30*, 561-569.
11. J. A. Dawson, A. J. Naylor, C. Eames, M. Roberts, W. Zhang, H. J. Snaith, P. G. Bruce, M. S. Islam *ACS Energy Lett.* **2017**, *2*, 1818-1824.
12. N. Vicente, G. Garcia-Belmonte *J. Phys. Chem. Lett.* **2017**, *8*, 1371-1374.
13. N. Vicente, G. Garcia-Belmonte *Adv. Energy Mater.* **2017**, *7*, 1700710.
14. W. Peng, C. Aranda, O. M. Bakr, G. Garcia-Belmonte, J. Bisquert, A. Guerrero *ACS Energy Lett.* **2018**, 1477-1481.
15. D. Bresser, E. Paillard, R. Kloepsch, S. Krueger, M. Fiedler, R. Schmitz, D. Baither, M. Winter, S. Passerini *Adv. Energy Mater.* **2013**, *3*, 513-523.
16. N. Nitta, F. Wu, J. T. Lee, G. Yushin *Mater. Today.* **2015**, *18*, 252-264.
17. E. J. Gabe *Acta Crystallogr.* **1961**, *14*, 1296.
18. S. M. Wood, C. H. Pham, A. Heller, C. B. Mullins *J. Electrochem. Soc.* **2016**, *163*, A1027-A1029.
19. M. Martos, J. Morales, L. Sanchez *Electrochim. Acta.* **2003**, *48*, 615-621.
20. Z. Li, C. Xiao, Y. Yang, S. P. Harvey, D. H. Kim, J. A. Christians, M. Yang, P. Schulz, S. U. Nanayakkara, C.-S. Jiang *Energy Environ. Sci.* **2017**, *10*, 1234-1242.

Supporting Information:

Probing the 3-step Lithium Storage Mechanism in $CH_3NH_3PbBr_3$ Perovskite Electrode by *Operando*-XRD Analysis

Here potential derivative curve shows the maximus that correspond to the plateaus of the discharge profile (red line). The different stages (lithiated phase, conversion and alloying) are provided by the different phases, which are observed in XRD diffractograms (see **Figure 2**). The end of the stages match at the turning points.

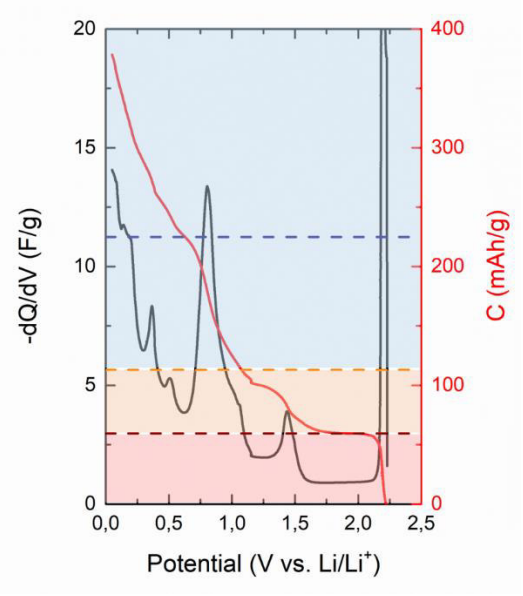

Figure 1. The recorded discharge profile (solid red line, right axis), where each stage is highlighted in a different color: First, the pure material (red), and lithiated phase

(red); second, the conversion stage (orange), and, third, the alloying stage (blue). On the left axis, potential derivative profile could be read (solid black line).

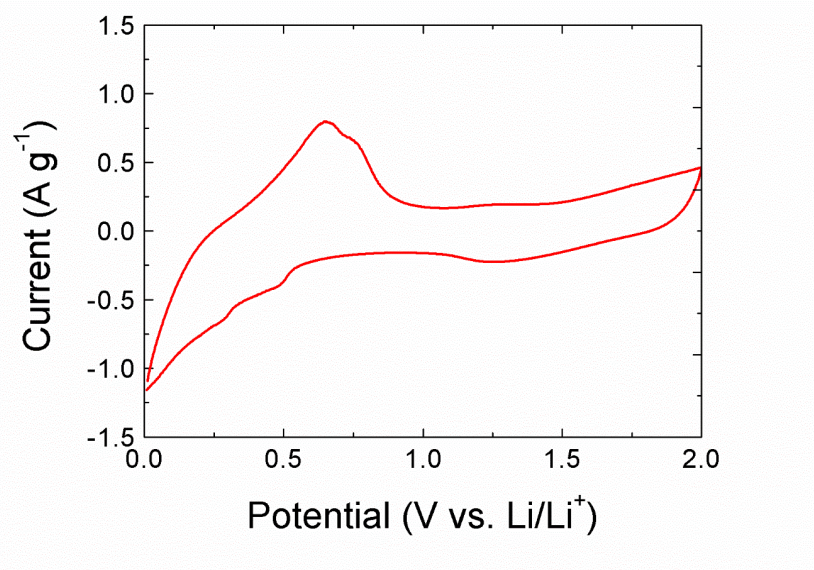

Figure 2. First cycli voltammetry of $CH_3NH_3PbBr_3$ electrodes.

8

Conclusions i futures línies d'investigació

En aquest últim capítol es presenten les conclusions dels diferents articles presentats en aquesta tesi doctoral, els quals han estat publicats en revistes d'alt impacte científic a nivell internacional.

Primerament, s'ha pogut mostrar que l'ús de la tècnica no destructiva d'espectroscòpia d'impedància electroquímica, junt a tècniques de caracterització fisicoquímiques i electroquímiques, permet determinar la resposta dels elèctrodes a estudiar. Fent ús de circuits equivalents possibilita fer la connexió entre la morfologia de l'elèctrode i els mecanismes electroquímics que tenen lloc, arribant a diferenciar el factor limitant: mecanismes limitats per la transferència de carrega o per la cinètica de la reacció que es produeix durant el ciclat.

I en particular, la caracterització dels elèctrodes per a bateries de liti utilitzant la tècnica d'impedància ens ha possibilitat:

- Per al fosfat de ferro-liti, $LiFePO_4$, mineral natural de la família de l'olivina, s'ha pogut modelar mitjançant circuits equivalents per a elèctrodes de multi partícules i on el mecanisme limitant és la difusió de liti.
  Aquests circuits possibiliten diferenciar la difusió del liti en la interfase càtode-electròlit (altes freqüències) i el

comportament capacitiu quan el liti és emmagatzemat en el càtode. A més a més, avaluar l'estratègia seguida embevent els partícules de LFP en una matriu de PEDOT per aconseguir millorar la seva conductivitat elèctrica.

- En les bateries de liti oxigen, on l'energia s'emmagatzema quan el ió liti reacciona directament en l'oxigen molecular en elèctrode porós. El circuit equivalent proposat permet identificar el fenomen de doble capa independent de l'oxigen, la capacitat de doble capa corresponent a l'adsorció de O_2, i quantificar la capacitat química de la reacció de reducció d'oxigen.

- I, l'últim mòdul d'aquesta Tesi, corresponent a les recents bateries amb ànodes de perovskita híbrida d'halur de plom. D'una banda, ha sigut el primer cop que es proposa un mecanisme d'emmagatzematge de liti en tres etapes: inserció, conversió i aliatge, amb evidències obtingudes amb experimentació *operando*.

  I d'altra banda, la configuració de bateria i l'estudi la modelització dels espectres d'impedància permet el càlcul del coeficient de difusió del ió de liti en $CH_3NH_3PbBr_3$.

En conclusió, queda evidenciat la gran utilitat que suposa l'eina de la tècnica de l'espectroscòpia d'impedància per a la caracterització d'elèctrodes. Els resultats d'aquesta Tesis Doctoral, i en concret els corresponents a bateries de liti amb ànodes de perovskita són l'etapa inicial d'una línia d'investigació innovadora que està atraient a laboratoris punters especialitzats en bateries, així com també laboratoris que treballen en fotovoltaica.

En primer lloc, el mecanisme proposat per a ànodes de perovskita on diferenciem tres etapes i com es produeix la degradació del material

de partida, pot facilitar poder esbrinar les conseqüències del dopat de liti en cel · les de perovskita i com intervé en la degradació, així com definir un límit de contingut de liti en les configuracions, per tal d'augmentar la seua estabilitat.

En segon lloc, si som capaços de definir els límits de treball i es podria dissenyar una configuració òptima per a una fotobateria integrada la qual fora capaç de convertir l'energia solar en energia elèctrica i emmagatzemar-la. Com ja ha segut reportat l'estabilitat de les cel · les és sensible a l'exposició oxigen i humitat, aquests són hàndicaps afegits per a aconseguir una configuració amb llarga vida útil i amb gran capacitat. La mesura en la qual aquests reptes ens afecten podria ser caracteritzada mitjançant tècniques morfològiques i electroquímiques *operando* simultànies amb il · luminació/obscuritat.

I, per finalitzar, la proposta d'un circuit equivalent que ens permetrà explicar els espectres d'impedància obtinguts d'aquests dispositius amb doble funcionalitat durant tot el perfil de càrrega i descarrega, és a dir, des de la il · luminació de la cel · la fins la descàrrega a una resistència connectada, discernint cadascun dels mecanismes implícits en el procés.

Conclusions and future work

The final chapter of this Thesis presents the conclusions of the attached publications, which have been published in renowned international journals.

Firstly, the use of non-destructive impedance spectroscopy technique together with another physicochemical and electrochemical techniques can be used to determinate the performance of any type of electrode. Morphology and electrochemical mechanisms which take place during the process can be linked by using equivalent circuits. This enables you to determine the limiting factor: diffusion-limiting mechanisms or the kinetics of reaction limitation itself.

Particularly, EIS allows characterize the lithium battery electrodes such as:

- The lithium iron phosphate ($LiFePO_4$) is a mineral from olivine family. It has been possible to model by equivalent circuits for electrodes of multi-particle, where, mainly, ion diffusion as slower carrier, as the principal kinetic limitation. These circuits enable to differentiate the lithium diffusion through the cathode-electrolyte interface (at high frequencies) and the capacitive behaviour when the lithium is stored in the cathode. In addition, it can evaluate the performance when LFP particles are imbedded in the PEDOT matrix to improve its electrical conductivity.

- For Lithium-oxygen cathodes, the energy is stored by the direct reaction between Li^+ ions and O_2 in a porous electrode that acts as an electric conductive substrate. The proposed equivalent circuit model enables the identification of the interfacial phenomena, the extended electrochemical double

layer capacitance, which is independent of the presence of oxygen, and chemical capacitance generated by oxygen reduction reaction (ORR capacitance).

- The last part of this thesis, corresponding to the recent hybrid perovskite halide lead anodes for lithium batteries. On the one hand, it was the first time that a lithium storage mechanism was proposed in three stages: insertion, conversion and alloying, supported by *operando* X-Ray Diffraction. On the other hand, the battery configuration enables to calculate of the lithium ion diffusion coefficient in $CH_3NH_3PbBr_3$ by the impedance spectra modelling.

To conclude, this Thesis presents a survey on the great applicability of the impedance spectroscopy technique to characterize the batteries electrodes. The results of this Doctoral Thesis, and specifically those corresponding to lithium batteries with perovskite anodes, are the early stage of an innovative research line, which is a battery promising line, as well as, who work in photovoltaic field.

Firstly, the perovskite anodes proposed mechanism allows to distinguish among three stages and how the starting material degrades. This can make easier to find out the consequences of lithium doping in perovskite cells and how it intervenes in the degradation. As well as, to limit the lithium content in the configurations, in order to increase its stability.

Secondly, if we are able to define the work limits and could design an optimal configuration for an integrated photobattery, which could be able to turn the solar energy into electrical energy and store it. Like, it has already been reported, the stability of the cells is sensitive to the exposure of oxygen and humidity, these are added handicaps to achieve a configuration with long useful life and with great capacity. The extent to which these challenges affect us could be characterized

by morphological and electrochemical techniques operating simultaneously with illumination / darkness.

To conclude, the proposal of an equivalent circuit that will allow us to explain the impedance spectrums obtained from these devices with dual functionality throughout the charge and discharge profile, it means from the illumination of the cell until the discharge, discerning each one of the implicit mechanisms in the process.